

9-15-2014

A Compact RF/Photonic Antenna using a Quantum Dot Mode Locked Laser as a Source

JUNGHOON KIM

Follow this and additional works at: https://digitalrepository.unm.edu/ece_etds

Recommended Citation

KIM, JUNGHOON. "A Compact RF/Photonic Antenna using a Quantum Dot Mode Locked Laser as a Source." (2014).
https://digitalrepository.unm.edu/ece_etds/137

This Dissertation is brought to you for free and open access by the Engineering ETDs at UNM Digital Repository. It has been accepted for inclusion in Electrical and Computer Engineering ETDs by an authorized administrator of UNM Digital Repository. For more information, please contact disc@unm.edu.

JUNGHOON KIM

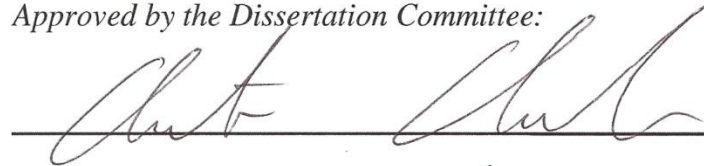
Candidate

Electrical and Computer Engineering

Department

This dissertation is approved, and it is acceptable in quality
and form for publication:

Approved by the Dissertation Committee:



, Chairperson



**A Compact RF/Photonic Antenna using a Quantum Dot
Mode Locked Laser as a Source**

BY

JUNGHOON KIM

B.S., ECE, Chung-Ang University, 2002
M.S., EE, Polytechnic Institute of New York University, 2005

DISSERTATION

Submitted in Partial Fulfillment of the
Requirements for the Degree of

**Doctor of Philosophy
Engineering**

The University of New Mexico
Albuquerque, New Mexico

December, 2010

Dedication

And whatever you do, whether in word or deed, do it all in the name of the Lord Jesus,
giving thanks to God the Father through him

- COLOSSIAN 3:17

To my beloved wife Kahwa, my hope Emma, and my parents for their support, sacrifices
and constant encouragement

Acknowledgements

I deeply thank to my advisor, Professor Christos Christodoulou, for his strong support and guidance through my PhD work. I also would like to thank my co-advisor, Professor Luke Lester for his directions and invaluable suggestions on my research. Special thanks go to the Air Force Office of Scientific Research for their financial assistance during my PhD term at the University of New Mexico.

At last, I thank to all of my friends whom I met at UNM for sharing the exciting and entertaining moments together.

**A Compact RF/Photonic Antenna using a Quantum Dot
Mode Locked Laser as a Source**

BY

JUNGHOON KIM

ABSTRACT OF DISSERTATION

Submitted in Partial Fulfillment of the
Requirements for the Degree of

**Doctor of Philosophy
Engineering**

The University of New Mexico
Albuquerque, New Mexico

December, 2010

A Compact RF/Photonic Antenna using a Quantum Dot Mode Locked Laser as a Source

by

JUNGHOON KIM

B.S., ECE, Chung-Ang University, 2002
M.S., EE, Polytechnic Institute of New York University, 2005
Ph.D, ECE, The University of New Mexico, 2010

ABSTRACT

The research presented here is focused on achieving an active compact RF/Photonic antenna module based on a broadband antenna design integrated with a quantum dot mode-locked laser (QDMLL). A two-section QDMLL is used to produce pulsed microwaves signals to feed the radiating antenna. To realize the microwave signal radiation generated by the QDMLL, several possible MLL-integrated-antennas are proposed. The prototype integrated antenna is fully described, including the design, fabrication, and characterization of the antenna performance.

Additionally, this work deals with the improvement of the radiation efficiency and functionality of the integrated module. An impedance matching network is designed to match the QDMLL to a bowtie slot antenna. The RF/Photonic integrated prototype is tested and analyzed over a wide frequency range.

Finally a QDMLL-integrated-phased antenna array is designed to achieve beam steering. By manipulating the applied voltage bias of each QDMLL, one can achieve beam steering without the use of external RF phase shifters yielding a more compact design of an RF/photonic antenna on a chip. The 2-element integrated prototype is presented and discussed. Beam-steering is fully demonstrated via both simulation and measurements.

TABLE OF CONTENTS

LIST OF FIGURES	x
LIST OF TABLES	xv
CHAPTER 1 INTRODUCTION	1
1.1 Motivation.....	1
1.2 Quantum Dots	2
1.3 Mode Locking Technique	5
1.4 Laser-integrated Antenna.....	7
1.5 Research Goals.....	10
1.6 Overview of Dissertation	10
1.7 References.....	12
CHAPTER 2 QUANTUM DOT PASSIVELY MODE-LOCKED LASER	14
2.1 Background.....	14
2.2 Device Structure.....	14
2.3 QDMLL Processing	16
2.4 Device Characterization.....	17
2.5 Reconfigurable Microwave Pulse Generator	25
2.6 Emission Measurement of the QDMLL Integrated Bow-tie Antenna.....	28
2.7 References.....	30
CHAPTER 3 ANTENNAS FOR HYBRID INTEGRATION WITH A QDMLL ...	32
3.1 Antenna Design.....	32
3.2 Two-port Simulation Technique into an Antenna Design	38
3.3 Fabrication Process and Hybrid Integration with a QDMLL	42

3.4	Characterization of the QDMLL-integrated-Antenna	44
3.5	Pattern Estimation of a Microstrip Antenna Integrated with QDMLL	49
3.6	Summary	55
3.7	References	57
CHAPTER 4 INTEGRATION WITH A BOWTIE SLOT ANTENNA AT 10 AND		
20 GHZ AND ANTENNA ARRAY BEAM-STEERING BY BIASING THE		
	QDMLL	58
4.1	Multi-resonance Bow-tie Slot Antenna	58
4.2	Antenna Fabrication and Measurement	66
4.3	Impedance Matching	68
4.4	Tapered Slot Antenna (TSA) Design using the Ideal Transmission Line	76
4.5	Tapered Slot Antenna (TSA) with Biasing Lines	82
4.6	2 Element TSA Array	86
4.7	Beam-steering Experiment	89
4.8	Conclusion	94
4.9	References	96
CHAPTER 5 CONCLUSIONS AND FUTURE WORK		98
5.1	Summary and Conclusions	98
5.2	Future Work and Recommendation	99

LIST OF FIGURES

Figure 1.1 Density of state functions for bulk, quantum well, quantum wire and quantum dot	4
Figure 1.2 The structure of InAs on GaAs Quantum Dots	4
Figure 1.3 (a) A simplified concept of a mode-locked laser resonator. (b) The pulse generation of an actively mode-locked laser. (c) The pulse generation of a passively mode-locked laser with a fast saturable absorber [9]......	5
Figure 1.4 A two-section QDMLL	7
Figure 1.5 The designed prototypes of the lithographic antennas integrated with the QDMLL; (a) Bow-tie antenna (b) Bow-tie slot antenna (c) Microstrip patch antenna (d) Tapered slot antenna	9
Figure 1.6 A dual frequency impedance matching transformer	9
Figure 2.1 Scheme of a 4.1-mm long two section QDMLL	15
Figure 2.2 Process flow chart.....	17
Figure 2.3 Experimental setup to measure RF spectrum of photocurrents	19
Figure 2.4 Measured RF spectrum of photocurrent of 4.1-mm long QDMLL for the conditions of -1V, 200mA	20
Figure 2.5 Measured average amount of photocurrents as a function of an applied pumping current	21
Figure 2.6 The experimental setup to measure the absolute phases of photocurrents	22
Figure 2.7 Equivalent lumped element models under (b) forward biasing condition and (c) reverse biasing condition	23

Figure 2.8 Measured Γ of a QDMLL on the smith chart from 5 GHz to 15 GHz under the biasing conditions of (a) I_{app} : 150mA, V_{app} : -2 V \sim +0.5 V , (b) I_{app} : N/A, V_{app} : -2 V \sim +0.5 V	24
Figure 2.9 The measured phase angle of the photocurrent out of the 4.1-mm long QDMLL under the biasing conditions of (a) I_{app} : 150mA, V_{app} : -2 V \sim +0.5 V, (b) I_{app} : N/A, V_{app} : -2 V \sim +0.5 V	25
Figure 2.10 Multi-section QDMLL with 27 segments	27
Figure 2.11 An operation map of the reconfigurable multi-section QDMLL	28
Figure 2.12 The two-section QDMLL-integrated-bowtie antenna	29
Figure 2.13 ESA spectrum of MLL on the 10GHz antenna chip	29
Figure 3.1 Quasi-static impedance of a bow-tie antenna as a function of the flare angle for various substrate: GaAs($\epsilon_r=12.9$), FR-4($\epsilon_r=4.9$), Rogers RT 5880($\epsilon_r=2.2$), Taconic TLX-3($\epsilon_r=2.33$).....	33
Figure 3.2 (a) Front view of the coplanar strip (CPS) line based on GaAs. (b) Top view of CPS line; T: height of a substrate, W: strip line width, g: air gap	34
Figure 3.3 Quasi-static characteristic impedance of a co-planar strip (CPS) line as a function of the air gap (g) for various CPS line's width (W): $\epsilon_r=12.9$ (Semi-insulating Gallium Arsenide), $h=450 \mu m$	36
Figure 3.4 Quasi-static characteristic impedance of a co-planar strip (CPS) line as a function of the CPS line's width (W) for different air gaps (g): $\epsilon_r=12.9$ (Semi-insulating Gallium Arsenide), $h=450 \mu m$	37

Figure 3.5 A bow-tie antenna with 90° flare angle. The height of a triangle is H and the base is 2H. Two bows are electrically separated by an air gap ('g')	38
Figure 3.6 Impedance π -network model of a bow-tie antenna	39
Figure 3.7 Computed impedance of a bow-tie antenna for various triangle heights	40
Figure 3.8 (a) Simplified π -network model (b) Equivalent lumped circuit model of a bow-tie antenna	41
Figure 3.9 Return loss plot on the Smith chart	42
Figure 3.10 Fabrication procedures for the QDMLL-integrated-bowtie antenna.....	44
Figure 3.11 Return loss measurement setup: network analyzer (HP 8722D), 140 μ m pitching microwave-probe.	45
Figure 3.12 Comparison between the measured return loss and simulated one	47
Figure 3.13 Measurement setup for the emission out of an integrated active antenna.....	48
Figure 3.14 Measured emitting power intensity out of the QDMLL-integrated-bowtie antenna	49
Figure 3.15 Measured and simulated return losses of a fabricated microstrip antenna.....	52
Figure 3.16 The experimental setup for the emission pattern estimation	53
Figure 3.17 RF power spectrums of the radiation intensity for different biasing conditions.....	54
Figure 3.18 Comparison of the measured estimated emission patterns and simulated result	55
Figure 4.1 Characteristic impedance of CPW line of a 0.3 mm wide center microstrip line and 0.2 mm wide air gap.....	60
Figure 4.2A Computed transmissions (S ₂₁) and reflection (S ₁₁) of a 10mm long CPW.	61
Figure 4.3A CPW fed bow-tie slot antenna; H: height of a bow, B: width of a bow	62

Figure 4.4 Simulated real and imaginary impedances of a bow-tie slot antenna	63
Figure 4.5 The block diagram of impedance matching	63
Figure 4.6 The bow-tie slot antenna with a short stub matching line	64
Figure 4.7 Impedances on the smith chart for both the matched and unmatched case	65
Figure 4.8 Return loss-comparison of the both matched and unmatched case	66
Figure 4.9 Simulated and Measured return losses of a bow-tie slot antenna.....	67
Figure 4.10 Equivalent circuit model of the matching circuit between a QDMLL and a bow-tie slot antenna; Z_{QD} : output impedance of a QD-MLL and Z_{ant} : impedance of a bow-tie slot antenna	68
Figure 4.11 Measured output impedance of the saturable absorber in the QDMLL as a function of reverse biasing voltages	69
Figure 4.12 Ideal Transmission line model of matching network between the QDMLL and bow-tie slot antenna	70
Figure 4.13 The CPW-based-impedance matching circuit between the QDMLL and bow- tie slot antenna	72
Figure 4.14 The simulated return losses under the consideration of both matched and unmatched cases, and the computed gain in dB	73
Figure 4.15 The schematic of an impedance transformer of two open stub lines.	74
Figure 4.16 A dual-band impedance matching network embedded bow-tie slot antenna ..	75
Figure 4.17 Measured signal power intensity comparison between matched and unmatched case	75
Figure 4.18 Electrical field distributions on the TSA	78
Figure 4.19 Equivalent circuit of the stepline.....	78

Figure 4.20 (a) Two-TLIN model of a TSA; (b) Three-TLIN model of a TSA; (c) Four-TLIN model of a TSA	79
Figure 4.21 Schematic views of the TSA with increased transmission lines; (a) two section, (b) three section, (c) four section, (d) V-LTSA	81
Figure 4.22 Return losses of the TLIN-modeled TSAs and the V-LTSA	81
Figure 4.23 QDMLL-integrated-TSA module and the enlarged view of a TSA	83
Figure 4.24 Input impedance (Z_{in}) of the TSA	84
Figure 4.25 Measured and simulated return losses	85
Figure 4.26 Simulated directivity and measured radiation intensity over $-90^\circ < \phi < 90^\circ$	86
Figure 4.27 S21-simulation of the 2 element TSA array as increasing the interval distance	88
Figure 4.28 Photo-image of the fabricated QDMLL-integrated-LTSA array	89
Figure 4.29 Experimental environment and schematics of a measurement setup for beam-steering	91
Figure 4.30 Photo-image of the measurement setup	91
Figure 4.31 The measured output phase angle of a QDMLL as applied voltage	92
Figure 4.32 The measured emission power-intensity for different biasing conditions	93
Figure 4.33 The simulated directivity of a TSA array	94

LIST OF TABLES

Table 3.1 Impedances of a bow-tie antenna for different bow heights.....	40
Table 3.2 Signal-to-noise ratio (SNR) for different biasing conditions.....	51
Table 3.3 Normalized signal-to-noise ratio (SNR) for the different biasing conditions. ..	51
Table 4.1 Dimensions of the proposed antenna.....	60
Table 4.2 Impedance and S_{11} in dB in both the matched and unmatched case.....	70
Table 4.3 Dimensions of an impedance matching circuit.....	74
Table 4.4 Dimensions of slot line model of a TSA.....	80
Table 4.5 Detail dimensions of a TSA.....	83

Chapter 1

Introduction

1.1 Motivation

Research in higher frequency is reaching the terahertz domain as the speed of microprocessors using electrical clock distribution increases. However, current microelectronic technology is limited by the copper interconnects used because the resistive and associated power loss increase as the size of a device becomes compact. In addition to that, the available power from solid state devices decreases as the operating frequency increases. In order to resolve the limitation, optical interconnects and semiconductor mode-locked Lasers (MLLs) are suggested as an ideal source for the ultra-short optical pulse generation. Compared to other competing approaches such as the heterodyning technique of two laser [1-2], this method is able to obtain higher optical-to-electrical conversion efficiency. Additionally, due to this technique, stabilization of the generated frequency is easier by removing the uncorrelated phase noise [3]. Therefore, the pulsed mm-wave generation using MLLs has attracted interest for various applications e.g. optical clock recovery, optical time multiplexing and switching [4-7].

We start with an array of quantum dot diode cells configured to emit mode-locked laser pulses. By manipulating the biasing of the saturable absorber (SA) section of a quantum dot mode-locked laser (QDMLL), the various resonance frequencies generation can be controlled. The optically generated microwave signals are then transported to broad-band lithographic antennas. Therefore the MLLs-integrated-active antennas are accomplished. The resonance frequency of the proposed antennas is determined by the repetition rate of the MLL. When the saturable absorber of the MLL is reversely biased,

longitudinal modes in the laser cavity are synchronized and the light becomes pulsed emission. Its repetition rate is determined by cavity round-trip time which is determined by $f_R = c/2nL$. Here c is the speed of light, n is the group index of refraction, L is the cavity length and f_R is the repetition rate. For this research, the 4.1-mm long QDMLL is used to obtain the hybrid integration with wireless RF modules and its estimated repetition rate can be computed to be 10 GHz.

Of particular interest in many applications are lithographic antennas because of their simple designs and broad-band impedance characteristics. Various prototypes of broad band antennas are designed and integrated with a QDMLL. Finally, we measured the integrated antenna's performances. The measurement results indicate that the proposed QDMLL is an excellent candidate for the compact microwave source. The repetition rate of a single MLL is possibly tuned by changing the locations of applied voltage bias. On this research, the ultimate reconfigurable wireless transmitting module will be enabled by combining a multi-section QDMLL with reconfigurable antennas.

1.2 Quantum Dots

Quantum dot (QD) materials are unique, due to their ultra-broad bandwidth, ultra-fast gain dynamics, and easily saturated gain and absorption, which make them an ideal choice for monolithic semiconductor MLLs [4]. These characteristics particularly give MLLs the advantage of stability over a wider power range compared to the quantum well (QW). With this increased range of operation, higher microwave power can be extracted from the device with lower phase noise [3].

In our research, a two-section passive QDMLL in 4.1 mm length demonstrated higher optical-to-electrical conversion efficiency than the optical heterodyning technique

of two lasers [8]. By comparing the density states for bulk, quantum well (QW), quantum wire (QWire) and quantum dot (QD), new properties of QDs are described. Figure 1.1 shows the state density for different materials [9]. The bulk material is a 0-dimension of confinement. Its state density is continuous and proportionally related to the square root of the energy. Compared to the bulk, the state density in QWs (1-dimension) decays so that its density forms a step function. In 2-dimensions, the density of the quantum wire's state further decreases compared to the QWs. Finally, the state density in QDs (3-dimensions) is a δ -function in energy. Although the state density of the real QD-materials has a line expansion resulted from fluctuations in the quantum dot sizes, the state density is still attenuated compared to the quantum wire. By taking advantage of the small size of QDs, the fundamental benefits of QD-lasers are an ultra-low threshold current, temperature-insensitive operation, high material gain and differential gain, a decreased line width enhancement factor, an ultra-broad bandwidth, easily saturated gain and absorption, and a larger tuning range of the lasing wavelength. The structure of InAs on GaAs Quantum Dots is shown in Figure 1.2.

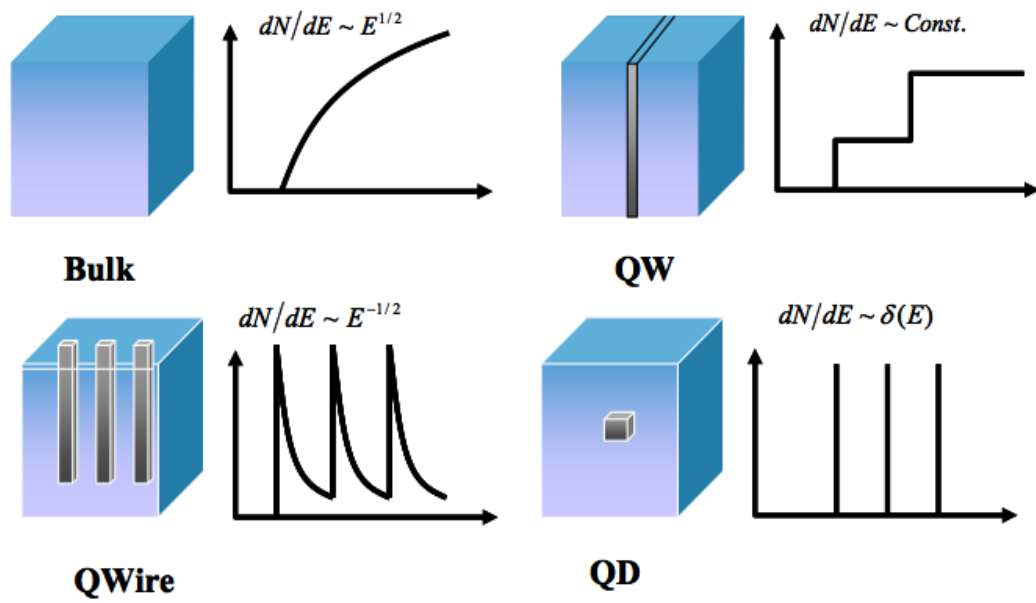


Figure 1.1 Density of state functions for bulk, quantum well, quantum wire and quantum dot

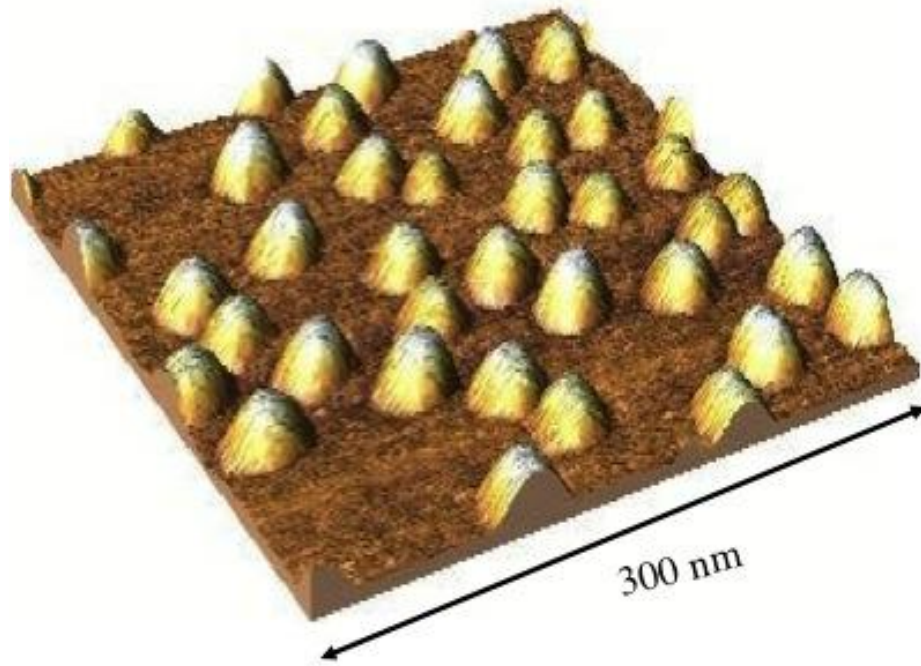


Figure 1.2 The structure of InAs on GaAs Quantum Dots

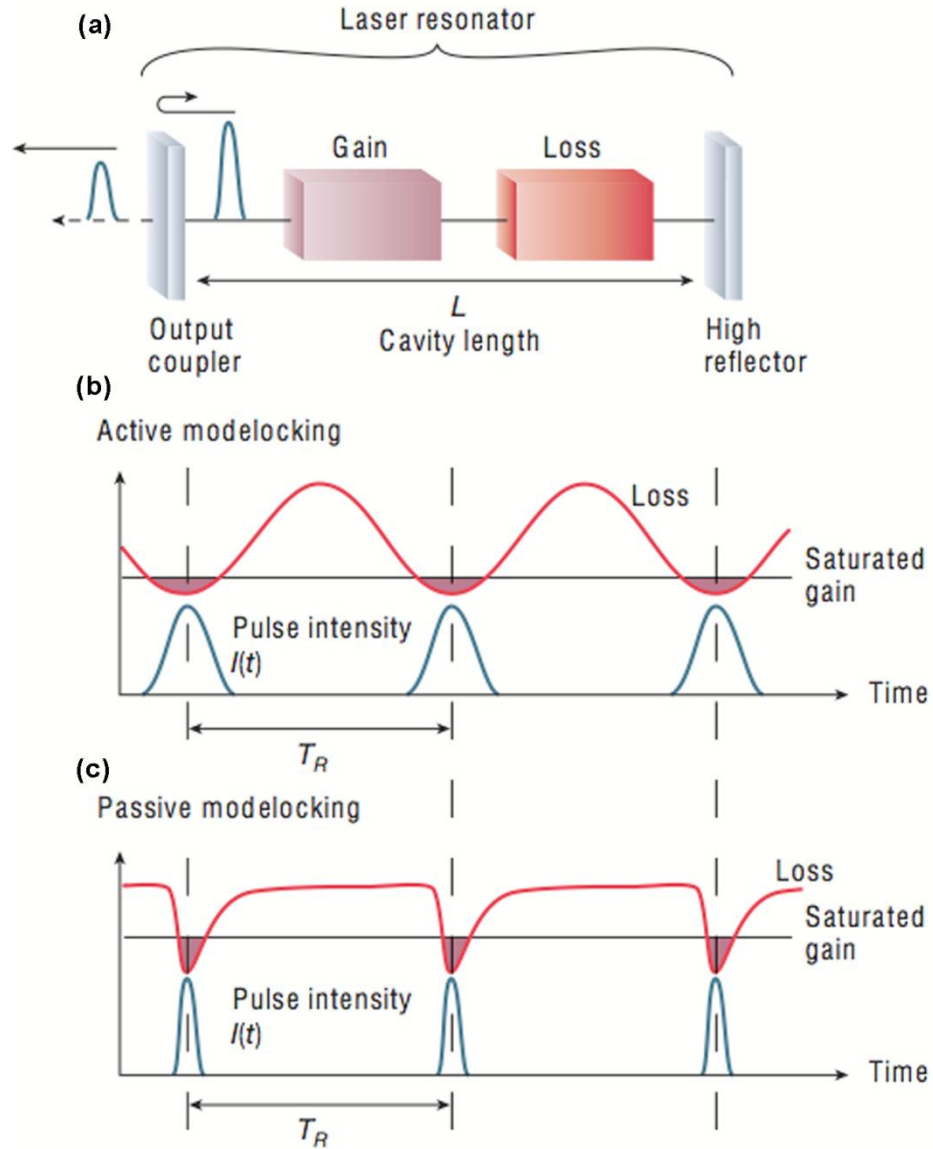


Figure 1.3 (a) A simplified concept of a mode-locked laser resonator. (b) The pulse generation of an actively mode-locked laser. (c) The pulse generation of a passively mode-locked laser with a fast saturable absorber [9].

1.3 Mode Locking Technique

The mode locking technique is a method to generate ultrashort pulses from lasers. The mode-locked laser (MLL) consists of a gain and a saturable absorber which is a

nonlinear passive element [10]. Due to the nonlinear effects of absorbers in MLLs, the formation of ultrashort pulses circulating in the laser cavity is possible. When it is in the steady state, the various effects influencing the circulating pulse are in a balance so that the pulse parameters are unchanged after each completed round trip. Every time the pulse inside laser cavity hits the output coupler's mirror, the pulse is emitted. As previously mentioned in section 1.1, the pulse repetition rate corresponds to the resonator round-trip time. Because the fast recovery time of the absorber, the pulse can be trimmed to a very short pulse width of picosecond order. In this way, the peak power of the MLL can be much higher than the average power.

MLLs can be either active or passive mode locked. Active mode locking approach uses an external signal in order to induce a modulation of the light inside the cavity. If the modulation is synchronized with the resonator round trips, ultrashort pulses are generated. Passive mode locking method uses the nonlinear passive element forming an ultrashort pulse circulating in the laser cavity. In our research, we used the passive mode locking approach by implementing a saturable absorber causing self-modulation of light. In Figure 1.3, much shorter pulse signals can be obtained by the passive mode-locking approach, compared to the active mode-locking approach. This is basically because a saturable absorber modulates the resonator losses much faster than an electronic modulator.

In conclusion, the result in the frequency domain is given as a phase-locked frequency comb containing a constant mode spacing of the pulse repetition rate. The spectral width of the envelope of this frequency comb is inversely proportional to the pulse duration. For this research, the 4.1mm long QDMLL device is used. Figure 1.4

depicts the 2-section QDMLL composed of a 3.8-mm long gain-section and a 0.3-mm long SA. The gain and SA are electrically isolated. The details on the passive QDMLL are introduced in Chapter 2. For the alternative method, the hybrid mode-locked technique is used in which active and passive mode locking are applied at the same time. The key advantage of it is an externally controlled pulse repetition rate.

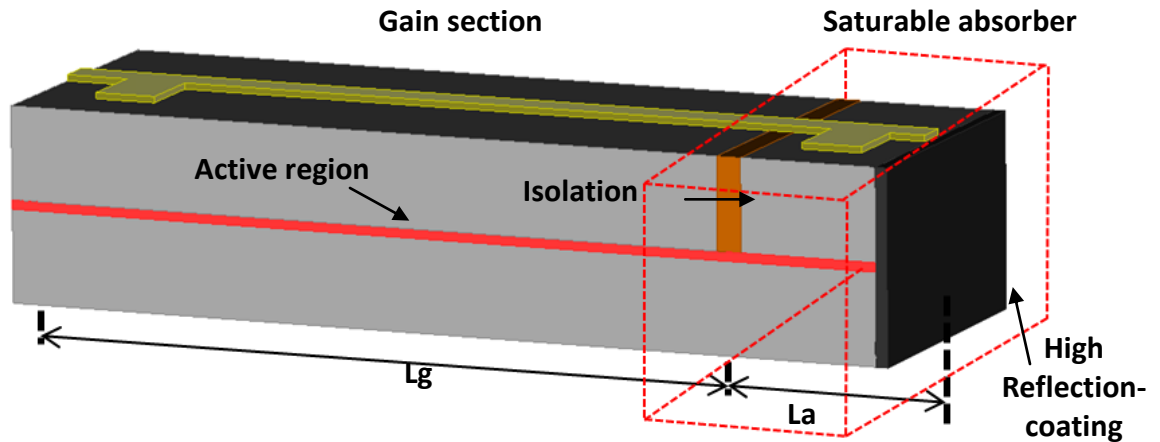


Figure 1.4 A two-section QDMLL

1.4 Laser-integrated Antenna

To radiate energy from the QDMLL, an antenna must be integrated to it lithographically. Various prototypes of lithographic antennas, in Figure 1.5, were designed and integrated with QDMLLs. First, a bow-tie antenna was tried. The bow-tie antenna was chosen due to its broadband bandwidth and its simplicity of integrating with a laser chip [11]. A semi-insulating GaAs was used as a substrate not only to achieve the monolithic integration with a QDMLL, but also to reduce the undesirable loss induced by mismatches among different materials.

The idea of using a QDMLL as a compact microwave source is verified by measuring the estimated emitting power intensity patterns of the QDMLL-integrated-active antenna. For the estimated radiation pattern, a rectangular microstrip antenna was used. By the existence of an infinite ground plane, the microstrip antenna can accommodate the environmental limitation where a metallic sub-mount is required underneath an antenna substrate to operate a QDMLL. We discuss the antenna design and radiation pattern measurement in Chapter 3.

Since a single QDMLL can produce the multiple harmonics of the fundamental repetition rate, new types of broad band antennas are requested to carry out the higher orders of repetition rates out of a QDMLL. To this end, the bow-tie slot antenna was proposed to accommodate the higher repetition rates of a QDMLL so that the MLL can extend its operating ranges.

Another area for improvements during integration is to introduce the matching circuit. As the operating frequency increases, the available power from solid state devices decreases. Therefore, the delivered power using an impedance transformer between the solid state device and an antenna is very critical [12]. Details of impedance matching are discussed in Chapter 4. The prototype of designed matching circuit is shown in Figure 1.6.

The phased array tapered slot antenna integrated with QDMLLs is fabricated to perform the beam-steering by manipulating the applied voltage biases. Detail antenna design and test are also presented in Chapter 4.

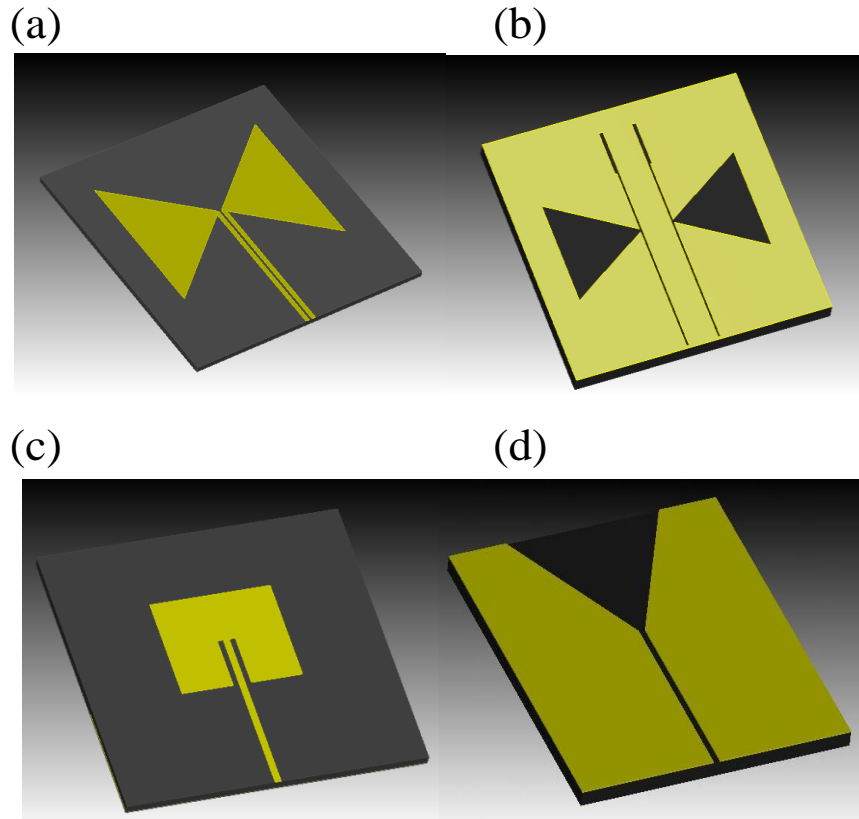


Figure 1.5 The designed prototypes of the lithographic antennas integrated with the QDMLL; **(a)** Bow-tie antenna **(b)** Bow-tie slot antenna **(c)** Microstrip patch antenna **(d)** Tapered slot antenna

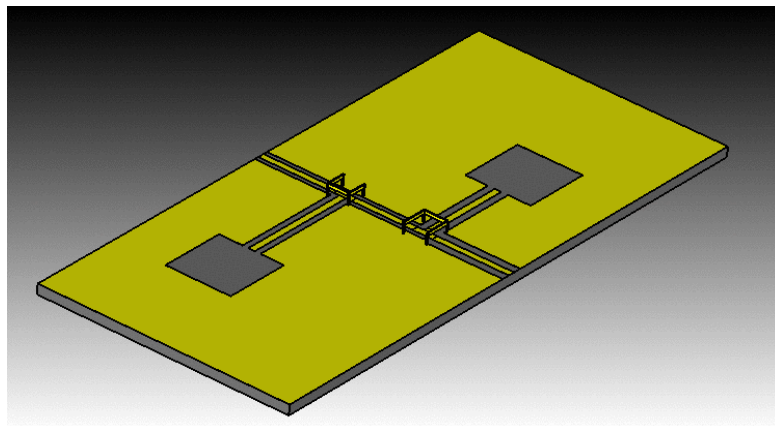


Figure 1.6 A dual frequency impedance matching transformer

1.5 Research Goals

Our research goals can be summarized as follow:

- 1) To design a broad-band antenna
- 2) Integrate the antenna with the QDMLL
- 3) Test radiation pattern
- 4) Optimize the matching between the antenna and the QDMLL
- 5) Design a multiple resonance antenna
- 6) Design an array antenna and study its beam steering properties
- 7) Demonstrate that phase shifting can be achieved by manipulating the biasing conditions on the QDMLL

1.6 Overview of Dissertation

This dissertation demonstrates that a quantum dot mode-locked laser can be used as a compact mm-wave source for an antenna to radiate high frequency RF signals. The resultant device is a compact RF/Photonic antenna. In Chapter 2, the idea of the 4.1-mm long quantum dot mode-locked laser (QDMLL) is introduced, and the principle of the pulsed microwave signal generation from the saturable absorber is explained. The structure of a two-section QDMLL is discussed as well. Additionally, the multi-section QDMLL is introduced as a feasible reconfigurable microwave source. In Chapter 3, some QDMLL-integrated-broad band antennas are presented. As a first prototype, a bow-tie antenna is fully described, including its design, fabrication, and characterization of its

radiation performance. The estimated emission pattern of the integrated antenna /source module is also measured. For the pattern estimation, a microstrip patch antenna is designed and incorporated with a MLL. To design antennas efficiently, the π -network model is employed. In Chapter 4, the improvement of a QDMLL-integrated-antenna is discussed. The use of the bow-tie slot antenna allows the QDMLL to extend its operating frequency range. For the improvement in the radiation efficiency, the impedance matching between an antenna and a MLL is proposed. A beam steering capability using a phased antenna array is demonstrated by changing the applied voltage bias on each QDMLL. Each element of the array is integrated with the 4.1mm long QDMLL. In Chapter 5, conclusions and future work are discussed.

1.7 References

1. J. Genest, M. Chamberland, P. Tremblay, M. Tetu, "Microwave signals generated by optical heterodyne between injection-locked semiconductor lasers," *IEEE J. Quantum Electron*, vol. 33, no. 6, pp. 989-998, Jun 1997.
2. M. A. Bernacil, S. O'Connor, B. Maher, A. Dekelaita, and D. Derickson, "Microwave Signal Generation Using Self-Heterodyning of a Fast Wavelength Switching SG-DBR Laser," *IEEE MTT-S International symposium*, pp. 603-606, Jun 2008
3. A. Gubenko, D. Livshits, I. Krestnikov, S. Mikhlin, A. Kozhukhov, A. Kovsh, N. Ledentsov, A. Zhukov and E. Portnoi, "High-power monolithic passively mode locked quantum-dot laser", *ELECTRONICS LETTERS* 29th September 2005 Vol. 41 No. 20.
4. M. Passerini, M. Sorel and P.J.R. Laybourn, "Optimization and regime characterization of monolithic semiconductor mode-locked lasers and colliding-pulse mode-locked lasers at microwave and millimeter-wave frequency," *IEE Proc. Optoelectron.*, vol. 151, no. 6, pp. 508-512, Dec. 2004.
5. C.-Y. Lin, Y.-C. Xin, J. H. Kim, C. G. Christodoulou, and L. F. Lester, "Compact Optical Generation of Microwave Signals Using a Monolithic Quantum Dot Passively Mode-Locked Laser", *IEEE Photonics Journal*, vol. 1, no. 4, pp. 236-244, Oct. 2009.
6. S. Arahira and Y. Ogawa, "Polarization-insensitive all-optical 160-Gb/s clock recovery with a monolithic passively mode-locked laser diode in polarization-diversity configuration," *IEEE J. Quant. Electron.*, vol. 43, no. 6, pp. 1204-1210, Dec. 2007.

7. R. Kaiser and B. Huttli, "Monolithic 40-GHz mode-locked MQWDBR lasers for high-speed optical communication systems," *IEEE J. Selected Topics Quant. Electron.*, vol. 13, no. 1, pp. 125–135, Jan./Feb.2007.
8. E. U. Rafailov, M. A. Cataluna, and W. Sibbett, "Mode-locked quantum-dot lasers", *Nature Photonics*, Vol. 1, 395 – 401, July 2007.
9. Y.-C. Xin, "Quantum Dot Multi-section light emitters", *Ph.D dissertation*, University of New Mexico, 2006.
10. U. Keller, "Recent developments in compact ultrafast lasers," *Nature*424, 831-838, (2003).
11. J.H. Kim, C.G. Christodoulou, Z. Ku, Y.-C. Xin, N.A. Naderi, L.F. Lester, "Quantum-dot laser coupled bowtie antenna," *IEEE Int. Antennas and Propagation Symp.*, pp. 1-4, Jul.2008.
12. J. H. Kim, C. G. Christodoulou, Z. Ku, C.-Y. Lin, Y.-C. Xin, N. A. Naderi, L. F. Lester, "Hybrid Integration of a Bowtie Slot Antenna and a Quantum Dot Mode-Locked Laser," *Antennas and Wireless Propag. Letters*, vol. 8, pp1337 - 1340, 2009.

Chapter 2

Quantum dot passively mode-locked laser

2.1 Background

Due to the various advantages including its compact size, direct electrical pumping, high electrical-to-optical-to-electrical (E/O/E) conversion efficiency and low power consumption to operate, monolithic passively mode-locked lasers (MLLs) are promising candidates for novel microwave frequency generators [1-4]. Particularly, the unique material properties of quantum dot (QD) materials such as ultra broad bandwidth, ultra fast gain dynamics, and easily saturated gain and absorption, result in an ideal material for MLLs [5,6]. Previously, semiconductor active regions such as quantum wells could produce the same optical gain and absorption functions, but frequently required separate optimization of the optical materials in the MLL cavity. However, for the QDMLL, the same epitaxial structure in both the absorber and gain sections can be used for achieving the need for compactness.

2.2 Device Structure

The laser epitaxial structure of this device is a multi-stack "Dots-in-a-WELL" (DWELL) structure that is composed of an optimized six-stack QD active region grown by solid-source molecular beam epitaxy (MBE) on a (001) GaAs substrate [7]. The 3.5- μm wide optical ridge-waveguide devices are fabricated with standard multi-section device processing. To achieve the 10 GHz repetition rate of a QDMLL, the two-section QD passively MLLs are made with a total cavity length of 4.1-mm. A highly reflective coating ($R \approx 95\%$) is applied to the mirror facet next to the SA and the other facet is cleaved ($R \approx 32\%$). The scheme of the proposed two-section QDMLL is shown in Figure

2.1. In general, a metal-semiconductor-metal (MSM) detector is applied to convert the optically generated pulse from MLLs to the electrical pulse signal [8].

In our research, optically generated signals are alternatively to bypass the LT-MSM detector and use the transient photocurrent produced in the SA of the passive QDMLL as the microwave signal source. In other words, as the picosecond optical pulse goes into the SA, the leading edge of the optical pulse is absorbed thereby creating free carriers. The applied DC voltage bias result in that electrons and holes are swept to the metal contacts. Thus, the microwave signals can be generated by simply applying DC voltage bias on an absorber. Due to its simpler geometry, it can have the potential to convert the ultrafast optical signal to electrical pulse more efficiently. The benefits of RF generation from the passive QDMLL compared to competing methods such as optical heterodyning of two continuous-wave single mode lasers are the higher conversion efficiency and easier stabilization of the generated RF frequency. These advantages of the passive QDMLLs are achieved by removing the uncorrelated phase noise and temperature fluctuations.

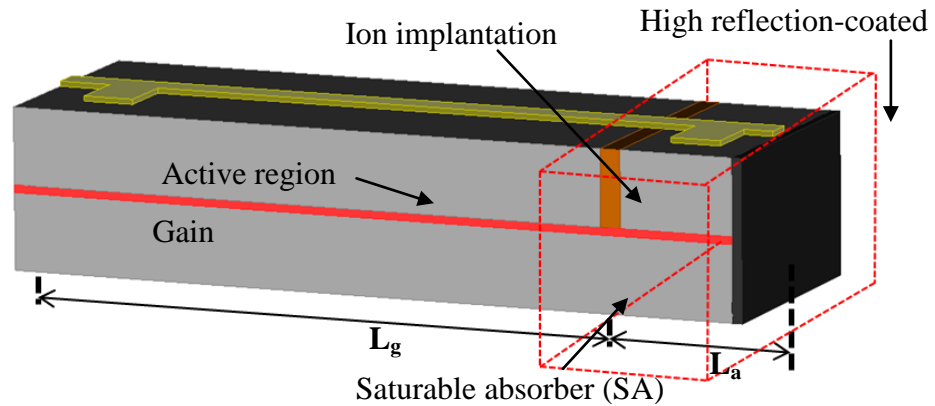


Figure 2.1 Scheme of a 4.1-mm long two section QDMLL

2.3 QDMLL Processing

The wafers are processed into two-section devices following standard ridge waveguide laser processing. Wafers were processed to be 3.5- μm wide, deep-etched ridge waveguides with segmented contact sections. The processing is demonstrated as shown in Figure 2.3. The sample was etched to form 3.5- μm wide, 1.8- μm deep ridges by inductively coupled plasma (ICP) etching after the first lithography was applied on the wafer with the ridge-waveguide-mask. Next, standard benzocyclobutene (BCB) processing was applied to achieve isolation between the p-type metal and the etched cladding layer. The segmented-contact mask was used to make photoresist patterns for the p-type metal deposition and ion implantation. The isolation between the adjacent sections is provided by proton implantation. By means of implantation, an isolation resistance is greater than $10\text{M}\Omega$. As the post processing of the n-type metal deposition on the substrate side of the wafer, the sample was annealed at 380°C for 1 minute. A temperature greater than 380°C can crack the BCB. Another Ti/Au metal layer was deposited for n-side mounting.

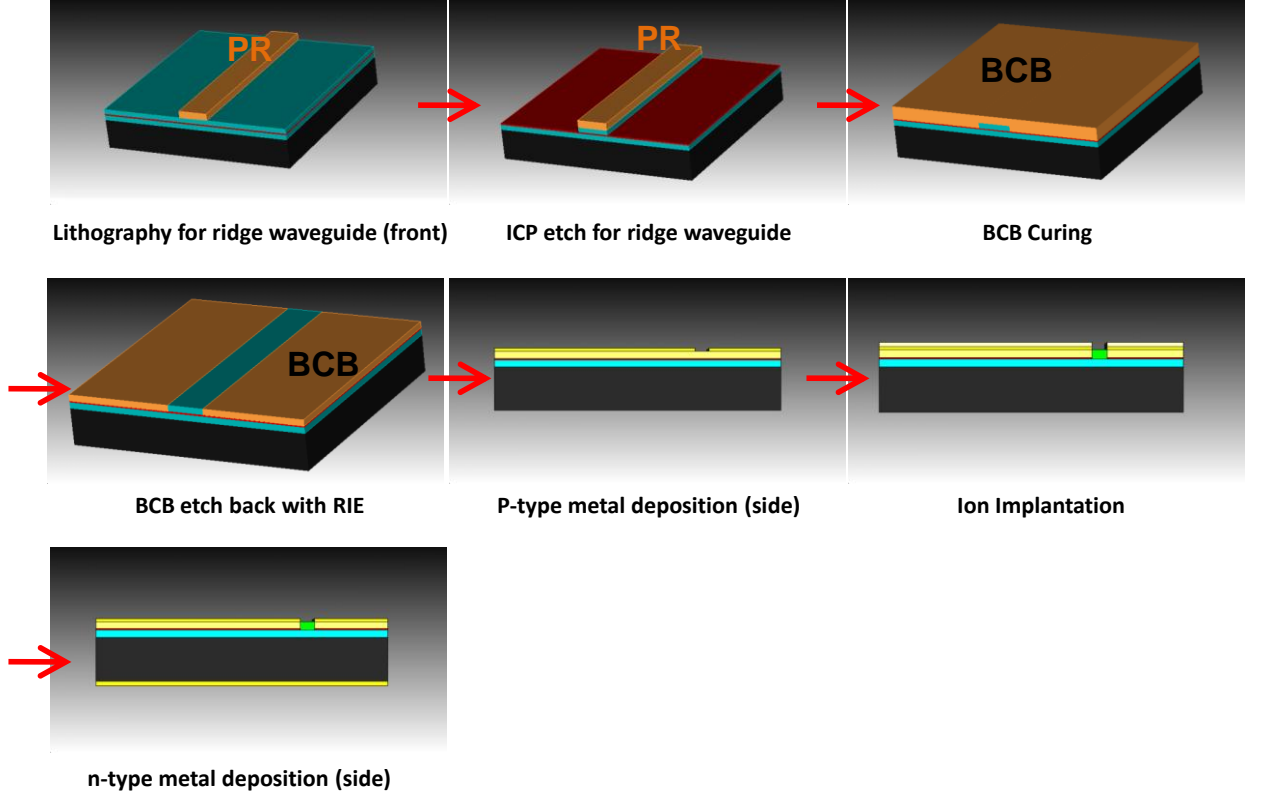


Figure 2.2 Process flow chart

2.4 Device Characterization

In this section, the characterized results of a two-section QDMLL are presented. In order to suitably apply a QDMLL as a compact microwave frequency source for hybrid integration with antennas, we measured the intensity and phase of photocurrent along the frequencies generated by the QDMLL.

In Figure 2.3, the experimental setup is demonstrated. The two-section laser was mounted on an Aluminum nitride (AlN) substrate and then on copper heat sink for both good thermal conductivity and electrical isolation. The temperature is remained at 20°C by a thermoelectric cooler (TEC). The optical output of the laser was collected with an optical head, which integrates a lens, an isolator and a short 1-m single-mode polarization

maintaining (PM) fiber pigtail, then connected into the Corning SMF-28e fibers followed by a polarization controller. The collected emission was fed into the autocorrelator (Femtochrome FR-103XL Autocorrelator) to measure the pulse width, and the optical spectrum analyzer (Agilent 86142B OSA) to measure the optical spectra through fiber couplers.

The repetition rate of the electrical pulses out of an absorber was measured by the RF-spectrum analyzer (HP 8563E ESA). We used the 150- μm pitch pico-probe to apply DC-voltage bias on an absorber and simultaneously extract the photocurrent out of a QDMLL. The bias-T circuit is located in between a QDMLL and RF spectrum analyzer. It is composed of the combination of parallel-inductor and series-capacitor. Due to the bias-T, the microwave pulse signals from a SA are delivered to the RF spectrum analyzer without affecting the voltage source. ADC voltage can only be applied on the absorber of a QDMLL since the capacitor prevents the DC voltage flowing into the RF spectrum analyzer.

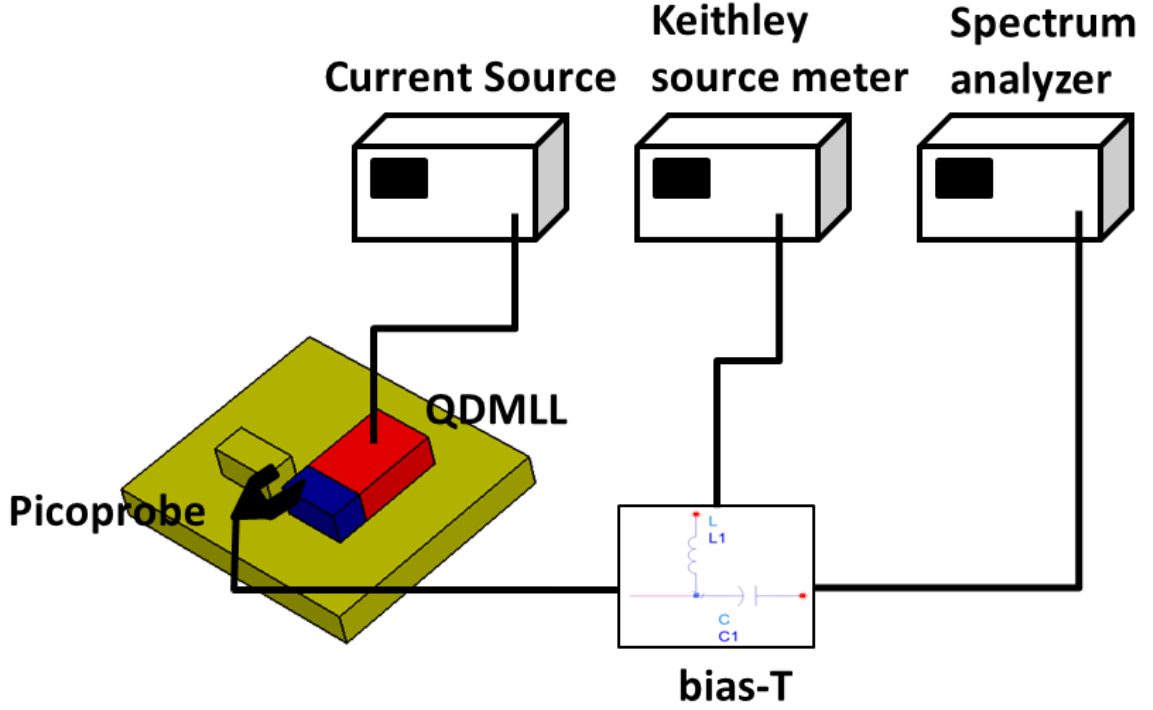


Figure 2.3 Experimental setup to measure RF spectrum of photocurrents

For the 4.1-mm long QDMLL, the measured RF spectrum of the photocurrent is shown in Figure 2.4. Under the biasing conditions of -1V and 200-mA, the intensity of photocurrent is measured to be -3.5 dBm at 10 GHz and -15.16 dBm at 20 GHz, respectively. The fundamental repetition rate of the QDMLL is 10.19 GHz. The repetition rate is determined based on the equation of $f_r = c/2nL$ where f_r is the repetition rate of a QDMLL, c is the speed of light at the vacuum medium, n is the group index of refraction, and L is the total cavity length of a MLL. As previously discussed, the pulse signals are generated after the light inside of the cavity finishes its round trip thereby the effective speed of medium is divided by $2L$. Figure 2.5 presents the average photocurrent intensity as the function of pumping currents on the gain-section. From the result, it is noticed that the average amount of photocurrents is proportional to the applied pumping

current after threshold current. However, the status of mode-locking in the QDMLL becomes unstable if the pumping current is over the mode-locking condition.

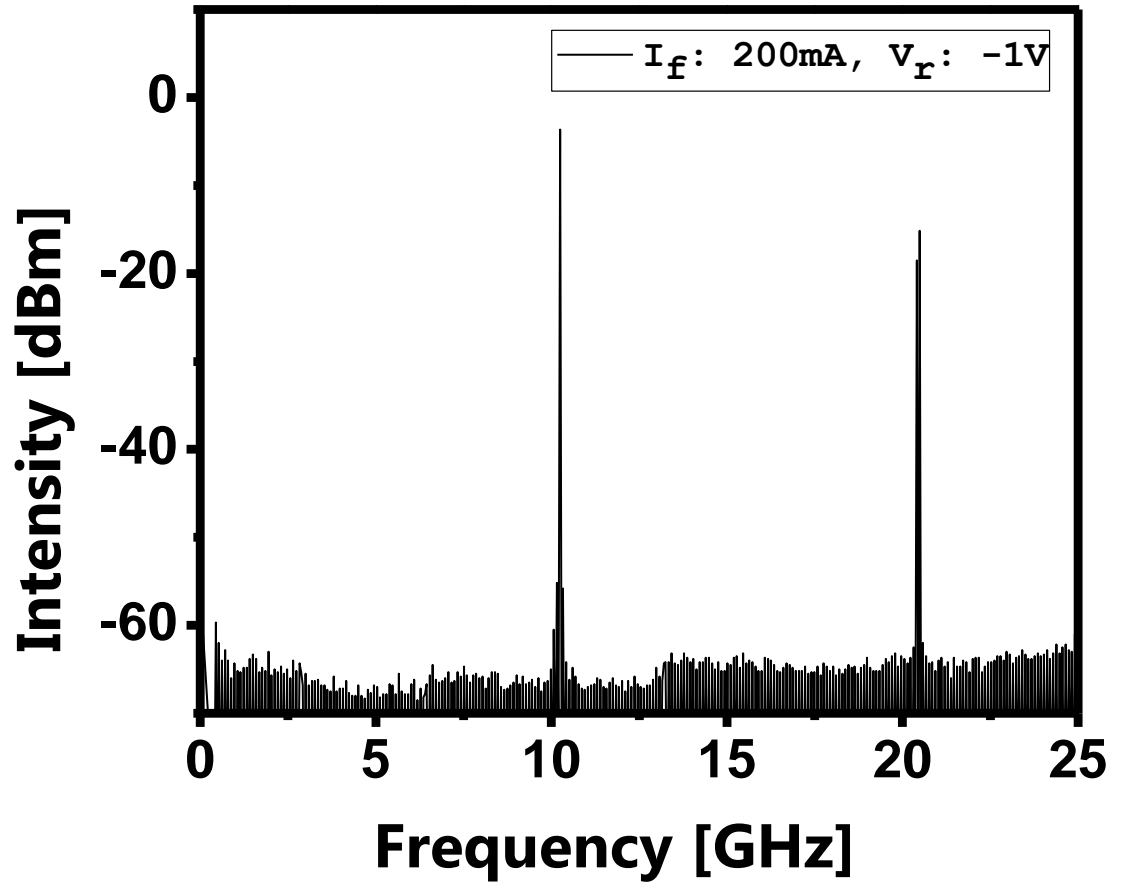


Figure 2.4 Measured RF spectrum of photocurrent of 4.1-mm long QDMLL
for the conditions of -1V, 200mA

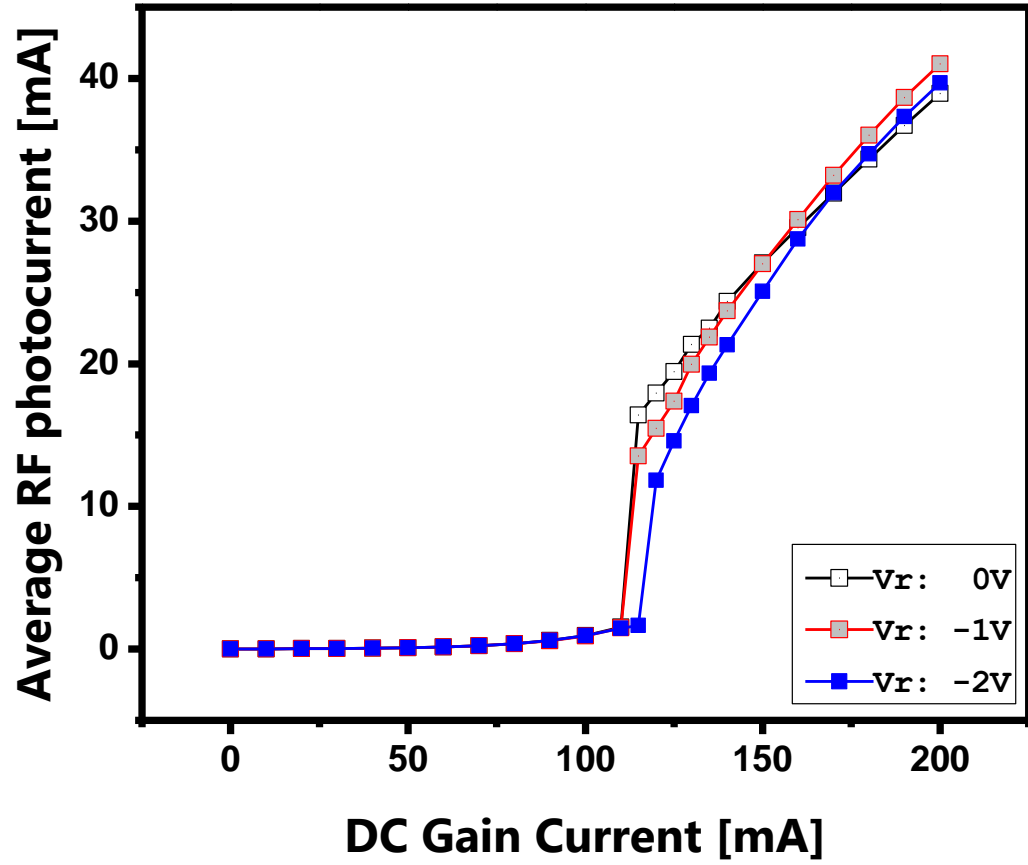


Figure 2.5 Measured average amount of photocurrents as a function of an applied pumping current

To be more efficient microwave source, the QDMLL requires not only the amplitude of output signal, but its phase as well. After conducting [S]-parameter measurement using the setup in Figure 2.6, the output phase of a MLL is extracted based on the measured impedances of a QDMLL. Compared to the RF-spectrum measurement

setup previously shown in Figure 2.3, the DC voltage on an absorber is applied through the network analyzer without the bias-T circuit.

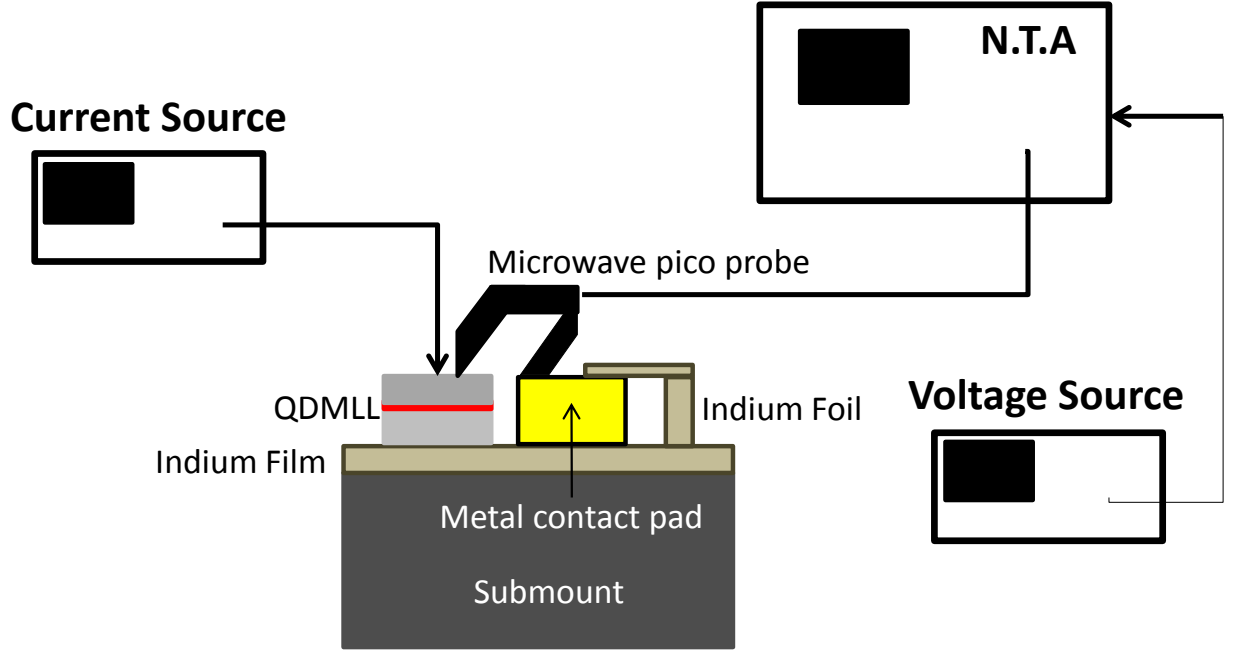


Figure 2.6 The experimental setup to measure the absolute phases of photocurrents

By changing the applied voltage bias on an absorber, the different output phase angle of the photocurrent out of a QDMLL can be observed. To explain the difference in the photocurrent phase, the equivalent circuit model of the absorber is employed under both (a) forward-and (b) reverse-bias conditions, as shown in Figure 2.7 [8]. The simplified equivalent lumped element models are regarded based on the model of a photodetector built on metal-semiconductor-metal. When the absorber is under the forward voltage bias, the phase of the impedance is computed to be $\theta_f = \tan^{-1}(\omega L / R_s)$. On the other hand, the phase of reverse biasing condition is $\theta_r = \tan^{-1}\{ (L/R_p) [1 + (\omega C_T R_p)^2 - (C_T/L) R_p^2] \}$. Here, ω is the angular frequency, L is the

inductance value, R_s and R_p are the series and parallel resistances in the semiconductor medium, respectively, and C_T is the capacitance induced between the top and bottom metal layers. From the simplified result, the phase angle of a reverse bias condition has an additional term compared to that of forward voltage bias so that the output photocurrents of a QDMLL can be produced with different phases by means of varying the DC applied voltages on an absorber.

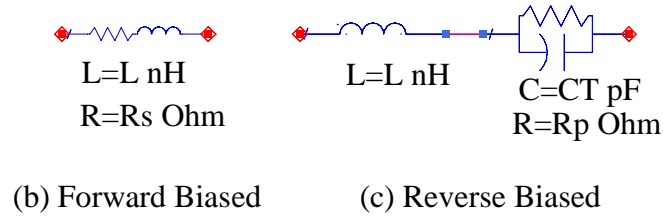


Figure 2.7 Equivalent lumped element models under (b) forward biasing condition and (c) reverse biasing condition

This result is used later on to design a compact phased antenna array integrated with QDMLLs. In order to support the theory, the output phases of photocurrents are measured by changing the applied voltage biases in Figure 2.8. In the plot, the result under the pumping current is presented in Figure 2.8 (a). We also compared the measured data to that of the unpumped case in (b). Finally, the phase angle of the output photocurrent, θ_{ph} , can be extracted from the measured $[\Gamma]$ -matrix based on the relation below.

$$\theta_{ph} = \tan^{-1} \left(\frac{\Gamma_{real}}{\Gamma_{imag}} \right)$$

Figure 2.9 shows the change in phase at different frequencies. When the pumping current is applied on the gain-section, the phase angle difference from V_{app} : -2V to V_{app} : +0.5V is larger than that without the pumping current. As results, the most variation in the phase angle occurs when the applied voltage is increased from -2 V to +0.5 V with a pumping current and the difference of angles is measured to be 10° at 10 GHz.

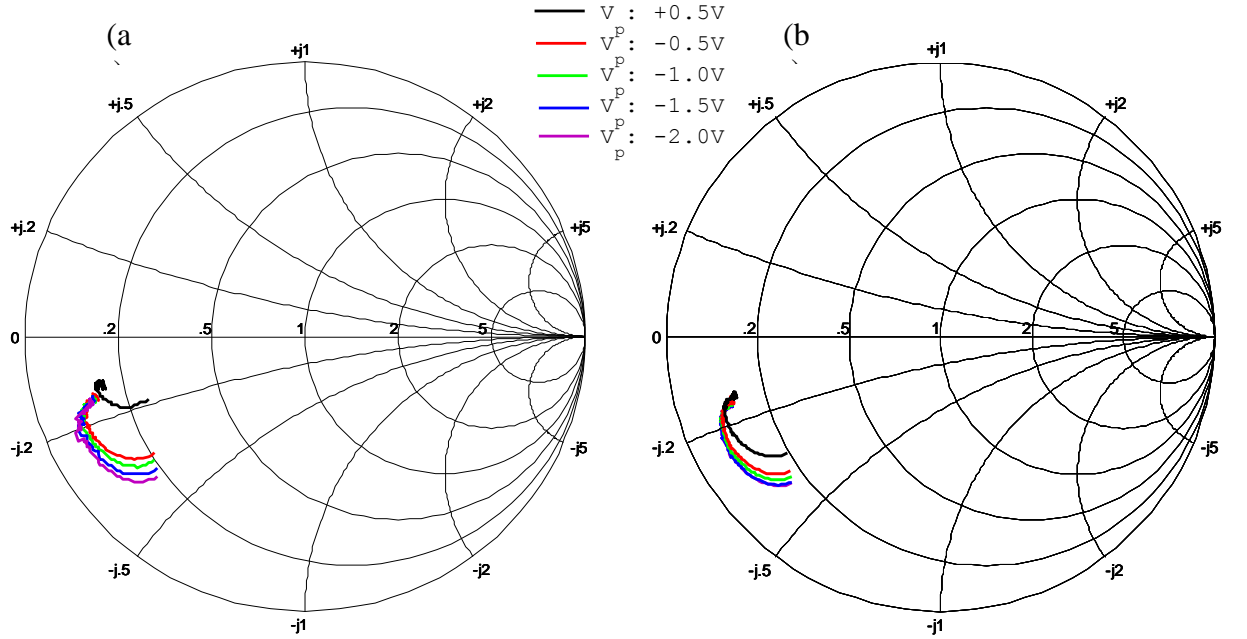


Figure 2.8 Measured Γ of a QDMLL on the smith chart from 5 GHz to 15 GHz under the biasing conditions of (a) I_{app} : 150mA, V_{app} : -2 V ~ +0.5 V , (b) I_{app} : N/A, V_{app} : -2 V ~ +0.5 V

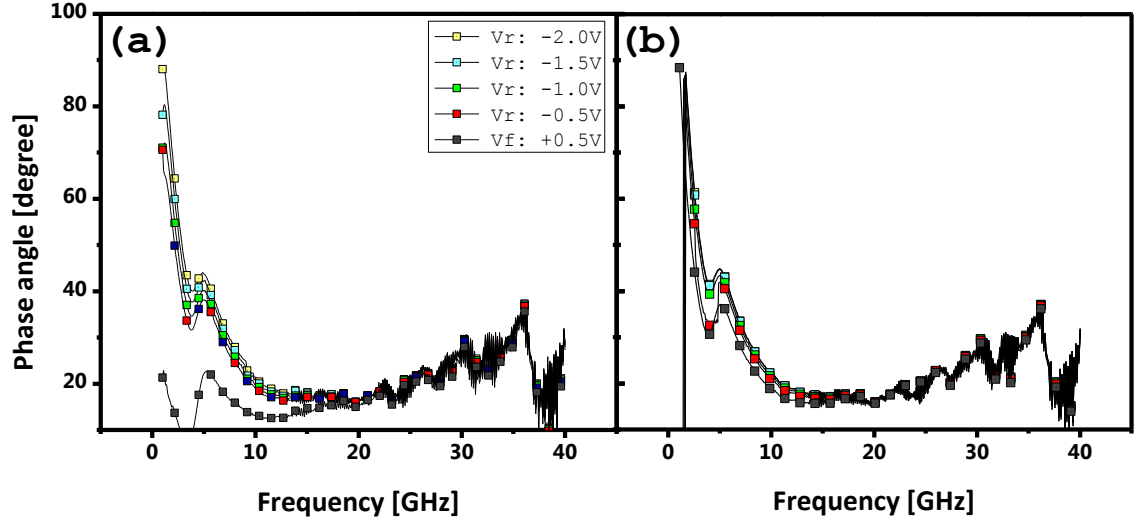


Figure 2.9 The measured phase angle of the photocurrent out of the 4.1-mm long QDMLL under the biasing conditions of (a) I_{app} : 150mA, V_{app} : -2 V ~ +0.5 V, (b) I_{app} : N/A, V_{app} : -2 V ~ +0.5 V

2.5 Reconfigurable Microwave Pulse Generator

In the previous section, a traditional two-section QDMLL was presented. It consists of a single gain and saturable absorber. The repetition rate can be estimated by its total cavity length. According to the repetition rate equation with the cavity length ($f_r = c/2nL$), the repetition rate is inversely related to the length of a cavity. The equation indicates that the higher rates can be obtained by making the laser chip shorter. However, the cavity length of a QDMLL is not much shorter than 1-mm because of the size of the absorber. The absorption is not sufficient with for shorter absorber lengths. It results in the fundamental repetition rate not higher than 40 GHz. To overcome this limit for the higher order repetition rates, the multi-section QDMLL is proposed. It consists of

connections of segmented QDMLLs and isolations. The generation of a desired higher repetition rate becomes difficult to satisfy because of the operating requirement that the absorber be short enough to simulate higher frequency harmonics and also long enough to maintain the sufficient absorption at the same time.

As an alternative, by putting the SA at different locations of segments within the multi-section QDMLL, the laser can harmonically generate pulses at one of possible multiples of the fundamental repetition rate [9]. Instead of using a single SA, the double interval technique applies two separate SAs which stimulate two different harmonics. With the double interval technique, the higher orders of the fundamental repetition rate can be obtained. Therefore, the multi-section QDMLLs by a double interval technique can function not only as the higher frequency microwave generation, but also as the reconfigurable microwave source. One of the main advantages of using this device is that the repetition rate can be controlled by means of biasing voltages. The ultimate reconfigurable wireless transmitting module can be achieved by combining the multi-section QDMLLs with reconfigurable antennas in future work. For the multi-section QDMLL, the corresponding section number ‘ m ’ that can stimulate the n^{th} -order harmonic generation can be determined based on the following equation [9].

$$m = \frac{N + 1}{2} \mp N \left(\frac{1}{2} - \frac{1}{n} \right)$$

where N is the total number of segments in the laser cavity. For instance, the second harmonic can be generated by locating the SA at section 14 as shown in Figure 2.10.

Likewise, the third harmonic is supported by putting the SA at either section 9 or 19. From the above equation, the actual section number ' m ' for the third harmonic is 8.5 or 18.5. However, the segment numbers are integers so that the values of ' m ' are chosen by rounding them. With the double interval technique, the repetition rate map of the QDMLL of Figure 2.10 is plotted in Figure 2.11 as a function of the gain current and the reverse bias voltage on section 14. It shows the possibility of supporting several orders of harmonics. In reality, not only the 6th order of harmonic can be reinforced, but also the 2nd and 3rd harmonics can be obtained due to the double interval biasing technique on the multi-section QDMLL. Since a single multi-section QDMLL can support diverse repetition rates, it can be an excellent candidate as reconfigurable microwave sources [10].

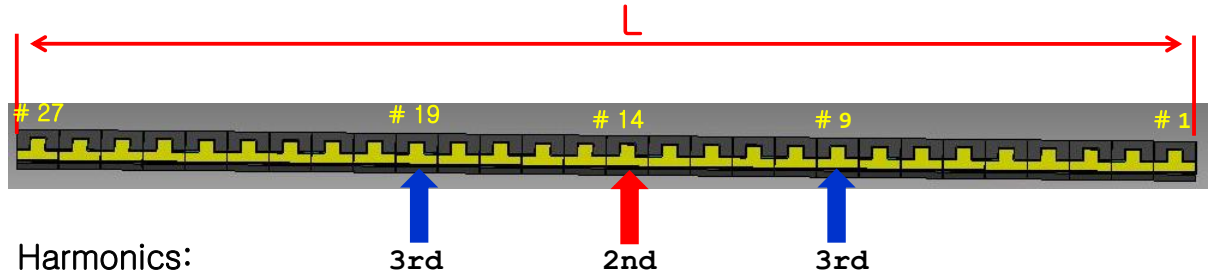


Figure 2.10 Multi-section QDMLL with 27 segments

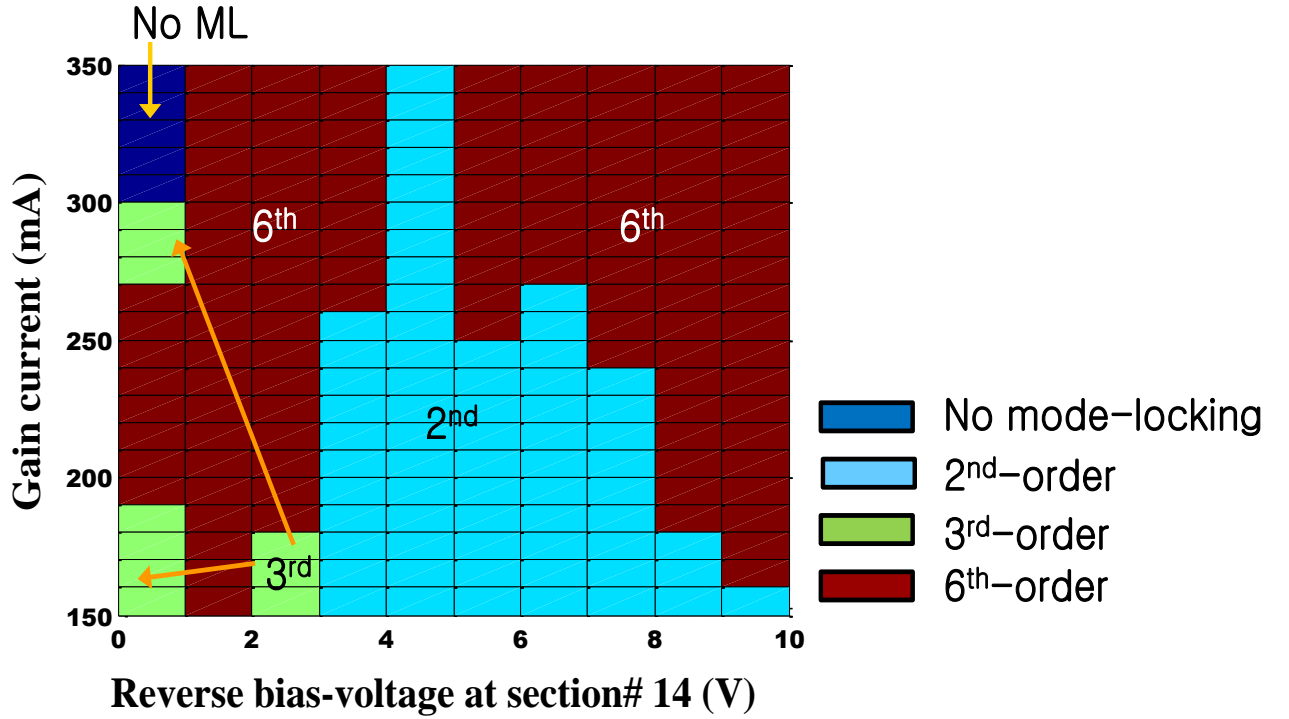


Figure 2.11 An operation map of the reconfigurable multi-section QDMLL

2.6 Emission Measurement of the QDMLL Integrated Bow-tie Antenna

In order to verify its practical usage into the QDMLLs into a microwave system, various types of antennas were designed and integrated with QDMLLs. We fabricated the first chip at 10GHz with a bow-tie antenna as shown in Figure 2.12 [11]. The MLL device has a 1 mm long absorber with the total cavity length of 4mm.

In this particular scheme, the absorber of the MLL is bond-wired to the antenna with 0 V reverse bias is applied on an absorber. Testing from the front facet with a spectrum analyzer shows that the MLL device operates mode-locking at 10.24 GHz with gain currents of 62-mA. The RF spectrum of the radiated signal from the antenna is shown in Figure 2.13. By characterizing the radiation out of the integrated antenna, the concept of using a QDMLL as a compact microwave source can be verified.

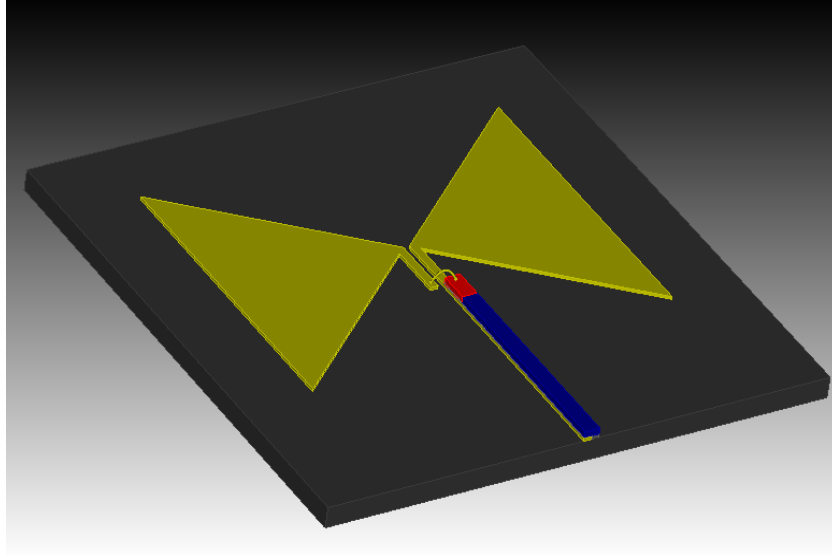


Figure 2.12 The two-section QDMLL-integrated-bowtie antenna

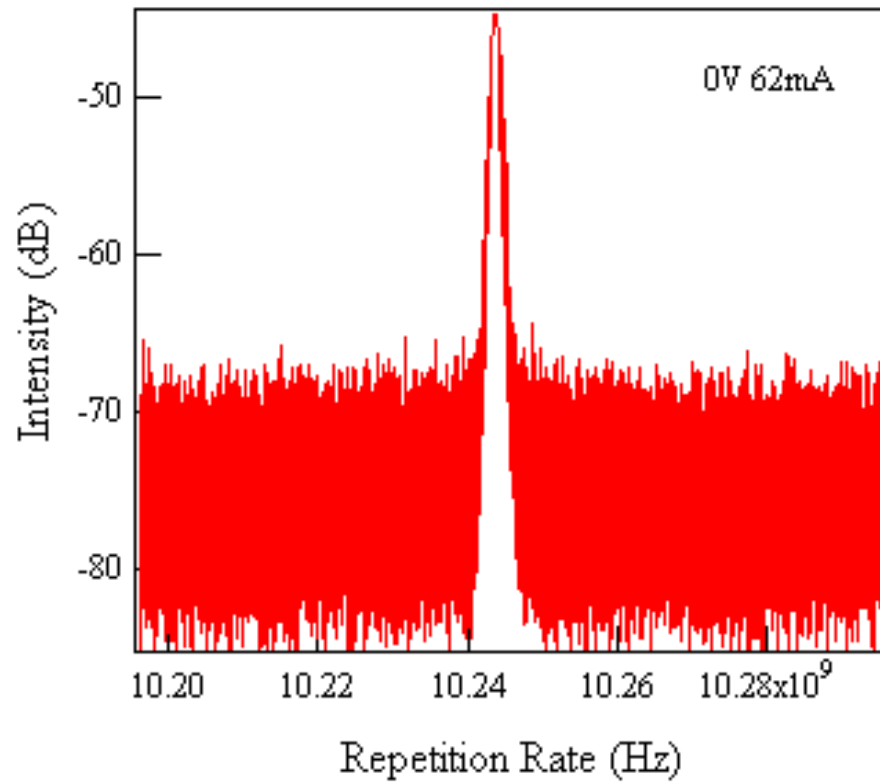


Figure 2.13 ESA spectrum of MLL on the 10GHz antenna chip

2.7 References

1. A.J.C. Vieira, P.R. Herczfeld, A. Rosen, M. Ermold, E.E. Funk, W.D. Jemison, and K.J. Williams, “A mode-locked microchip laser optical transmitter for fiber radio”, *IEEE Trans. Microw. Theory Tech.*, vol. 49, no. 10, 1882–1887 (2001).
2. J.H. Kim, C.G. Christodoulou, Z. Ku, Y.C. Xin, N.A. Naderi, L.F. Lester, “Quantum-dot laser coupled bowtie antenna,” *IEEE AP-S*, pp.1 – 4 (2008).
3. D.J. Derickson, R.J. Helkey, A. Mar, J.G. Wasserbauer, and J.E. Bowers, “Microwave and millimetre-wave signal generation using mode locked semiconductor lasers with intrawaveguide saturable absorbers,” *Proc. of IEEE Int. Symp. on Microwave Theory and Techniques*, pp. 753–756 (1992).
4. C.-Y. Lin, Y.-C. Xin, J.H. Kim, C.G. Christodoulou and L.F. Lester, “Compact Optical Generation of Microwave Signals Using a Monolithic Quantum Dot Passively Mode-Locked Laser,” *IEEE Photonics Journal*, Vol. 1, no. 4, pp. 236-244, Oct. 29 (2009)
5. E.U. Rafailov, M.A. Cataluna, W. Sibbett, “Mode-locked quantum-dot lasers,” *Nature Photonics* 1, 395-401, (2007).
6. M. G. Thompson, A. R. Rae, M. Xia, R. V. Penty, and I. H. White, “In GaAs quantum-dot mode-locked laser diodes,” *IEEE J. Sel. Top. Quantum Electron.* 15, 661-672, (2009).
7. Y.-C. Xin, Y. Li, V. Kovanis, A. L. Gray, L. Zhang, and L. F. Lester, “Reconfigurable quantum dot monolithic multi-section passive mode-locked lasers,” *Opt. Express* 15 7623-7633 (2007).

8. A.H. Steinbah, I. Penn, N. Chokshi, D. Martin, K. Slomkowski, W. Baun, N. Agrawal, R. Ben-Michael, M.A. Itzler, “Equivalent circuit modeling of p-i-n photodiodes for 40 Gb/s receivers,” *LEOS 2002. IEEE*, Vol. 2, pp. 486 – 487(2002).
9. Y.-C. Xin, Y. Li, V. Kovanis, A. L. Gray, L. Zhang, and L. F. Lester, “Reconfigurable quantum dot monolithic multisection passive mode-locked lasers”, *Opt. Express*, 15, 7623-7633 (2007)
10. Y. Li, F. L. Chiragh, Y.-C. Xin, C.-Y. Lin, J.-H. Kim, C.G. Christodoulou, L.F. Lester, “Harmonic mode-locking using the double interval technique in quantum dot lasers,” *Opt. Express*, 18 (14), 14637-14642 (2010).
11. J. H. Kim, C. G. Christodoulou, Z. Ku, Y.-C. Xin, N. A. Naderi, and L. F. Lester, “Quantum-dot laser coupled bowtie antenna”, AP-S 2008. IEEE, 5-11 July 2008

Page(s): 1 - 4

Chapter 3

Antennas for hybrid integration with a QDMLL

3.1 Antenna Design

Various types of antennas as potential candidates for integration with a QDMLL are proposed. A microstrip antenna has numerous benefits including compact size, light weight, low cost and ease of fabrication. Yet, the resonant modes of the microstrip antennas generally depend on the half-wavelength structure thereby operating bandwidths become narrow. Here, we prefer to use broadband antennas that can be matched to a QDMLL over a wide range of frequencies.

As a start, a bow-tie antenna is used to achieve the QDMLL-integrated-antenna device. The bow-tie antenna is broadband in nature and offers some superior impedance matching characteristics. The antenna structure is determined by its flare angle and bow length. The quasi-static antenna impedance can be computed by the following equation [1]. In Figure 3.1, Z_{qs} is plotted as a function of the flare angle based on the different dielectric permittivity.

$$Z_{qs} = \frac{120\pi}{\sqrt{\epsilon_{eff}}} \left[\frac{K(k)}{K(k')} \right] [\Omega]$$

where

$$\epsilon_{eff} = \frac{1}{2}(\epsilon_{r,substrate} + 1), k = \tan^2 \left(\frac{\pi}{4} - \frac{\theta}{4} \right), k' = \sqrt{1 - k^2}$$

and θ is a flare angle.

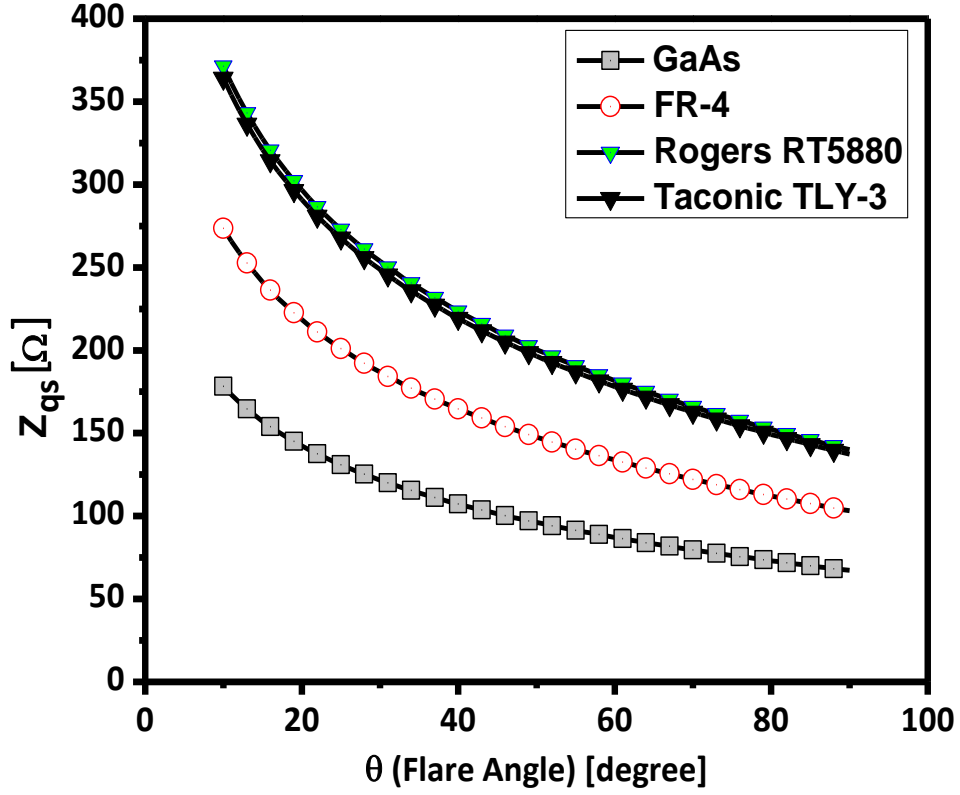


Figure 3.1 Quasi-static impedance of a bow-tie antenna as a function of the flare angle for various substrate: GaAs($\epsilon_r=12.9$), FR-4($\epsilon_r=4.9$), Rogers RT 5880($\epsilon_r=2.2$), Taconic TLY-3($\epsilon_r=2.33$)

The 450 μ m thick semi-insulating Gallium Arsenide (SI-GaAs) is used as a substrate of an antenna whose dielectric constant is 12.9 and loss tangent at the resonance is 0.0016. For the 50 Ω input impedance of an antenna, the dimensions of an equilateral triangle are determined with a 90 $^\circ$ flare angle and 2.8-mm long height. The SI-GaAs is used as an antenna substrate.

A co-planar strip (CPS) line is the transmission line used to deliver the photocurrent out of a QDMLL into the bow-tie antenna. The geometry of the CPS-line is shown in Figure 3.2.

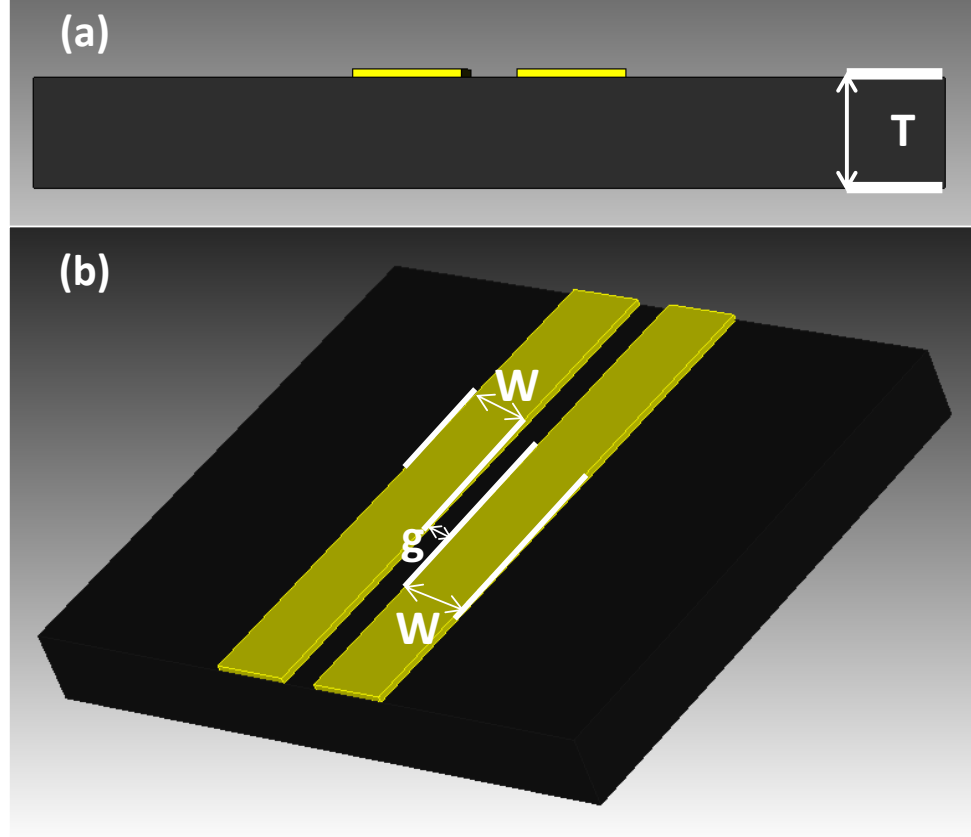


Figure 3.2 (a) Front view of the coplanar strip (CPS) line based on GaAs. (b) Top view of CPS line; T: height of a substrate, W: strip line width, g: air gap

The dimensions of the proposed CPS-line are determined to make a characteristic impedance of a CPS line be 50Ω . The dimensions of the structure are its air gap (g), line width (W) and its thickness (T). According to the analytical formula presented in [2], the effective dielectric constant is calculated by

$$\epsilon_{\text{eff}} = \frac{1}{2}(\epsilon_{r,\text{GaAs}} + 1)$$

The characteristic impedance of a CPS line is

$$Z_{c,CPS} = \frac{120\pi}{\sqrt{\epsilon_{eff}}} \left[\frac{K(k')}{K(k)} \right] [\Omega]$$

where $k = \sqrt{1 - \frac{\sinh^2\left[\frac{\pi}{2T}\left(\frac{g}{2}\right)\right]}{\sinh^2\left[\frac{\pi}{2T}\left(W + \frac{g}{2}\right)\right]}}$, $k' = \sqrt{1 - k^2}$, T: height of a substrate, W: strip line

width, g: air gap and K is the complete elliptical integral of the first kind.

In Figure 3.3, the characteristic impedance of a CPS line is computed as function of its air gap. The result indicates that its impedance is proportional to the air gap. Likewise, for different gaps, the impedances are also calculated as a function of line width in Figure 3.4. It shows that the characteristic impedance is inversely proportional to a CPS line width. As a final choice, the width of a CPS line is 160- μm , separated by the 20- μm air gap for a $Z_{c,CPS} = 50 \Omega$ at 10 GHz. The scheme of a bow-tie antenna is presented in Figure 3.5.

Based on the determined parameters, the height (H) of a triangle of a bow-tie antenna is optimized by using commercial software. To perform the field simulation, we use the CST–Microwave Studio Suite [3].

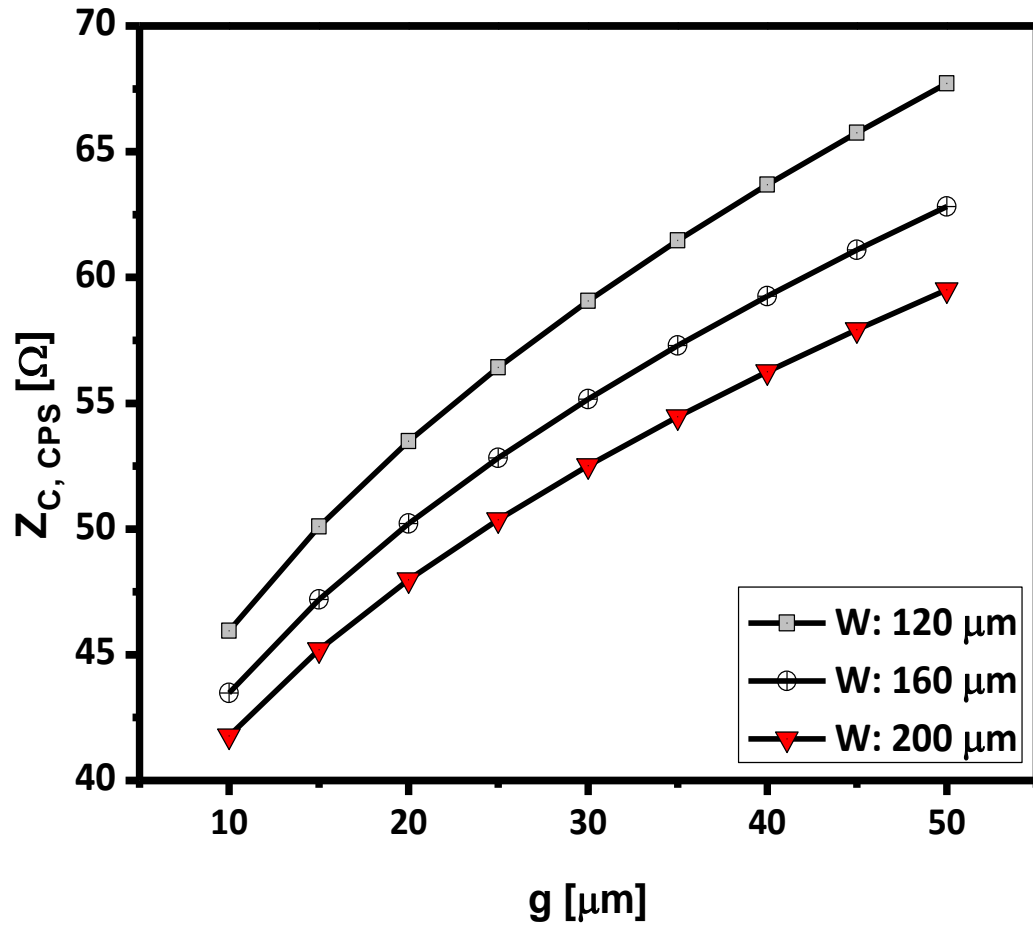


Figure 3.3 Quasi-static characteristic impedance of a co-planar strip (CPS) line as a function of the air gap (g) for various CPS line's width (W): $\epsilon_r=12.9$ (Semi-insulating Gallium Arsenide), $h=450$ μm

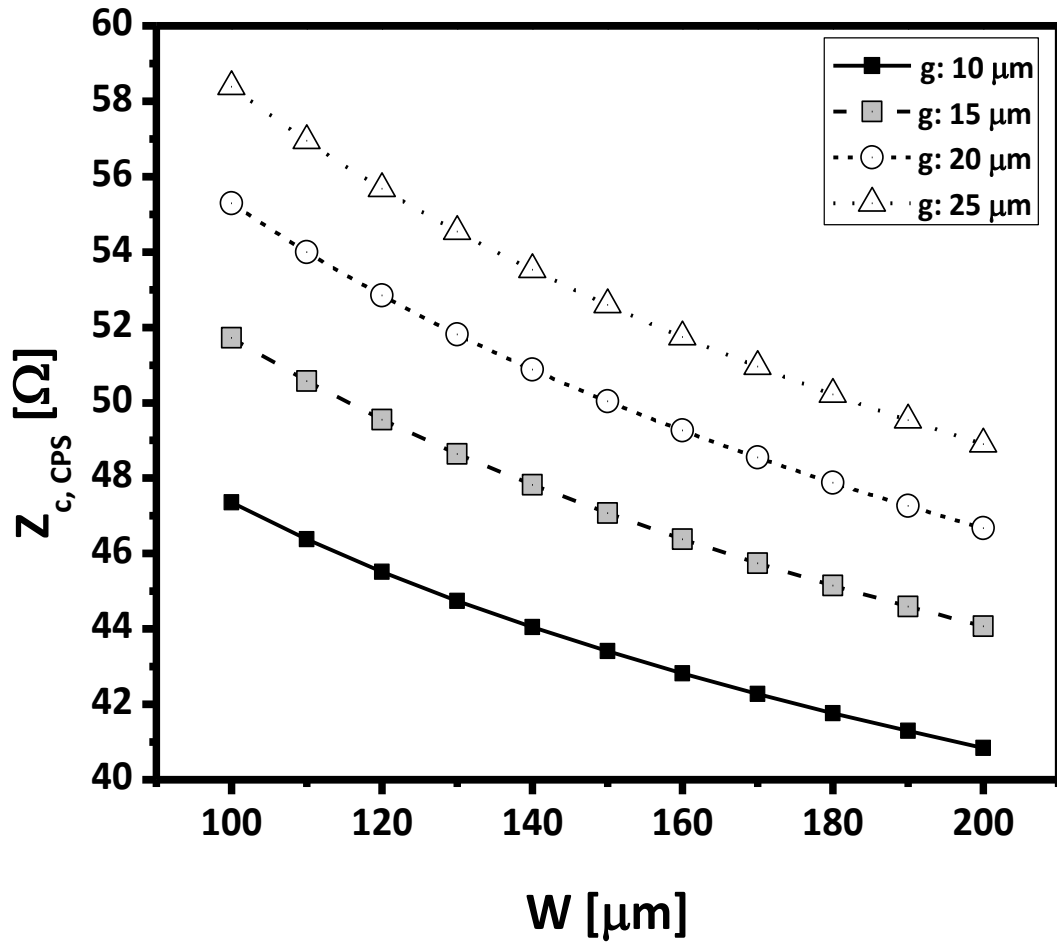


Figure 3.4 Quasi-static characteristic impedance of a co-planar strip (CPS) line as a function of the CPS line's width (W) for different air gaps (g): $\epsilon_r=12.9$ (Semi-insulating Gallium Arsenide), $h=450 \mu\text{m}$

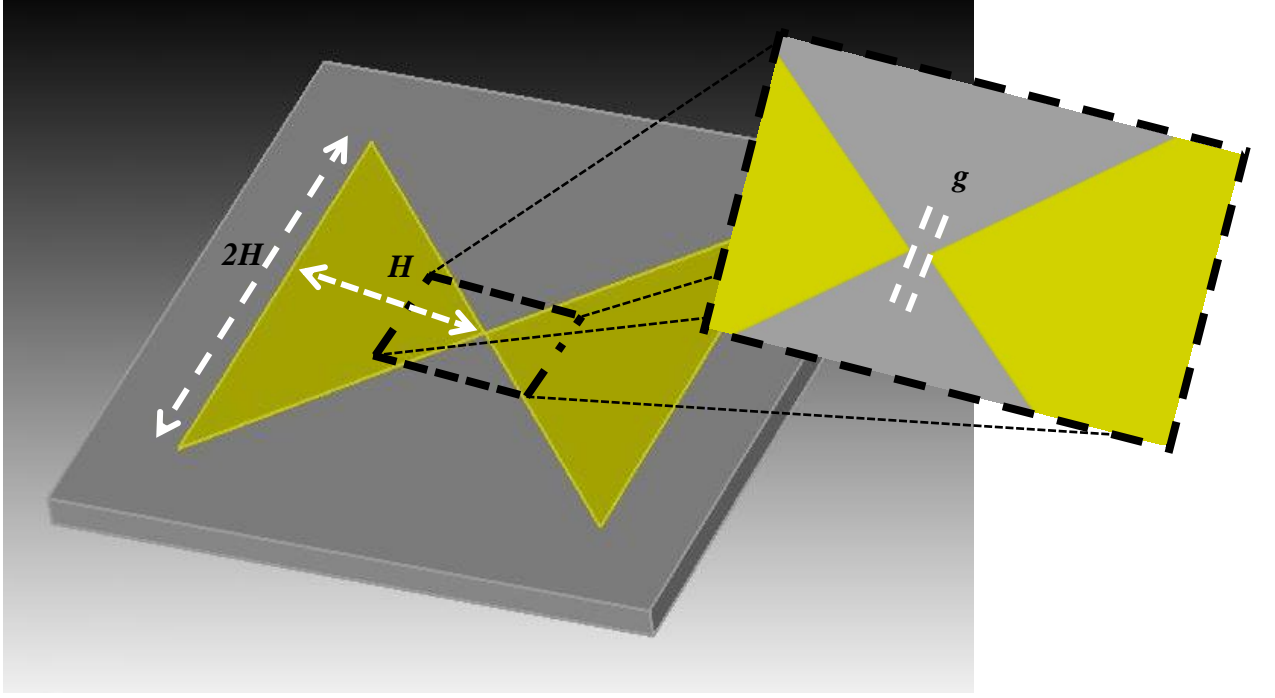


Figure 3.5 A bow-tie antenna with 90° flare angle. The height of a triangle is H and the base is $2H$. Two bows are electrically separated by an air gap ('g')

3.2 Two-port Simulation Technique into an Antenna Design

To determine the suitable height (H) of a triangle, we used the 2-port simulation technique. We can compute the $[S]$ -parameter data of a 2-port model of a bow-tie antenna using the electromagnetic (EM) software such as CST-MWS. Based on the calculated $[S]$ -parameters, the admittance $[Y]$ parameters of the bow-tie antenna can be determined by the following equations

$$[Y] = \frac{1}{D} \begin{pmatrix} (1 - S_{11})(1 + S_{22}) + S_{12}S_{21} & -2S_{12} \\ -2S_{12} & (1 + S_{11})(1 - S_{22}) + S_{12}S_{21} \end{pmatrix}$$

Where $D = (1 + S_{11})(1 + S_{22}) - S_{12}S_{21}$. In general, all two-port networks can be categorized with either a T or a π -network. In this research, we used the π -network to analyze the

simulation result. With previously computed [Y]-parameters, the series and parallel admittances (YY_s , YY_p) are calculated by the following equation.

$$YY_s = -y_{21}$$

$$YY_p = y_{11} + y_{21}$$

Next, the impedances are established by the inverse relation of YY_s and YY_p .

$$ZZ_s = 1 / YY_s$$

$$ZZ_p = 1 / YY_p$$

The π -network model with the impedances of a bow-tie antenna is shown in Figure 3.6.

By using this technique, the complex network models are simplified and easily analyzed.

In Figure 3.7, the various impedances of the π -network are provided as a function of frequency range over 8-to-12 GHz for various heights (H) of an antenna. Its result at 10 GHz is tabulated in Table 3.1.

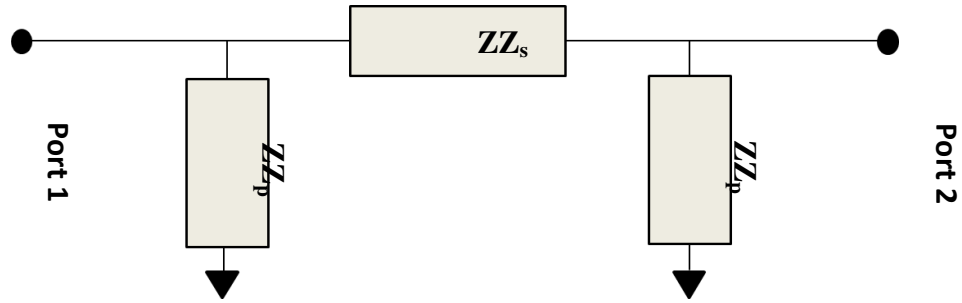


Figure 3.6 Impedance π -network model of a bow-tie antenna

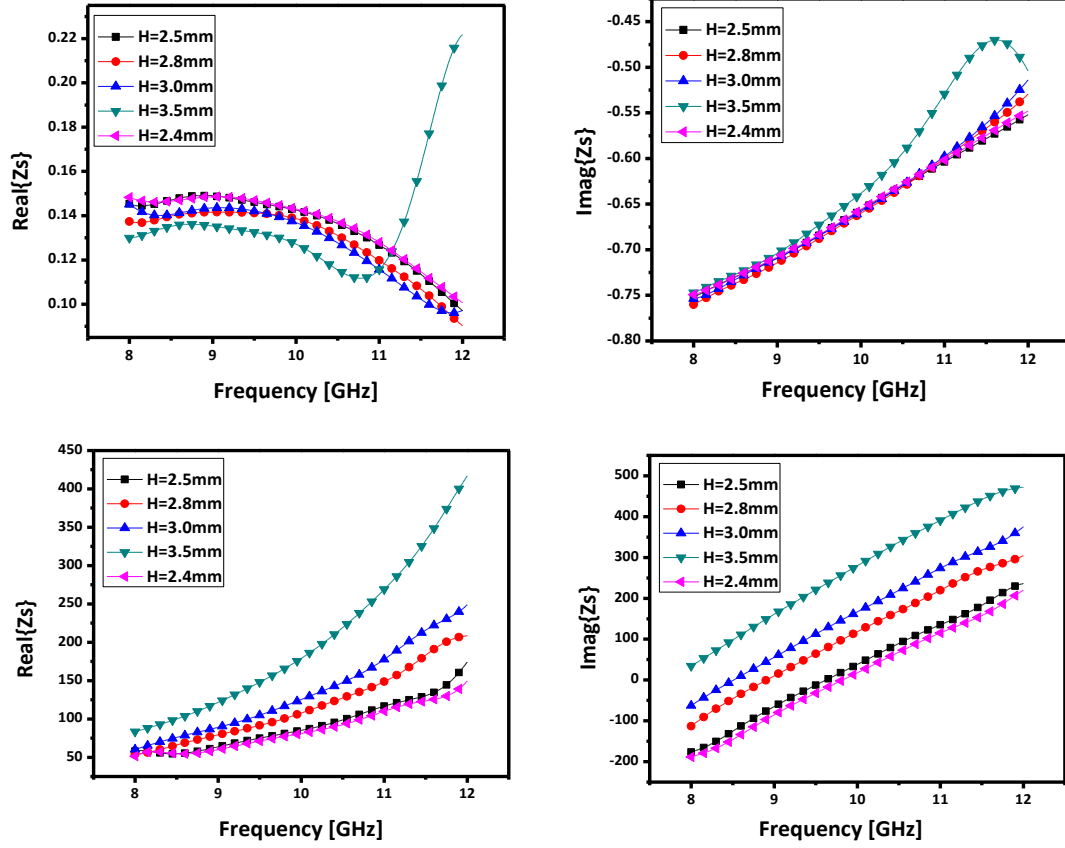


Figure 3.7 Computed impedance of a bow-tie antenna for various triangle heights

Bow height [mm]	ZZ_s [Ω]		ZZ_p [Ω]	
	Real	Imaginary	Real	Imaginary
3.5	0.127	-0.638	179	279.7
3.0	0.137	-0.657	125.35	167
2.8	0.139	-0.658	107.7	118.2
2.5	0.143	-0.660	85.15	37.1
2.4	0.143	-0.656	81.1	17.635

Table 3.1 Impedances of a bow-tie antenna for different bow heights

From the numerical results in Table 3.1, the series impedance (ZZ_s) of an antenna at 10 GHz can be considered to be negligible compared to the parallel impedances (ZZ_p). In addition to that, it is also notified that the imaginary of ZZ_p decreases along the smaller

bow height. For $H=2.4\text{-mm}$, the initially proposed π -network is simplified to the network model in Figure 3.8 (a). The impedance of a simplified network model is to be the half of that of the parallel components in π -network. Therefore, the impedance of network is $ZZ_p = 81.1 + j17.635$. And its corresponding lumped model is presented in Figure 3.8 (b).

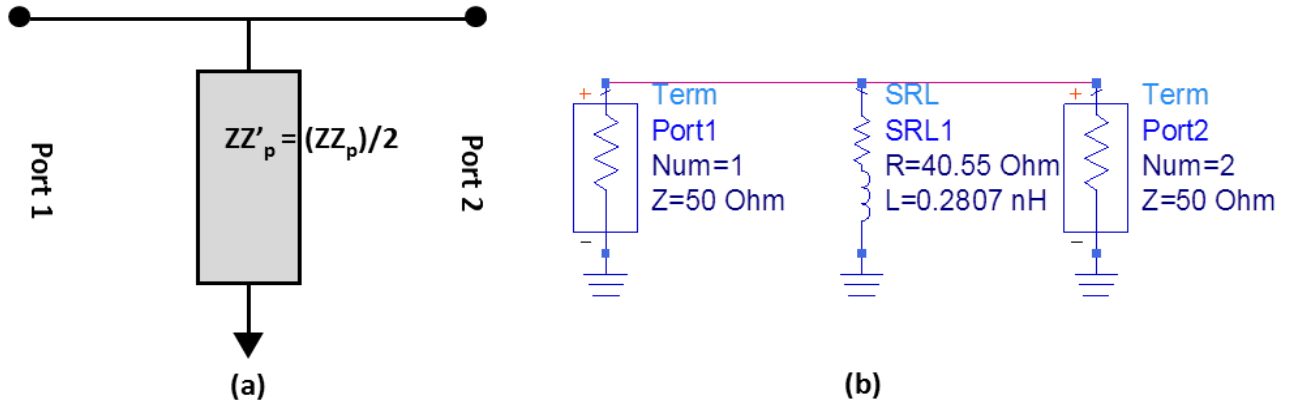


Figure 3.8 (a) Simplified π -network model **(b)** Equivalent lumped circuit

model of a bow-tie antenna

With determined dimensions of the bow-tie antenna; $H = 2.4\text{ mm}$, $\theta = 90^\circ$ and $g = 20\text{ }\mu\text{m}$, the return loss of the antenna is simulated and plotted on the smith chart. The simulated result on smith chart demonstrates that the antenna impedance is well matched to $50\text{ }\Omega$ at 10 GHz .

○	8.000 (11.92, -68.51) Ohm
□ ₁	10.00 (36.78, 6.922) Ohm
●	12.00 (146, 88.51) Ohm

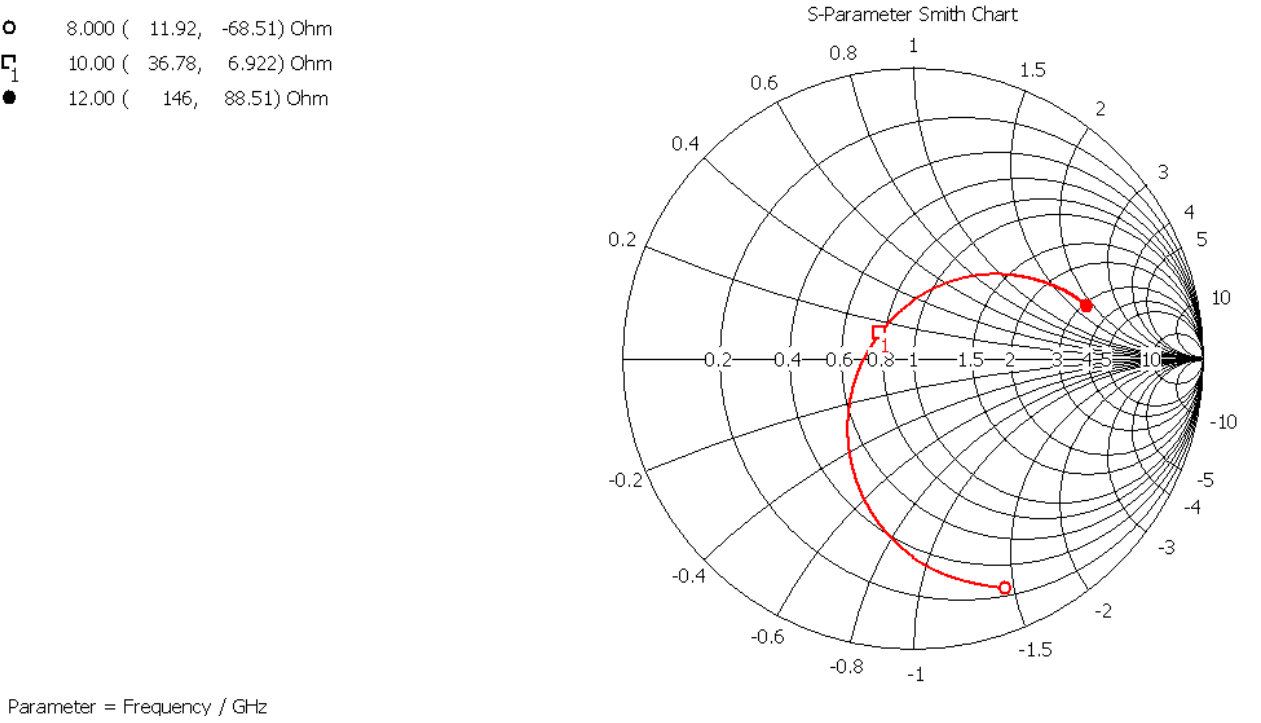


Figure 3.9 Return loss plot on the Smith chart

3.3 Fabrication Process and Hybrid Integration with a QDMLL

Details on the fabrication method are presented in this section. According to the designed dimensions, we built a bow-tie antenna with the photolithographic method. One good advantage of the photolithography is to be able to pattern the small structure in the order of μm on the substrate and its accuracy is also guaranteed. The whole fabrication procedures for the QDMLL-integrated-bowtie antenna are presented in Figure 3.10. As a beginning step, a thick layer (450 μm) of SI-GaAs was prepared as a substrate. The wafer cleaning process is sequentially to soak wafers into acetone, methanol and isopropyl alcohol (I.P.A) for 5 min for each material. After UV laser beam exposure on the surface of the negative photoresist (PR) coated on SI-GaAs, the desired bow-tie antenna pattern is printed. Since we first used the negative type of PR, the photoresist on the antenna

image is removed by the development process. Next, thin films of Ti ($0.05\mu\text{m}$) and Au ($0.3\mu\text{m}$) are deposited atop the PR layer by an e-beam metal evaporation. With help of the thin Ti layer, the deposition of the gold layer is better stuck on the substrate. A bow-tie antenna is finally constructed by a lift-off process. The lift-off process takes the PR away on the surface thereby removing undesired geometries from the substrate. The QDMLL is combined with an antenna through the chip-to-chip bonding method. A thick ($> \sim 1\mu\text{m}$) indium layer is introduced to bond a laser chip on the designed antenna surface. Because the electrical conductivity of an indium is in the order of 10^6 [S/m] [4], the indium layer can be used as the adhesive without affecting the condition of electrical properties of device. By applying the same procedures from an antenna fabrication, the indium post is prepared to mount a laser chip. Instead of using e-beam deposition machine, we used the thermal metal evaporator for this layer. It is mainly due to the deposition rate of the thermal evaporator is much higher than that of an e-beam deposition method. After constructing the thick indium post, a QDMLL is bonded on the one side of bow by placing it atop of an indium layer and applying heat to the layer. As a final step of the integration, an absorber of a QDMLL is connected on the other side of a bow-tie antenna via wire-bonding. The prototype of an integrated antenna was made according to the procedure.

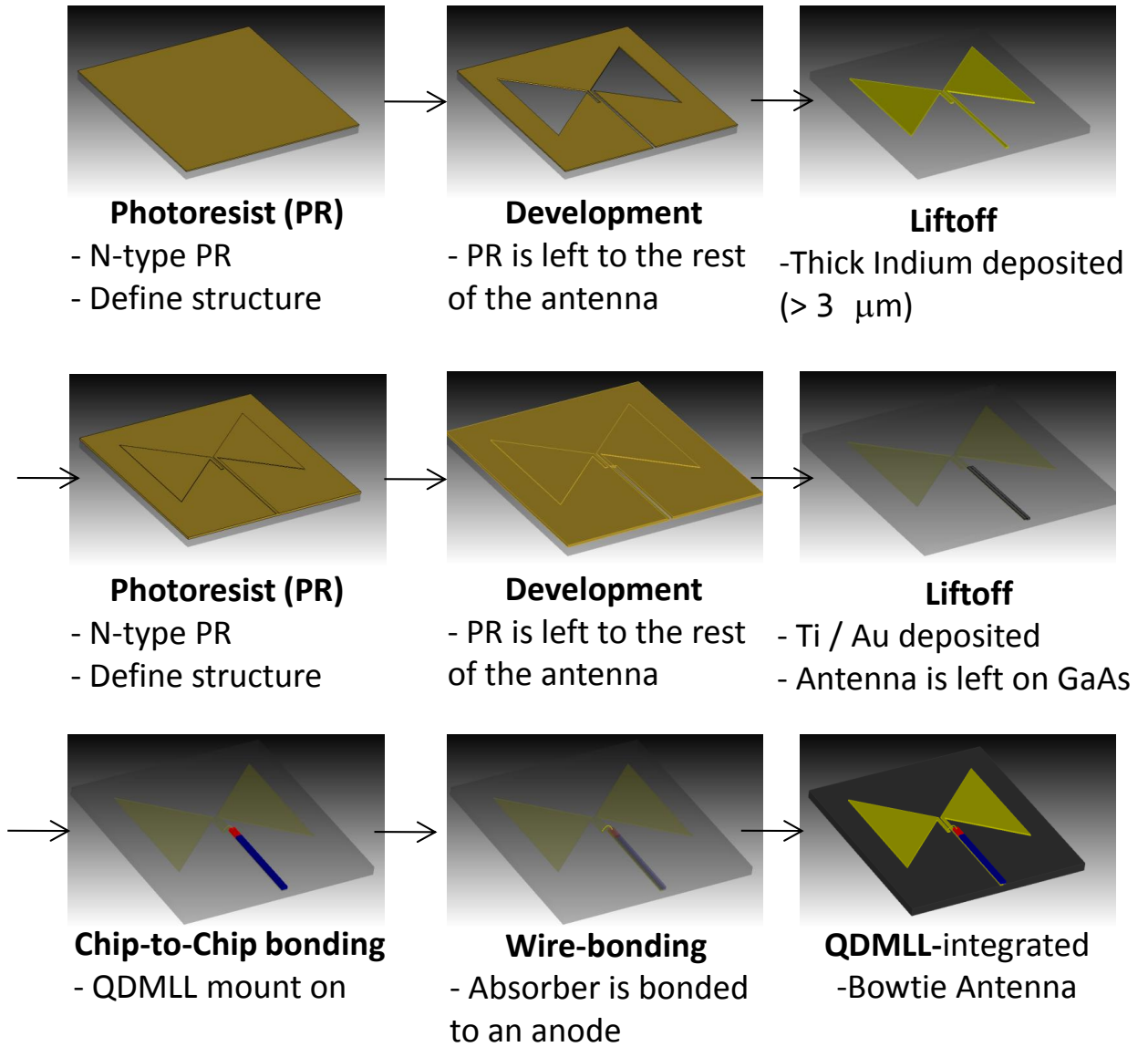


Figure 3.10 Fabrication procedures for the QDMLL-integrated-bowtie antenna

3.4 Characterization of the QDMLL-integrated-Antenna

This section presents setup for the characterization of an integrated antenna and its results. The characterization includes the return loss and emission from the fabricated antenna. For measuring return loss of an antenna, the on-wafer RF probe is used as

demonstrated in Figure 3.11. The RF-probe has the signal-ground configuration, which is apart by the 140- μm pitch. The fabricated module is placed on a copper heat-sink, then the RF-probe contacts on an antenna. The return loss of an antenna is measured by an HP8722D vector network analyzer. To remove the undesirable back scattered effects by a metal sub-mount, the microwave absorbing form is placed underneath of an antenna.

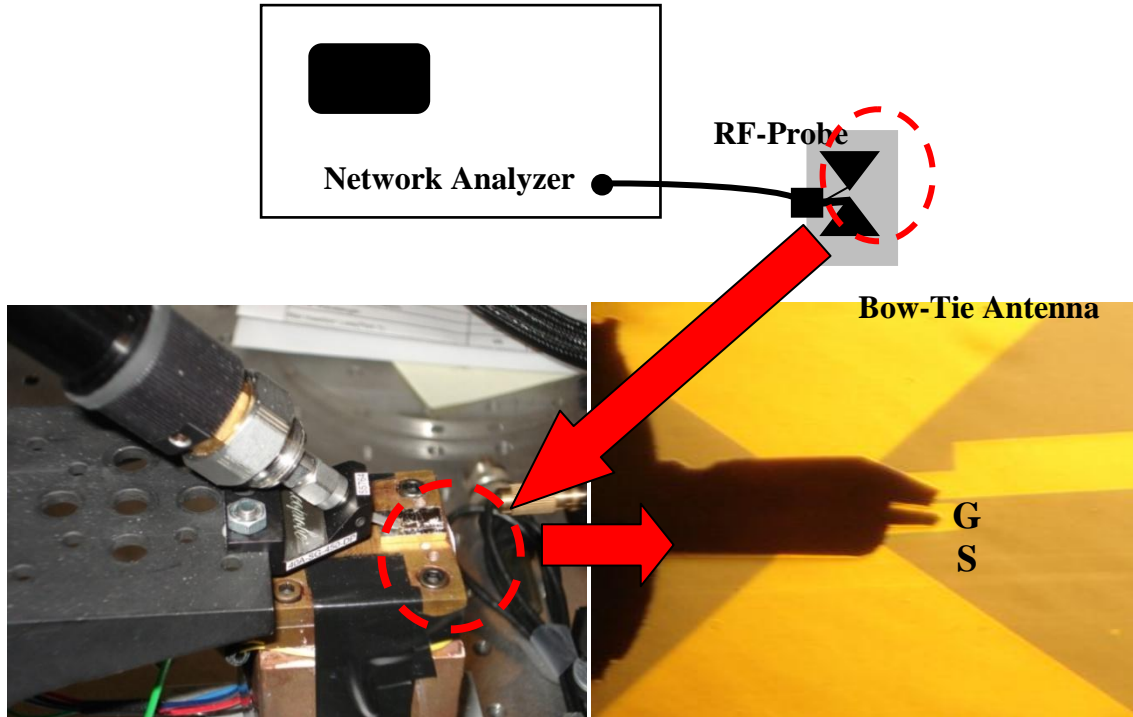


Figure 3.11 Return loss measurement setup: network analyzer (HP 8722D), 140 μm pitching microwave-probe.

The measured return loss in dB is compared with the simulation result in Figure 3.12. In the result, the resonance frequency appears higher than the 10 GHz. In general, the longer timing of an exposure to the UV laser beam causes the printed image on the PR to be decreased. Thus, it results in the resonance frequency. Although the resonance frequency of the lowest return loss is higher than 10 GHz, its return loss is still less than -

10 dB. The QDMLL-united active bow-tie antenna is made by following the procedure demonstrated in Figure 3.10.

The setup for the emission measurement out of the integrated antenna module is shown in Figure 3.13. The antenna module under the test is placed on the copper-heat sink which controlled by the temperature controller. Since the QDMLL sensitively operates by the temperature, the sub-antenna heat controlling unit is importantly required. The operation of the QDMLL is controlled by the power supplies. As a receiving / scanning antenna, we use the X-band (8-12 GHz) horn antenna. The radiated power intensity is monitored though the spectrum analyzer. In Figure 3.14, the measured result of radiation intensity is appeared at 10 GHz. With the measured emission out of an integrated transmitting module, the QDMLL is verified as the feasible compact microwave source. The attempt to improve its radiated power will be discussed in the following chapter.

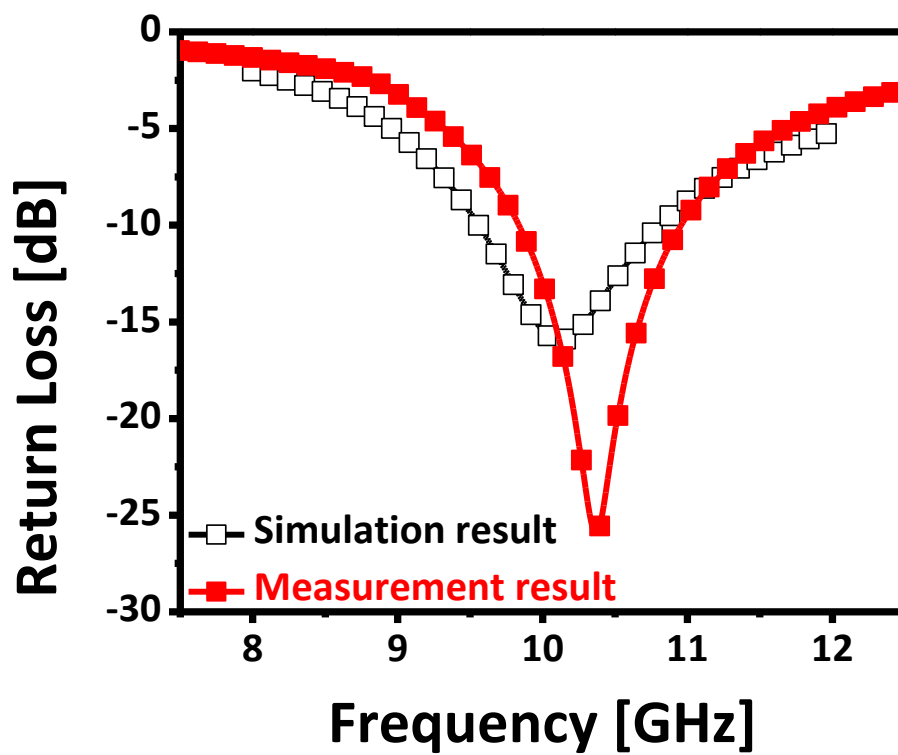


Figure 3.12 Comparison between the measured return loss and simulated one

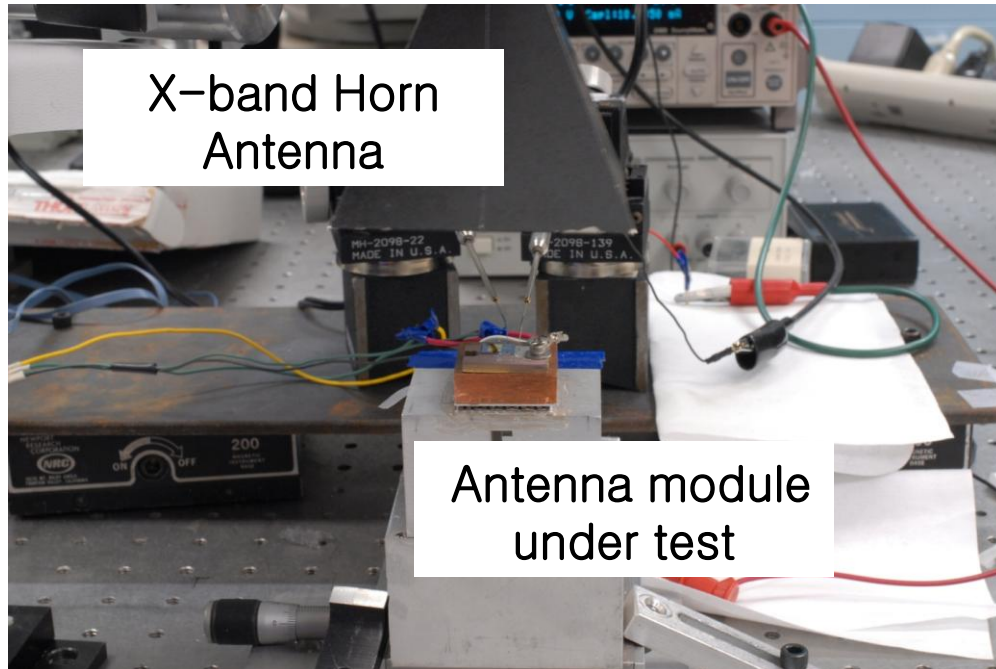


Figure 3.13 Measurement setup for the emission out of an integrated active antenna

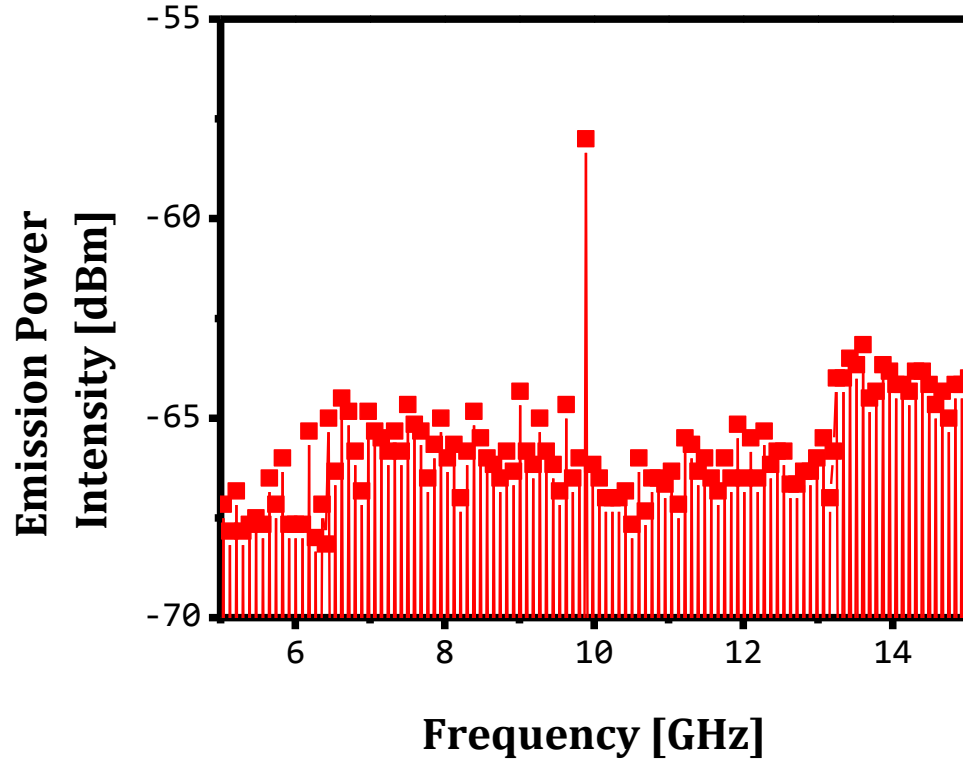


Figure 3.14 Measured emitting power intensity out of the QDMLL-integrated-bowtie antenna

3.5 Pattern Estimation of a Microstrip Antenna Integrated with QDMLL

The radiation pattern of a QDMLL-integrated-antenna is estimated in this section. From the previous part of this chapter, we have measured the emission power intensity using a bow-tie antenna at $\theta=0^\circ$, $\phi=90^\circ$. The proper operation of a QDMLL requires the Peltier-type temperature controller that results in a large metalized surface under the MLL chip. Due to its environment, a microstrip-type antenna accommodates this requirement better than a bow-tie antenna. The antenna proposed here is designed to

couple to 10 GHz, which is the fundamental repetition rate of the 4.1 mm-long QDMLL. As a base substrate, a 450 μm -thick semi-insulating GaAs is used. The size of the rectangular patch is designed to be 5.1 mm wide and 4.45 mm long. As a compared result in Figure 3.15, the measured return loss is in good agreement with the simulated result at 10 GHz. The electrical signal optically generated in the SA of the QDMLL is connected to the patch antenna via wire bonding. Then, the radiated signals are scanned by a horn antenna at different angles; $(\theta=0^\circ, \phi=90^\circ)$, $(\theta=45^\circ, \phi=90^\circ)$ and $(\theta=45^\circ, \phi=90^\circ)$. Figure 3.16 depicts the experimental setup, consisting of an RF-spectrum analyzer (*Agilent 8565EC*), voltage/current sources, and an X-band horn antenna. Three different biasing conditions including $(I_{\text{app}}: 100\text{mA}, V_{\text{app}}: -1\text{V})$, $(I_{\text{app}}: 120\text{mA}, V_{\text{app}}: -1\text{V})$ and $(I_{\text{app}}: 150\text{mA}, V_{\text{app}}: -1.5\text{V})$ are applied on the QDMLL. The X-band horn antenna is used as a receiving antenna and is vertically located above the fabricated patch antenna. Its straight-line distance between the patch and horn antenna is 3 cm. Figure 3.17 presents the measured RF spectra of the emission power intensity of the QDMLL-integrated-patch antenna for various angles. In Figure 3.17(a), a QDMLL is biased by $V_{\text{app}}: -1\text{V}$, $I_{\text{app}}: 100\text{mA}$. The received emission power intensities are recorded as -64.33-dBm for $\theta=0^\circ$, $\phi=90^\circ$, -66.5-dBm for $\theta=\pm 45^\circ$, $\phi=90^\circ$ and -66.48-dBm for $\theta=\pm 90^\circ$, $\phi=90^\circ$. With the evaluated radiation intensities, the signal-to-noise ratio (SNR) is calculated by subtracting the maximum power intensity from the noise level. For instance, $\text{SNR} = -64.33 + 76.4615$ (dBm) = 12.1315-dB for $\theta=0^\circ$, $\phi=90^\circ$. Likewise, SNRs for different angles are also computed. For the different biasing conditions, the computed SNRs are presented in Table 3.2. According to the table, the highest radiation power is observed at the angle of $\phi=90^\circ$ and $\theta=0^\circ$.

SNR [dB]		-1V / 100mA	-1V / 120mA	-1.5V / 150mA
$\phi=90^\circ$	$\theta=0^\circ$	<i>12.13</i>	<i>11.31</i>	<i>13.98</i>
	$\theta=\pm 45^\circ$	<i>11.31</i>	<i>10.95</i>	<i>11.50</i>
	$\theta=\pm 90^\circ$	<i>10.41</i>	<i>10.77</i>	<i>10.05</i>

Table 3.2 Signal-to-noise ratio (SNR) for different biasing conditions.

The computed SNR values in Table 3.2 are normalized to the maximum SNR. With the normalized signal-to-noise ratios in Table 3.3, the 2Dradiation pattern on the XY-plane can be plotted as shown in Figure 3.18.

Normalized SNR [dB]		-1V / 100mA	-1V / 120mA	-1.5V / 150mA
$\phi=90^\circ$	$\theta=0^\circ$	<i>0</i>	<i>0</i>	<i>0</i>
	$\theta=\pm 45^\circ$	<i>-0.82</i>	<i>-0.36</i>	<i>-2.48</i>
	$\theta=\pm 90^\circ$	<i>-1.72</i>	<i>-0.54</i>	<i>-3.93</i>

Table 3.3 Normalized signal-to-noise ratio (SNR) for the different biasing conditions.

The measured estimated emission patterns for different biasing conditions are compared with the simulated result in Figure 3.18. From the plot, it can be observed that the radiation pattern for the different biases is nearly similar. In addition, the simulated result shows good agreement with the experimental results under various biasing conditions.

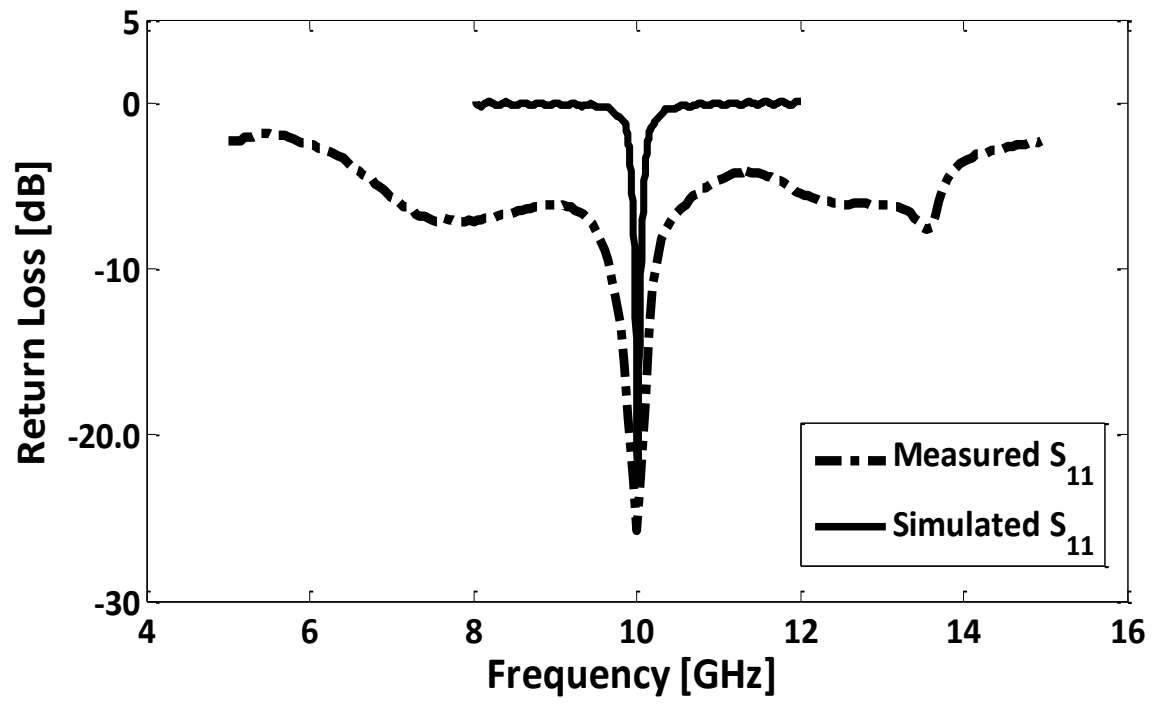


Figure 3.15 Measured and simulated return losses of a fabricated microstrip antenna

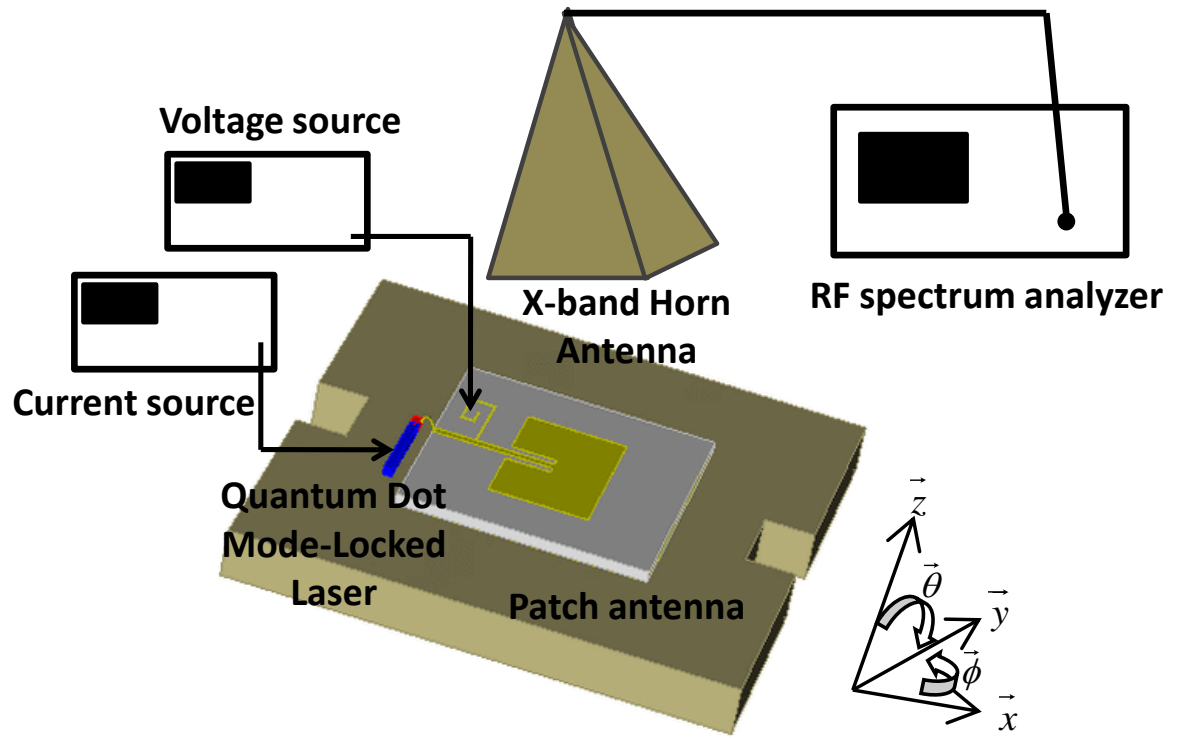


Figure 3.16 The experimental setup for the emission pattern estimation

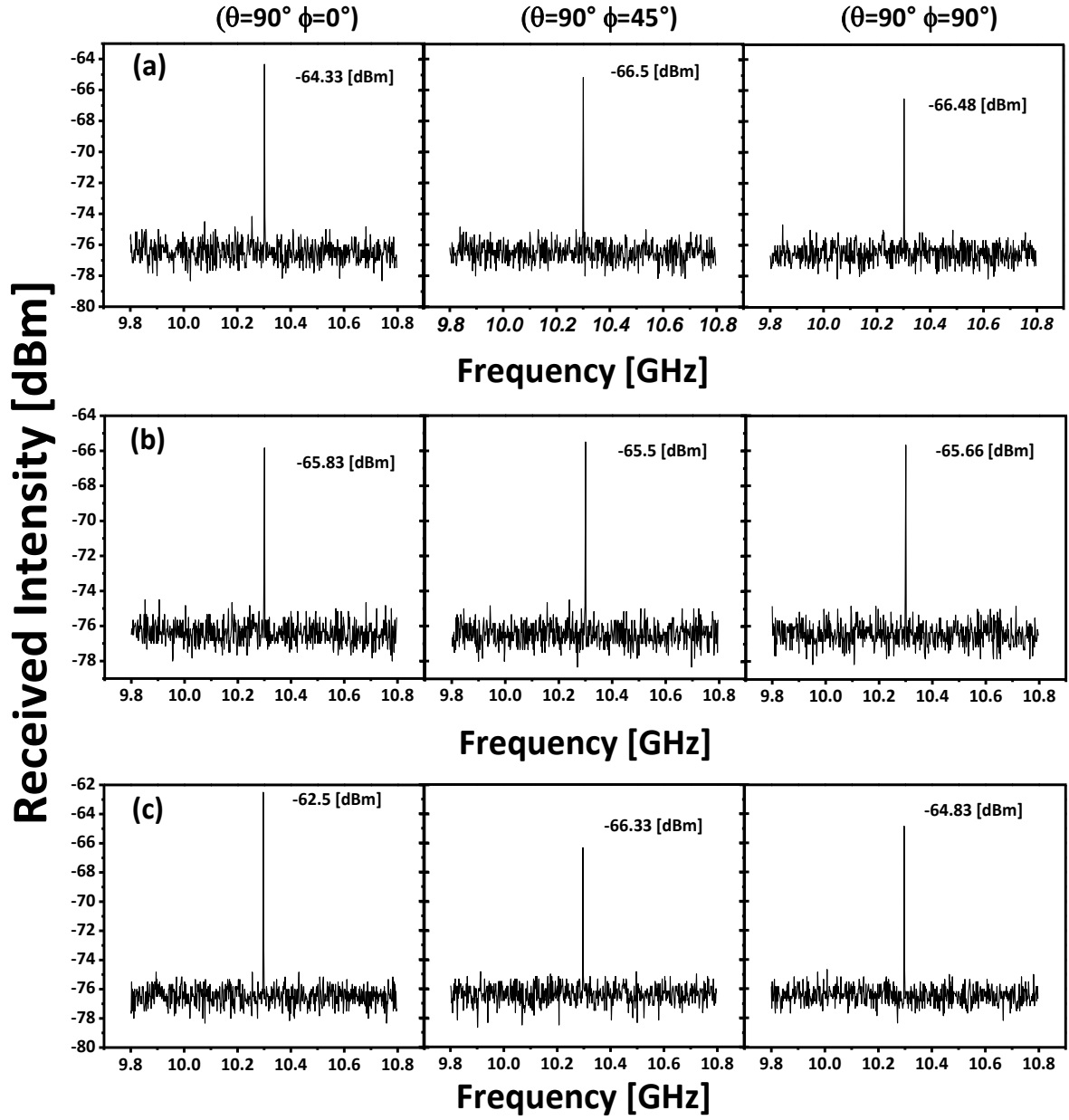


Figure 3.17 RF power spectrums of the radiation intensity
for different biasing conditions.

(a) -1V, 100 mA

(b) -1V, 120 mA

(c) -1.5 V, 150 mA

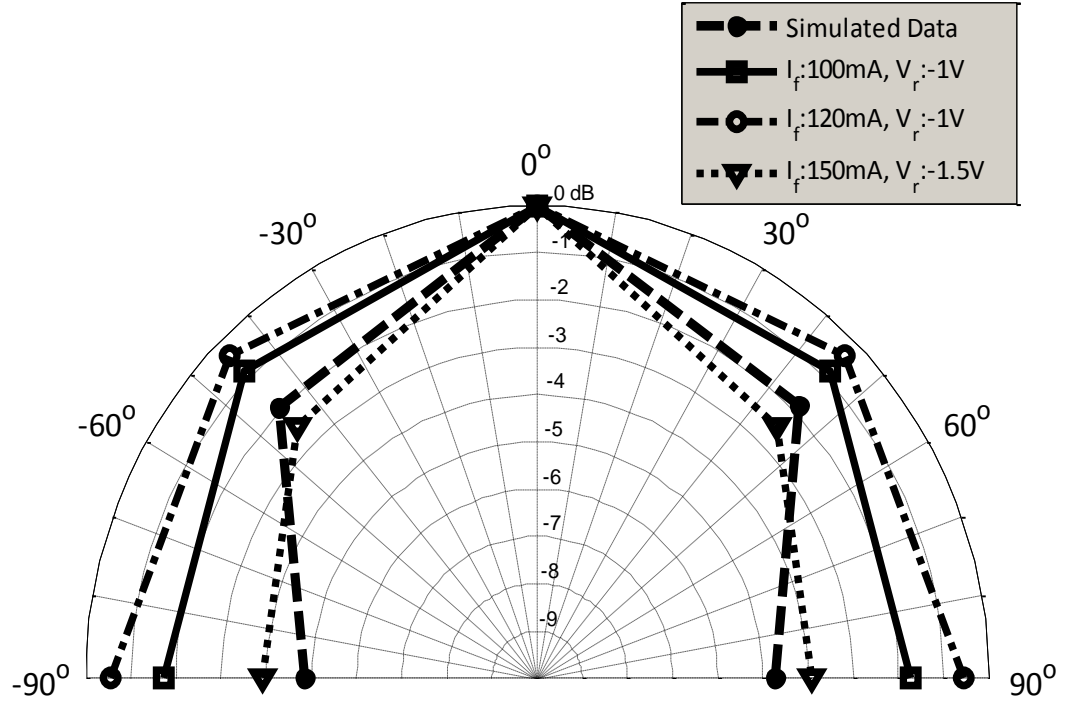


Figure 3.18 Comparison of the measured estimated emission patterns and simulated result

3.6 Summary

A co-planar strip line and a bow-tie antenna are fabricated and integrated with a 4.1-mm long QDMLL whose repetition rate is 10 GHz. We applied the π -network model to improve the efficiency in designing antennas. The photo-lithographic method is also used to fabricate the antenna and combine two devices. The two section passively mode locked laser is integrated with the fabricated prototype to measure the emission power. Based on the characterized results of an integrated module, the QDMLLs can be verified as possible compact microwave sources.

We characterized the estimated emission pattern out of the microstrip antenna integrated with a QDMLL. We performed the emission measurements by changing the biasing conditions and compared results with the simulation. The experimental result well agrees with the simulation. The results in this chapter support the concept of the QDMLL to be a feasible microwave source.

3.7 References

1. R.C. Compton, R.C. McPhedran, Z. Popovic, G.M. Rebeiz, P.P. Tong, and D.B. Rutledge, "Bow-Tie antennas on a dielectric half-space: Theory and Experiment," IEEE Transaction, Antennas and Propagation, Vol. 35, pp 622-631, February, 1987.
2. E. Chen, S.Y. Chou, "Characteristics of Coplanar Transmission Lines on Multilayer Substrate: Modeling and Experiments," IEEE Transactions on Microwave Theory and Techniques, Vol. 45, No. 6, June 1997.
3. CST Studio Suite 2010 (www.cst.com).
4. A. W. Smith, "The electrical conductivity of Indium and Thallium," The Ohio Journal of Science, Vol. XVI, No. 6, pp 244 – 247, April 1916.

Chapter 4

Integration with a Bowtie Slot Antenna at 10 and 20 GHz and Antenna Array

Beam-Steering by Biasing the QDMLL

4.1 Multi-resonance Bow-tie Slot Antenna

Here another design is presented that works at the first two harmonics (10 and 20 GHz). In Chapter 2, it was shown that the RF-spectra of the photocurrent (Figure 2.5), under the biasing conditions of V_{app} : -1V and I_{app} : 200mA contain second order harmonics. To extend the MLL's operating frequency range beyond the 10 GHz range, the bow-tie slot antenna is proposed. A co-planar wave guide (CPW) is used as the feed line for the antenna. ACPW is well developed and commonly used in the high frequency RF-applications since its characteristic impedance does not vary too much as a function of frequency

Based on the 450 μm thick SI-GaAs substrate, the CPW of the 0.3 mm-wide microstrip line and 0.2 mm-wide air gap has a 50 Ω characteristic impedance line. In Figure 4.1, the simulated value is approximately 50 Ω over the entire frequency range of interest. Figure 4.2 shows the simulated transmission (S21) and reflection (S11) of the 10mm-long CPW. From the figure, one can see that most of the input power is delivered to the load within the frequency range of interest. In order to obtain the suitable dimensions of an antenna, two-port simulation approach, previously introduced in Chapter 3, was used.

As mentioned in the beginning of this section, the antenna is designed to resonate at two frequencies; 10 and 20 GHz. The desired resonant frequency of a bow-tie slot antenna can be determined by $F_{\text{resonance}} = 2nF_0$ where $n = 1, 2, \text{ and } 3 \dots$ for

$\lambda/2$, $3\lambda/2$ and $5\lambda/2$. For instance, if $F_0 = 5$ GHz is chosen, the antenna can resonate at 10 and 20 GHz. The proposed antenna is shown in Figure 4.3. In the figure, the yellow component is the metal structure and the grey part of the geometry is the dielectric substrate. By employing the same manner in Chapter 3, the two-port simulation approach, explained in Chapter 3, was used to determine the unknown values of the bow-tie slot antenna including the size of bow base (B), and its height (H). With the values of $H = 10$ mm, $B = 8$ mm, Figure 4.4 presents the real and imaginary values of the series-impedance of the two-port model of a bow-tie slot antenna. The parallel-impedances are generally large enough to be regarded as an open circuit. Based on the simulated result, the fundamental resonance frequency (F_0) appears at 5GHz.

Next, stub lines were used to cancel the imaginary parts of input impedance of an antenna. The block diagram in Figure 4.5 shows the matching procedure using the ideal transmission (TX) line with a shorted stub line. For matching, the unknown values are required to satisfy the equation of $|Z_{ant} + jZ_{stub}\tan\theta| = |Z_0|$ where $Z_0 = 50 \Omega$, Z_{ant} is the calculated antenna impedance and Z_{stub} is the characteristic impedance of the stub line at 10 and 20 GHz. At both 10 and 20 GHz, the antenna resistances (R_{ant}) with $H = 10$ mm X $B = 8$ mm are approximately 50Ω . Thus, the equation is simplified to $X_{ant} + Z_{stub}\tan\theta = 0$ to meet the matching condition. Using the optimization tools in ADS [1], these unknown variables can be determined. For the calculated variables of $Z_0 = 75 \Omega$, $\theta_0 = 169^\circ$ at 10 GHz, the detail dimensions of an antenna are presented in Table 4.1. The schematic of the bow-tie antenna with a stub-line is also presented in Figure 4.6. The simulated return loss is shown for both cases; with and without impedance matching line. As shown in Figure

4.7, the antenna impedances at 10, 20 GHz are closer to the center of the smith chart when matching is applied. Figure 4.8 depicts this return loss on a rectangular plot.

Unit:

B	W_{cpw}	W_{stub}	G_{cpw}	G_{stub}	H	L_{stub}
<i>8.0</i>	<i>0.3</i>	<i>0.2</i>	<i>0.2</i>	<i>0.4</i>	<i>10.0</i>	<i>5.25</i>

Table 4.1 Dimensions of the proposed antenna

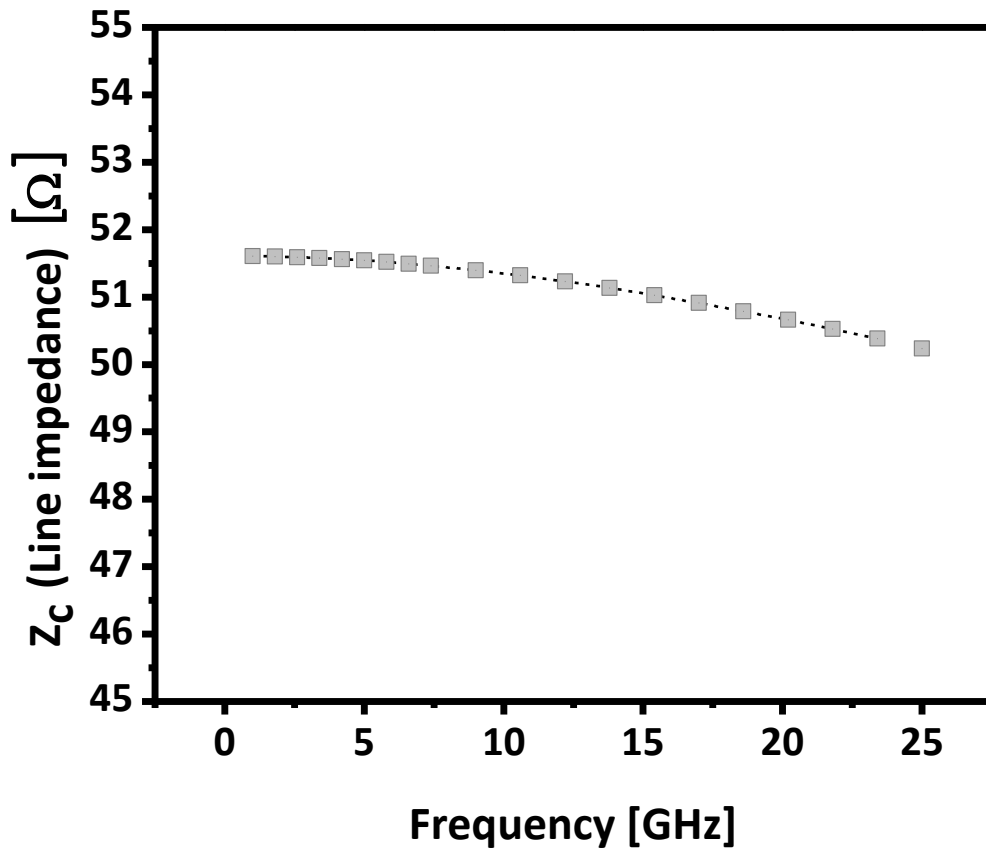


Figure 4.1 Characteristic impedance of CPW line of a 0.3 mm wide center microstrip line and 0.2 mm wide air gap

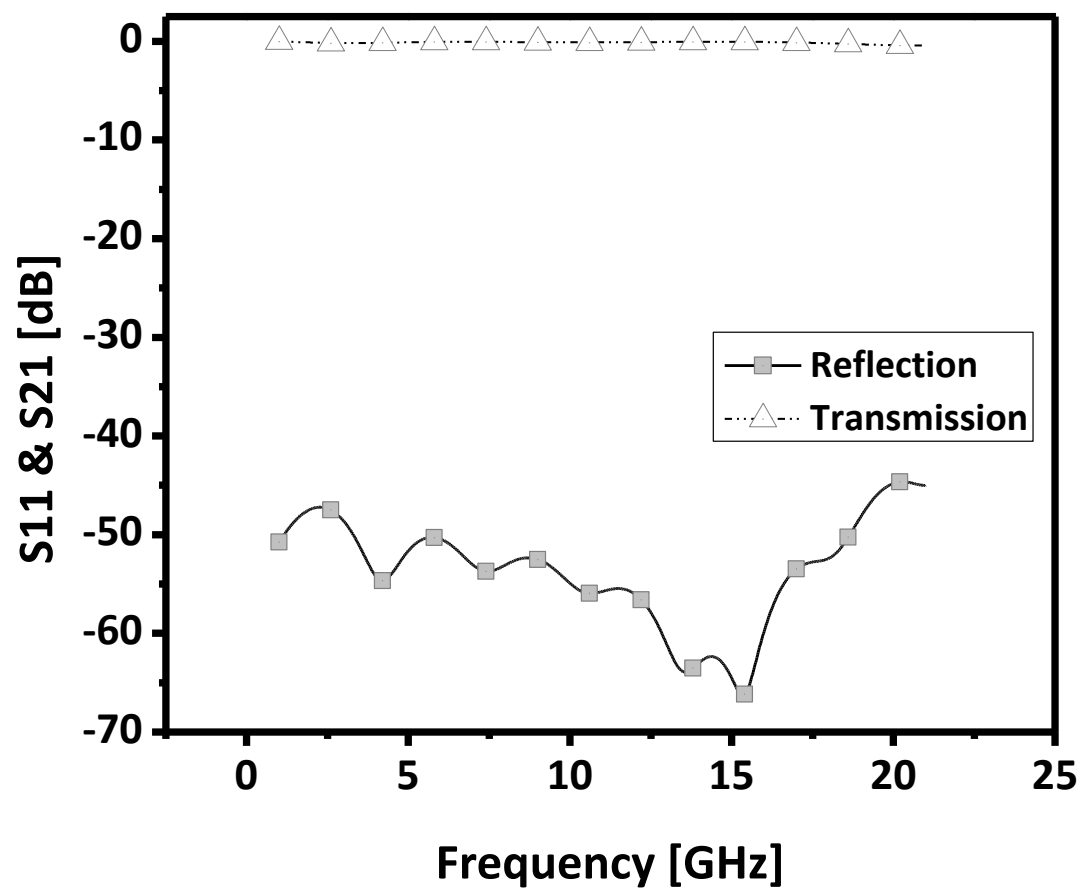


Figure 4.2A Computed transmissions (S21) and reflection (S11) of a 10mm long CPW.

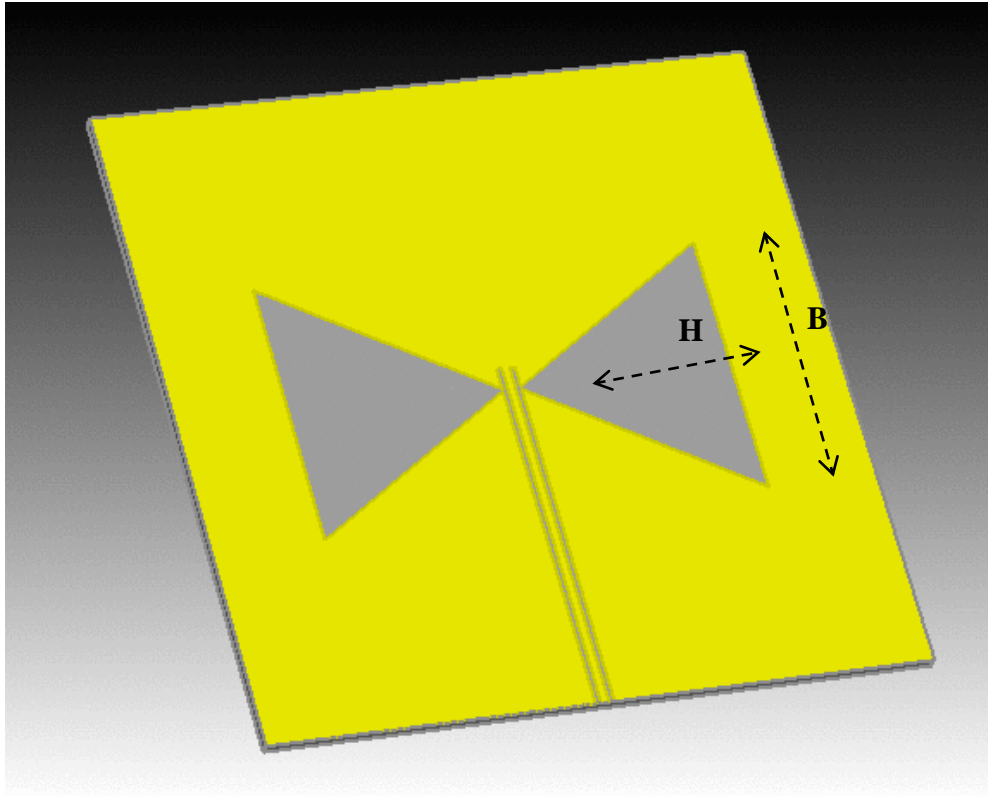


Figure 4.3A CPW fed bow-tie slot antenna; H: height of a bow, B: width of a bow

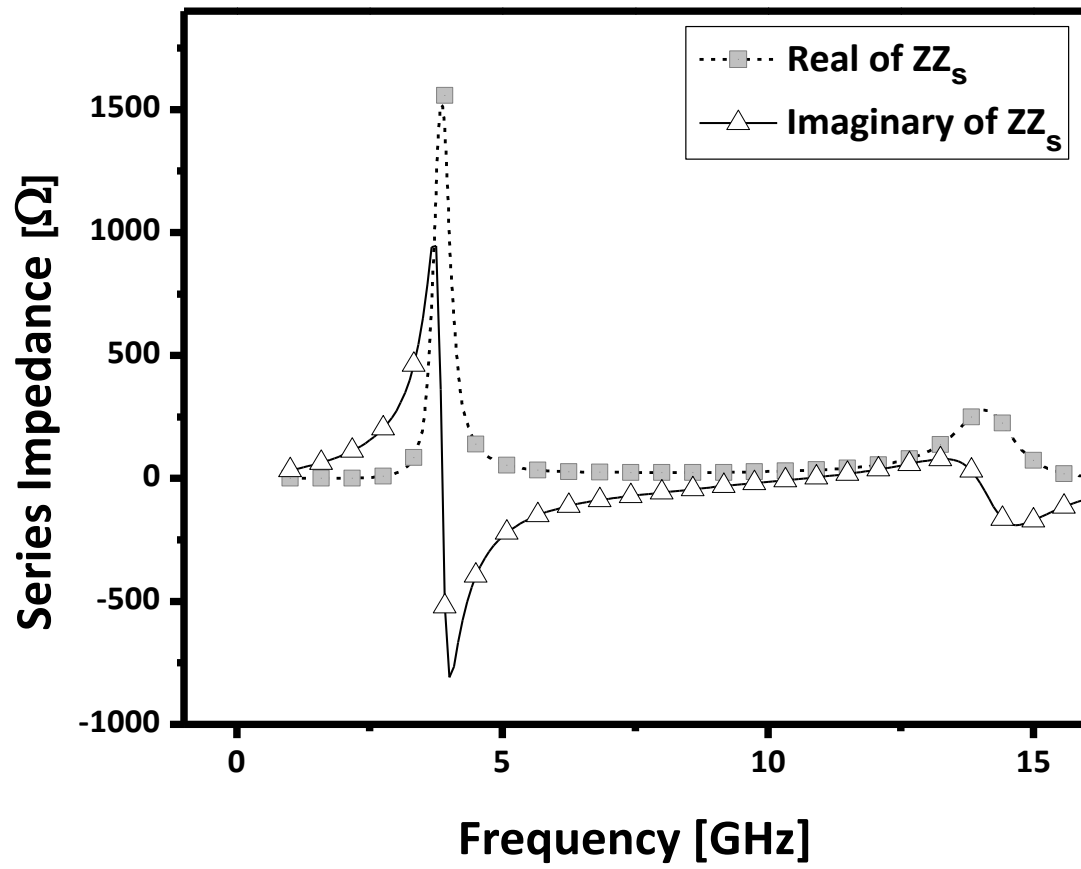


Figure 4.4 Simulated real and imaginary impedances of a bow-tie slot antenna

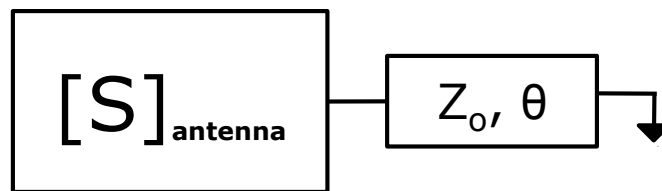


Figure 4.5 The block diagram of impedance matching

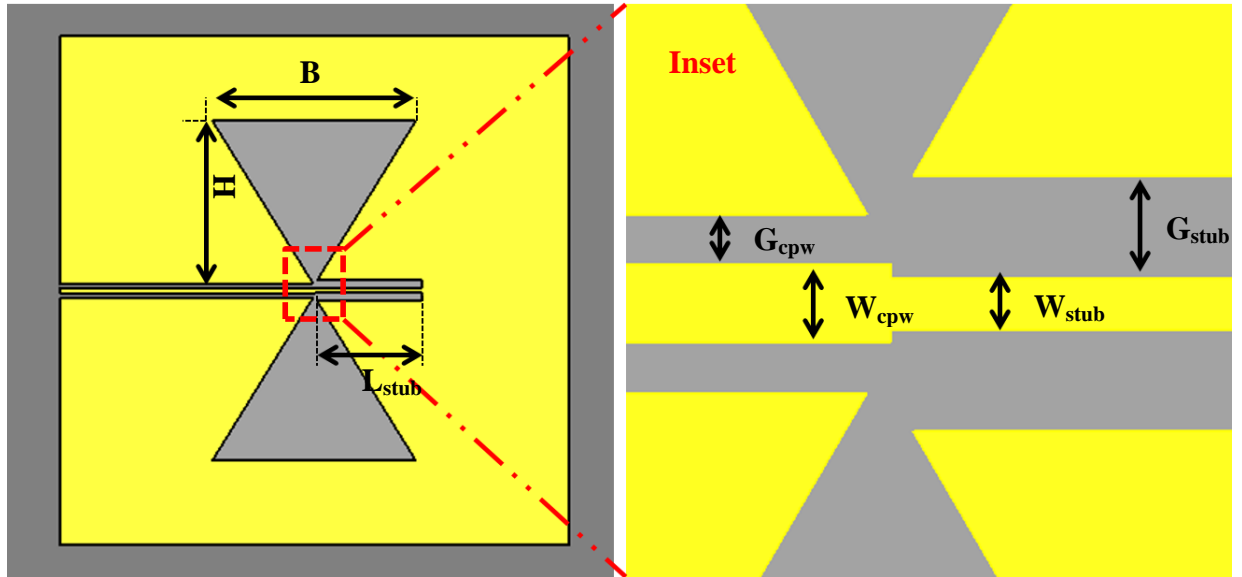


Figure 4.6 The bow-tie slot antenna with a short stub matching line

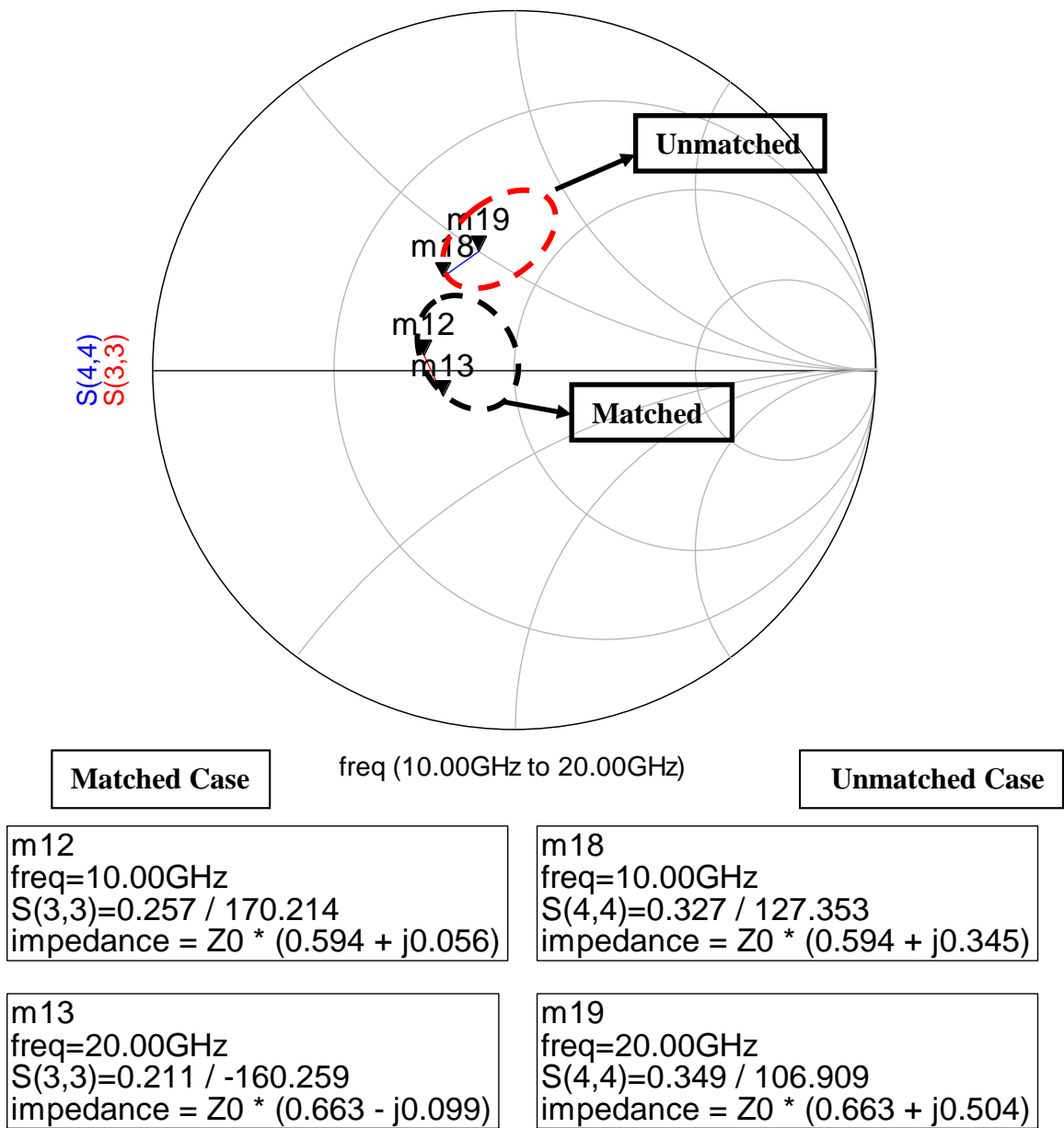


Figure 4.7 Impedances on the smith chart for both the matched and unmatched case

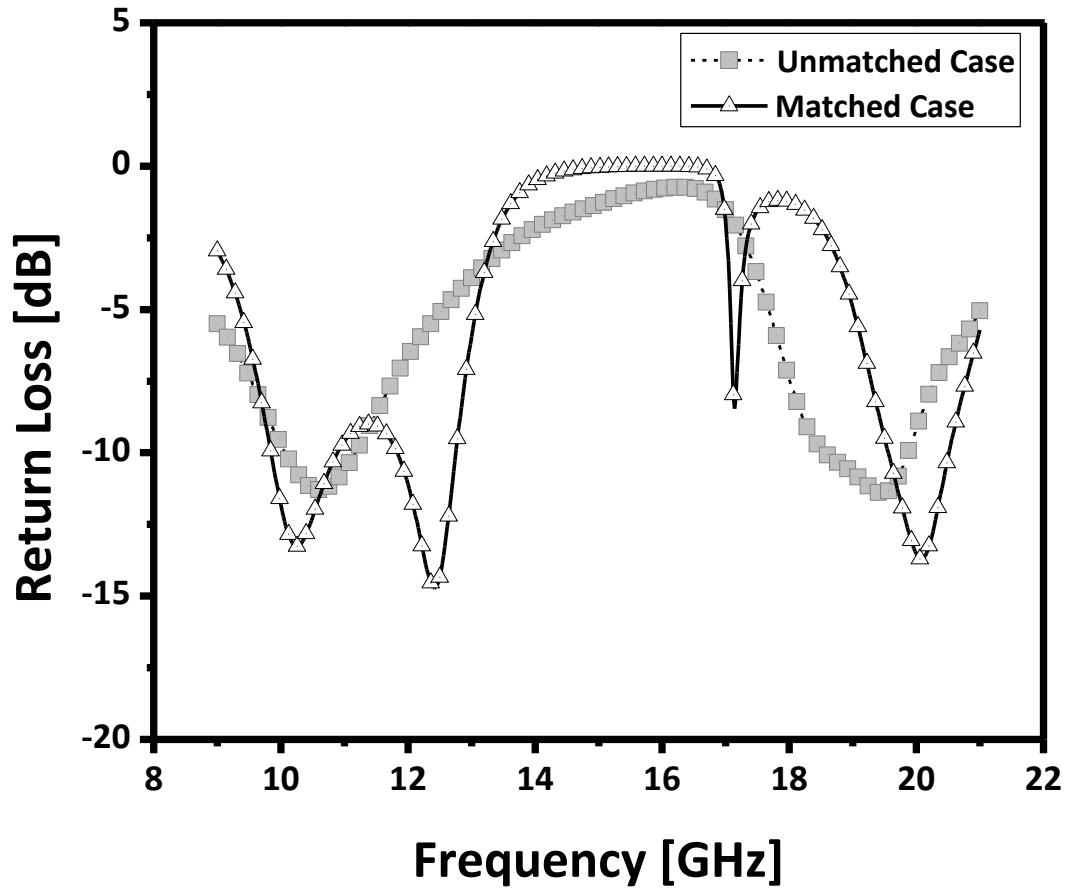


Figure 4.8 Return loss-comparison of the both matched and unmatched case

4.2 Antenna Fabrication and Measurement

As a substrate for the antenna, SI-GaAs substrate is used to achieve the seamless integration with the MLL. By using the same material, the laser chip and the antenna allows the monolithic fabrication of the entire RF/photonic device. To realize a 50Ω -characteristic impedance for the required CPW line, a line width of 0.3 mm and a gap of 0.2mm are used. All other dimensions of the proposed antenna are provided in Table 4.1.

The photolithographic method, shown in Figure 3.10, is employed to build the integrated prototype. Figure 4.9 shows the comparison of the measured and simulated S_{11} -results of the fabricated antenna. The measured and simulated results agree well at the first resonance frequency but not at 20 GHz (2nd resonance). This is because the dimension of the bowtie slot antenna is larger than the actual proposed design.

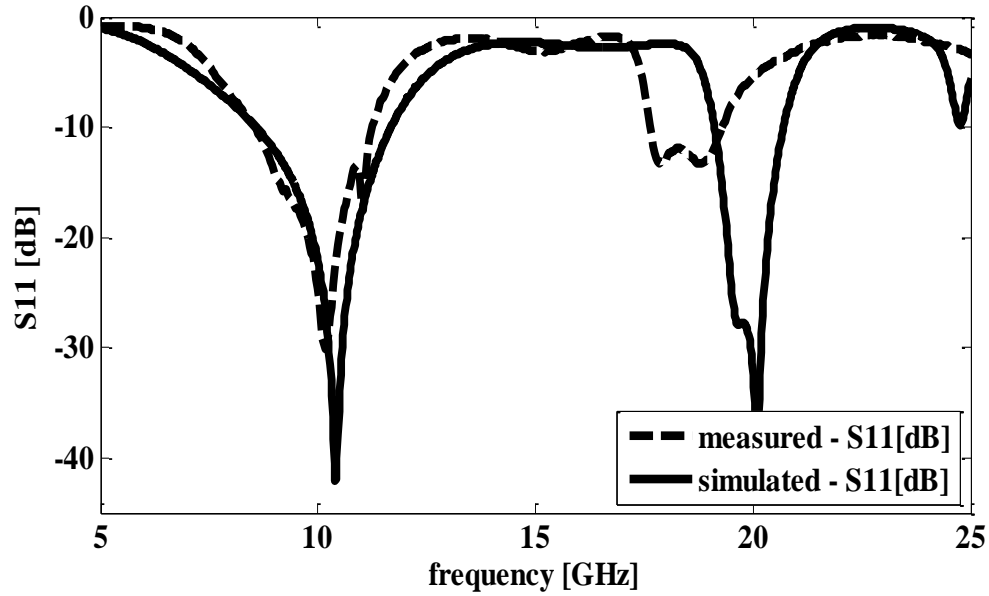


Figure 4.9 Simulated and Measured return losses of a bow-tie slot antenna

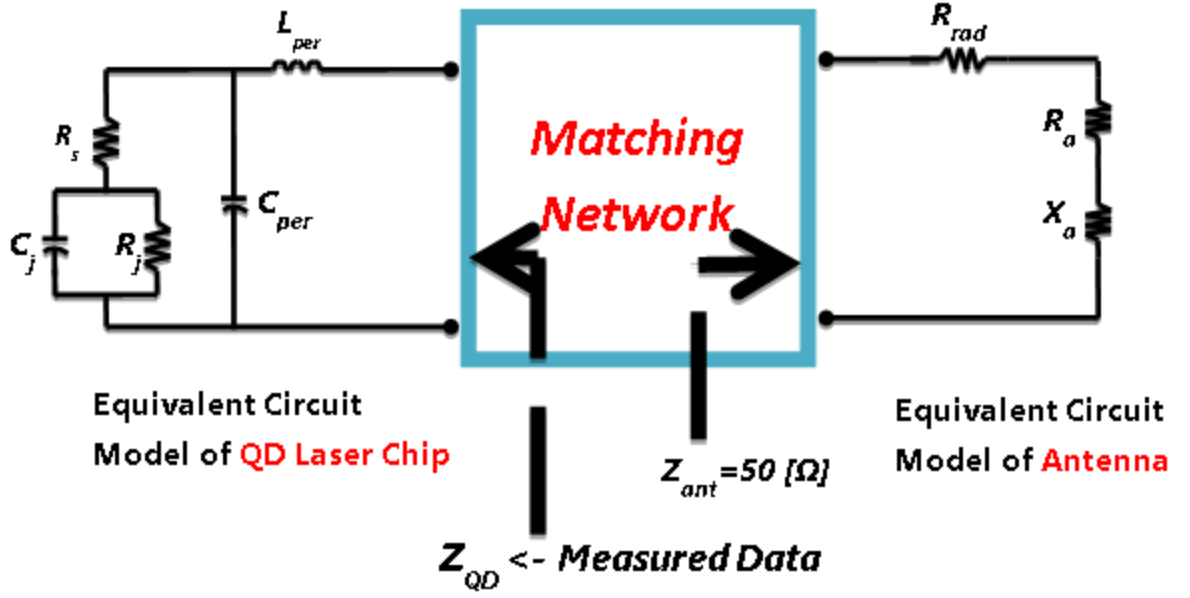


Figure 4.10 Equivalent circuit model of the matching circuit between a QDMLL and a bow-tie slot antenna; Z_{QD} : output impedance of a QD-MLL and Z_{ant} : impedance of a bow-tie slot antenna

4.3 Impedance Matching

To integrate with the bow-tie slot antenna in section 4.1.1 to the MLL, the impedance transformer is designed for 10 and 20 GHz; the first and second orders of harmonics based on the QDMLL's repetition rate. The diagram in Figure 4.10 demonstrates the equivalent lumped element model of the impedance transformer in between a saturable absorber in the MLL and the antenna. The S_{11} of the quantum dot (QD)-absorber is measured first over the frequency window ranging from 1 to 30 GHz. Based on the measured [S]-parameters and the output impedances of the absorber, one can recalculate Z_{QD} . In Figure 4.11, the saturable absorber impedance is plotted as the

function of reverse bias voltage at both 10 and 20 GHz. The values of tis impedance are also tabulated in Table 4.2.

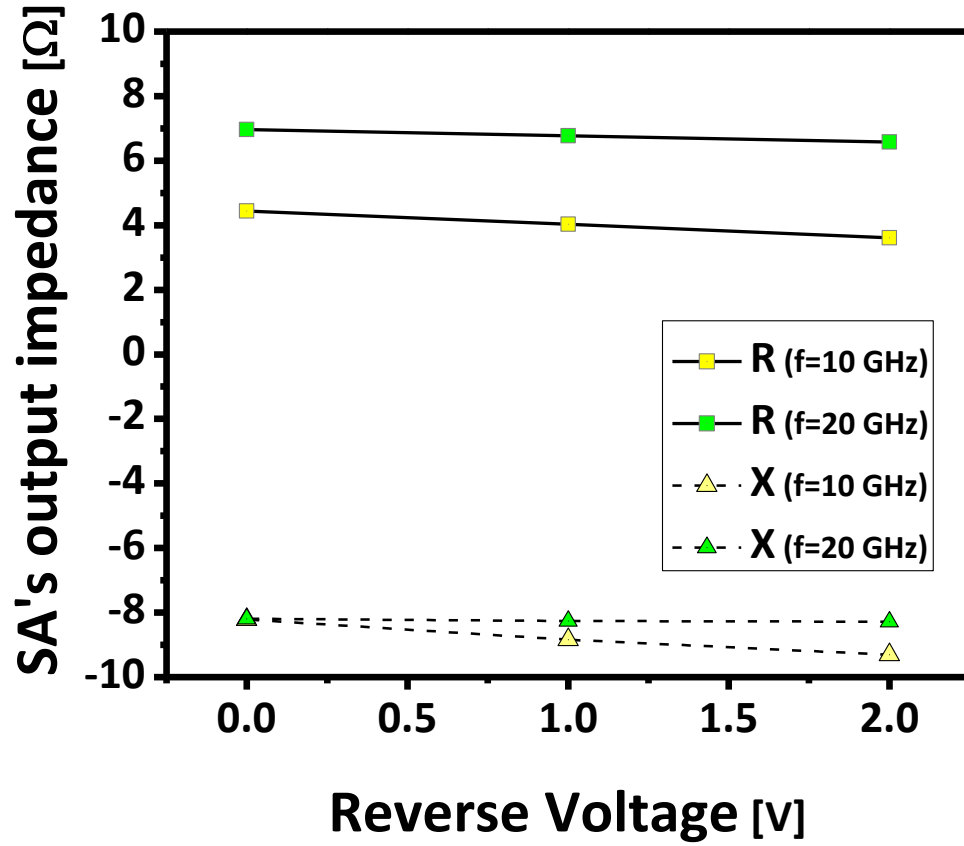


Figure 4.11 Measured output impedance of the saturable absorber in the QDMLL as a function of reverse biasing voltages

Case	Frequency [GHz]	Impedance [Ω]	S_{11} [dB]
Unmatched	10	$4.45-j8.25$	-1.5
	20	$6.95-j8.2$	-2.37
Matched	10	$37.8-j12.3$	-14.17
	20	$56.2-j16.8$	-15.54

Table 4.2 Impedance and S_{11} in dB in both the matched and unmatched case

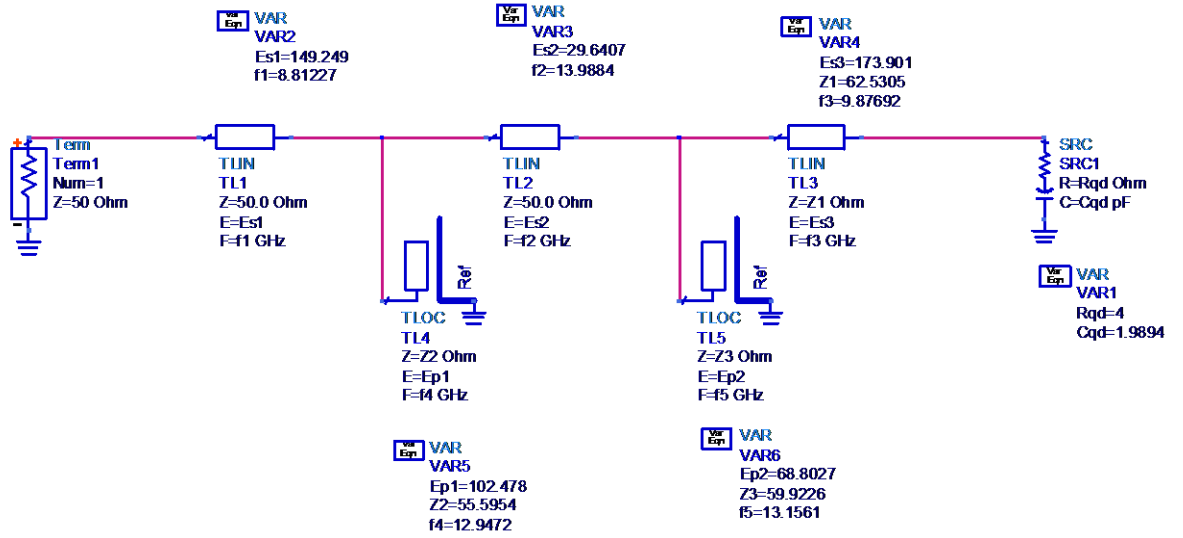


Figure 4.12 Ideal Transmission line model of matching network between the QDMLL and bow-tie slot antenna

The matching network using ideal transmission lines is shown in Figure 4.12. Using the fast converging algorithms such as the genetic algorithm [2], the unknown variables including the electrical length, the operating frequency and the characteristic impedance of each transmission line are optimized to meet the requirements. Next, the

CPW-based-matching circuit is designed as shown in Figure 4.13. In the design, the abrupt transitions in the structure are taken into account in the simulation.

The return loss with and without an impedance matching circuit is compared in Figure 4.14. According to the computed data, the delivered power to the load is only 29 % at 10GHz and 43% at 20GHz of the generated power for the unmatched case. With the equation of $G_{dB} = 20\log_{10}(T_{matched}/ T_{unmatched})$ where $T=S(2,1)$, the possible gain is computed by employing the impedance transformer. Its result is also shown in Figure 4.14. The outline of the impedance matching circuit and its corresponding dimensions are presented in Figure 3.30 and Table 4.3, respectively. Figure 4.16 shows the bow-tie slot antenna integrated with a dual-band impedance matching network. In the figure, the yellow component is the metal structure and the black one is that of the dielectric. To affirm the progress due to a matching network, the emitting power intensity out of the antenna with a matching circuit is compared with that of an antenna without the aid of impedance transformer at 10 GHz. The result is presented in Figure 4.17. The received power intensity in the matched and unmatched case is -41 dBm and -45.7 dBm, respectively. As a result, the gain in the received power intensity is 4.7 dB. This result agrees with the simulated 5 dB-gain in the return loss.

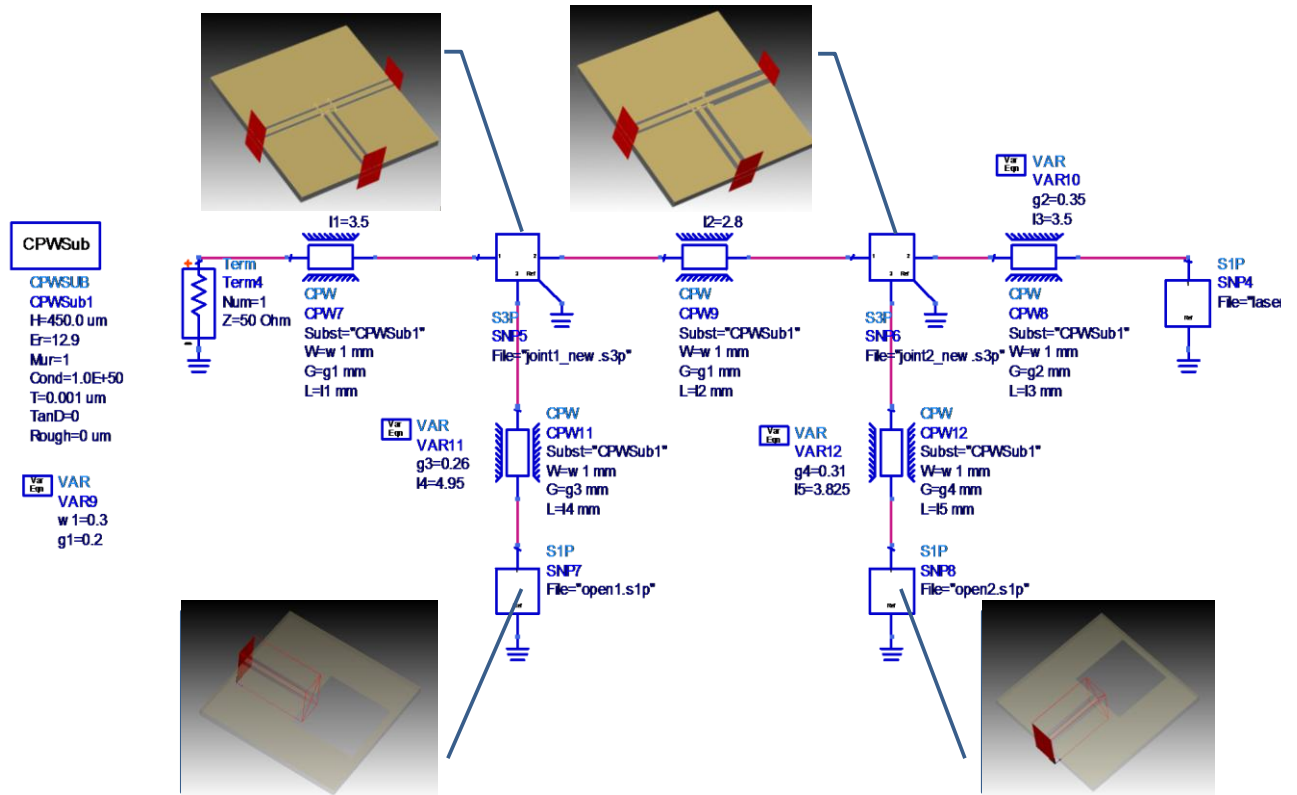


Figure 4.13 The CPW-based-impedance matching circuit between the QDMLL and bow-tie slot antenna

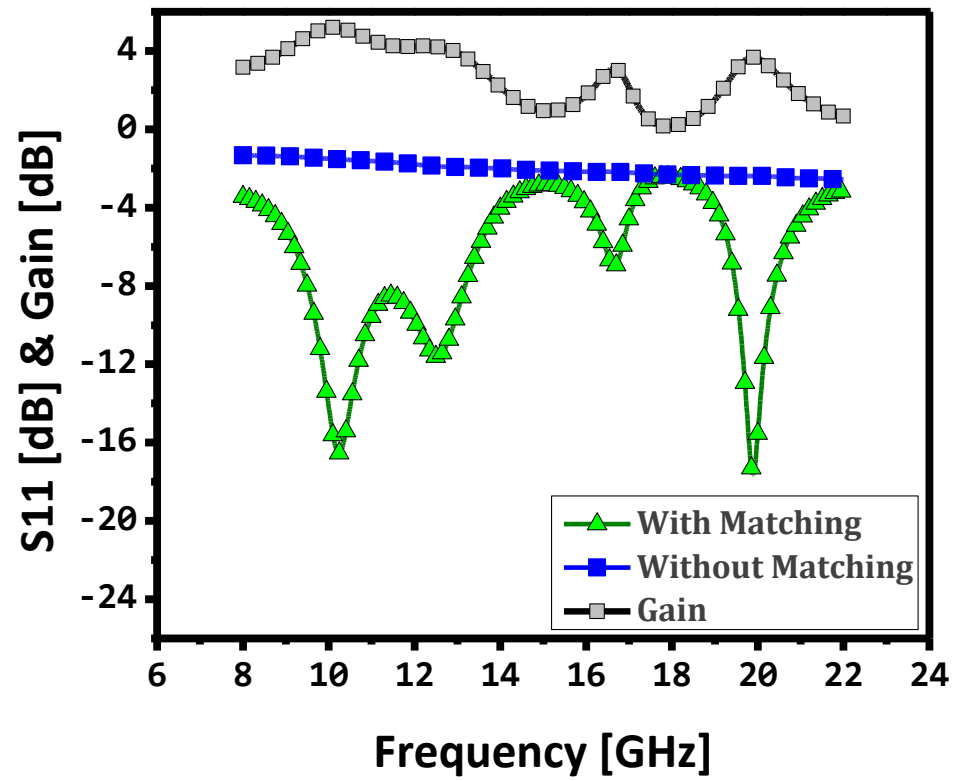


Figure 4.14 The simulated return losses under the consideration of both matched and unmatched cases, and the computed gain in dB

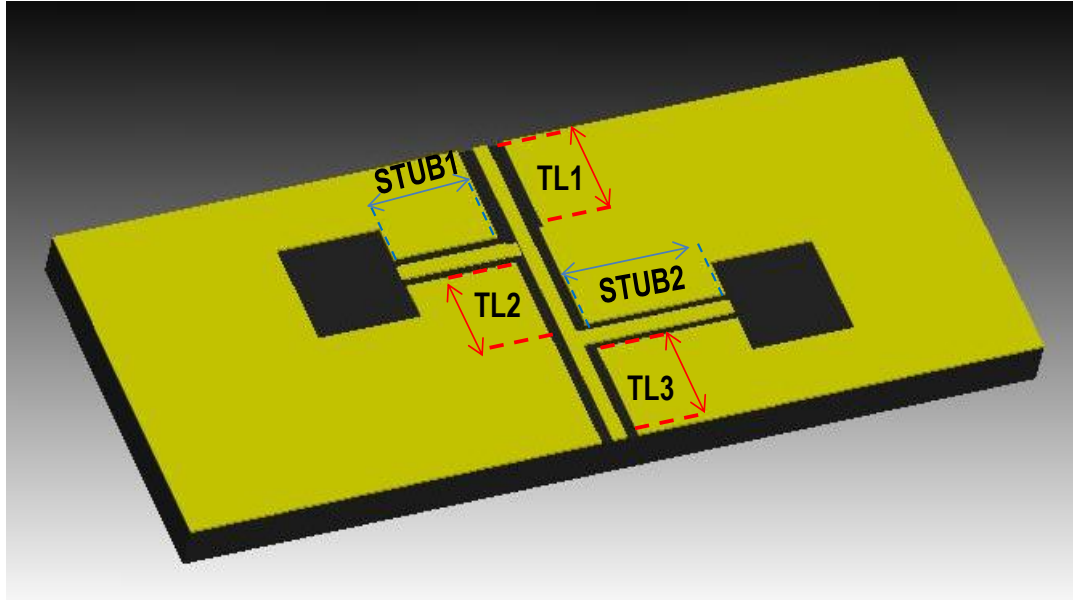


Figure 4.15 The schematic of an impedance transformer of two open stub lines.

Unit: mm

	W	G	L
TL1	0.3	0.2	3.5
STUB1	0.3	0.26	4.95
TL2	0.3	0.2	2.8
STUB2	0.3	0.31	3.825
TL3	0.3	0.35	3.5

Table 4.3 Dimensions of an impedance matching circuit

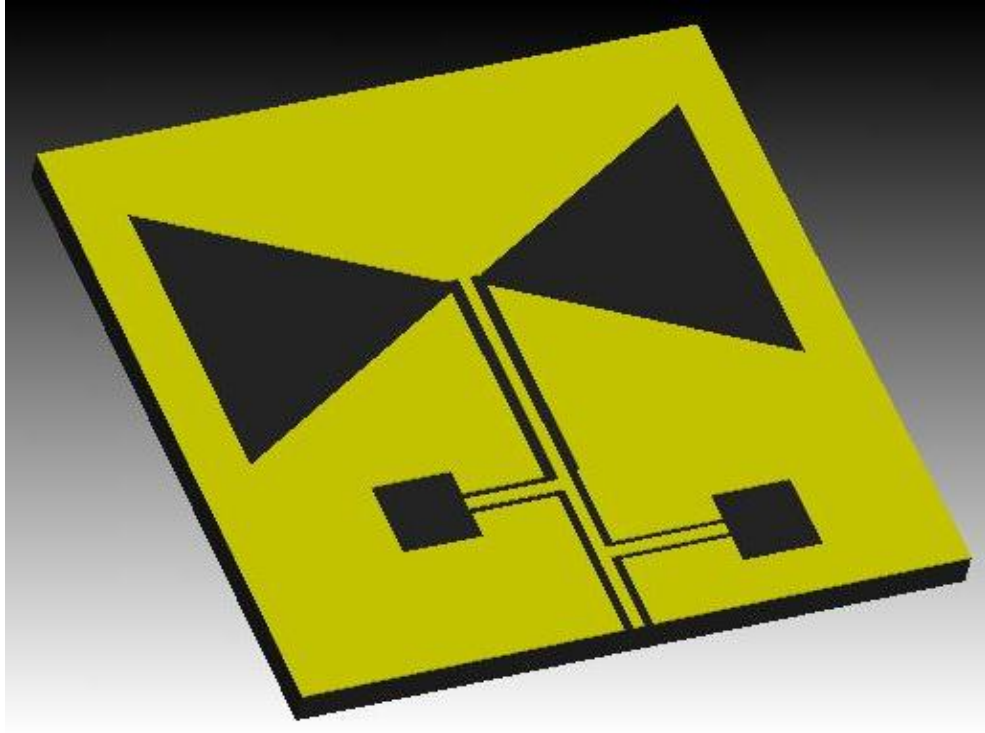


Figure 4.16 A dual-band impedance matching network embedded bow-tie slot antenna

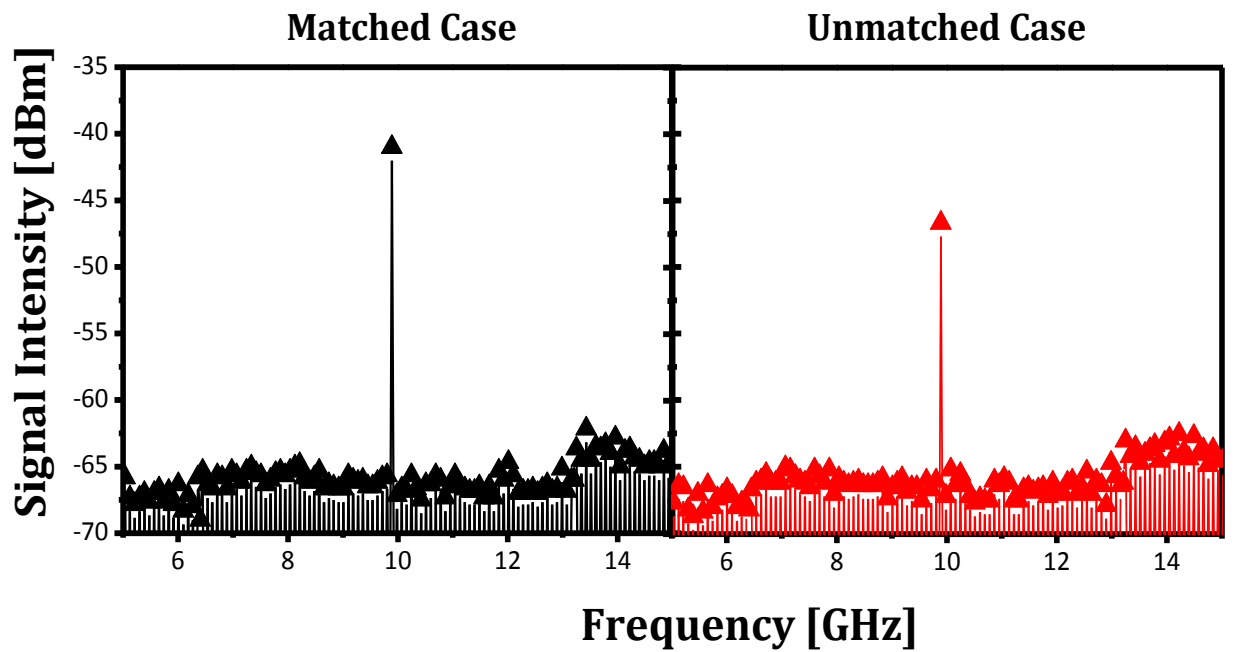


Figure 4.17 Measured signal power intensity comparison between matched and unmatched case

4.4 Tapered Slot Antenna (TSA) Design using the Ideal Transmission Line

In previous discussion, we designed the multiband resonance bow-tie slot antenna and tested the radiation improvement by adding an impedance matching circuit. In this section, the phased array tapered slot antenna is fabricated to perform a beam-steering experiment. Our aim is to also achieve beam steering by changing the bias conditions on the QDMLL and avoid the use of any RF phase shifters.

The tapered slot antenna (TSA) was initially developed by Gibson et al. and Yngvesson et al. [3, 4]. It consists of a tapered slot etched onto a thin film of metal on a substrate. It produces radiation in the end-fire direction at the wider end of the slot. Since the phase velocity of the travelling waves on the antenna is smaller than the speed of light in free space, the radiation out of an antenna occurs toward the end-fire.

In order to reduce the time and effort to design a TSA, the transmission line model is applied. The TSA in the length of L can be modeled by cascading the ideal transmission lines with progressing characteristic impedances and the length of L_n ($L_n=L/N$) [5]. This can be supported by the electric field distribution profile in Figure 4.18. Thus, the equivalent circuit model of a TSA is also regarded as the cascaded step lines as shown in Figure 4.19. In the equivalent model, the circuit is compared to the series-combined TLINs and shunt admittance (Y_k). TLIN has the characteristic impedance (Z), propagation constant (β) and length (θ) at 10 GHz. Shunt admittances (Y_k) is due to the step discontinuities between TLINs. The discontinuity is decreased if the step line becomes finite. In other words, the discontinuity admittances are ignored due to the small slot step changes. This approximation is valid because the large number of steps reduces the reflected traveling wave within the slots in the TSA i.e. $\lim_{n \rightarrow \infty} Y_k \cong 0$.

Figure 4.20 presents three equivalent ideal TLIN-models of a TSA. Each TLIN is composed of the characteristic impedance (Z) and electrical length (θ) based on the fundamental frequency of 10 GHz. The load impedances of the models are $120\pi\Omega$. For an ideal TLIN model, the propagation constants and electrical lengths are computed as $\beta = \omega/c$, $\theta = \beta l$ at $f = 10$ GHz. Here c is the speed of light at air and ω is the angular frequency of 10 GHz. Using the ADS, unknown values of Z , l are determined. The optimized Z and l values of the ideal transmission line are converted to the physical gap width and length of the slot line. For instance, the size of an air gap is computed based on the line impedance calculation for the slot line. The slot line's physical length (l') is found out by $l' = (\beta/\beta')l$. Here, β' is the propagation constant of a slot line at 10 GHz. The β and l are respectively the propagation constant and length of an ideal TLIN. The slot gaps and line lengths for the three models are presented in Table 4.4. The ideal transmission line modeled TSAs are shown in Figure 4.21.

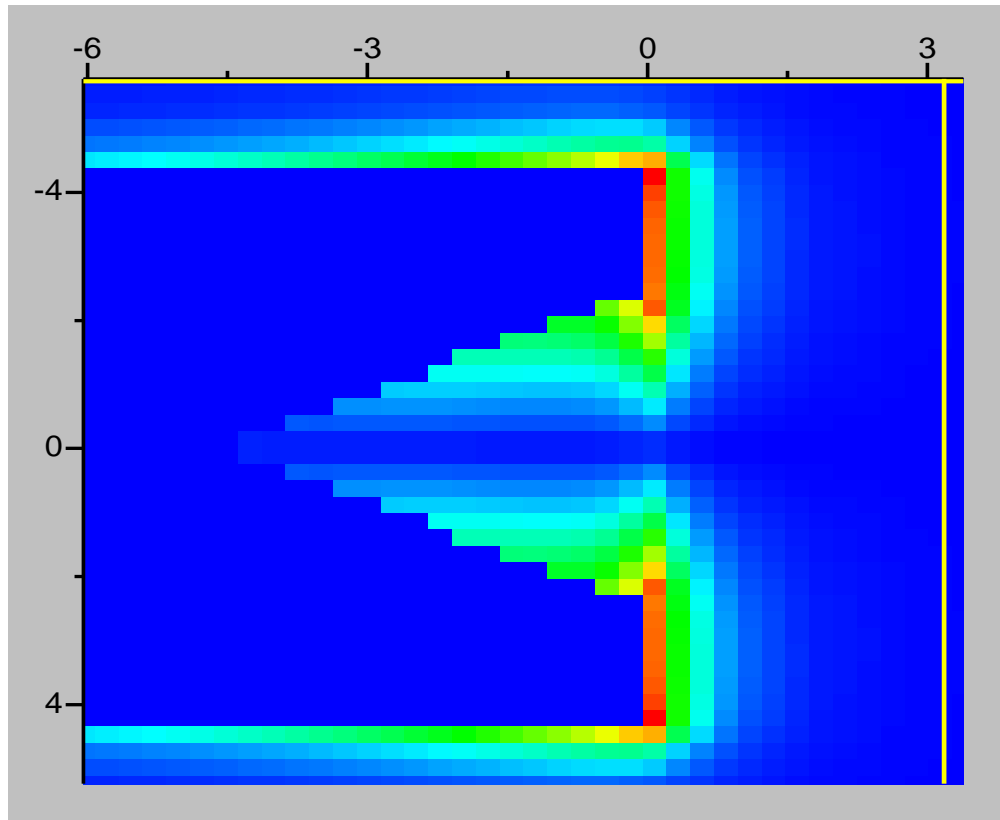


Figure 4.18 Electrical field distributions on the TSA

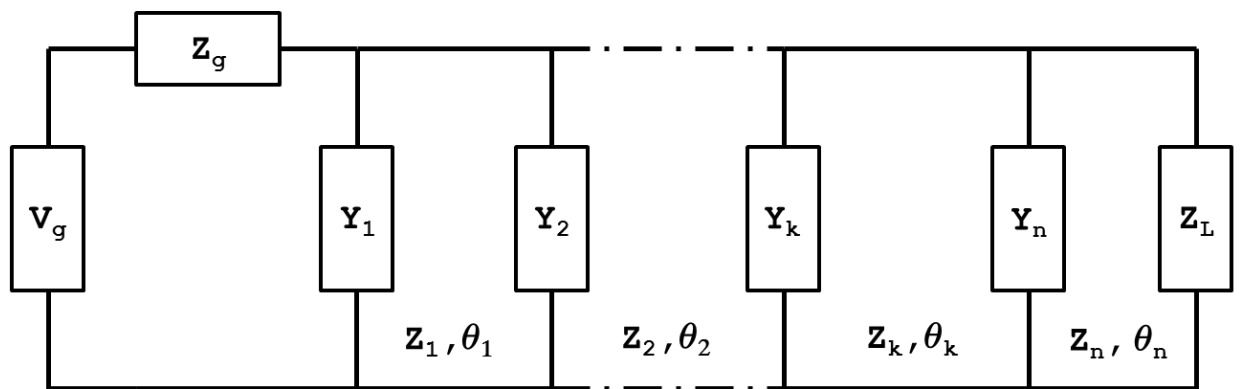


Figure 4.19 Equivalent circuit of the stepline

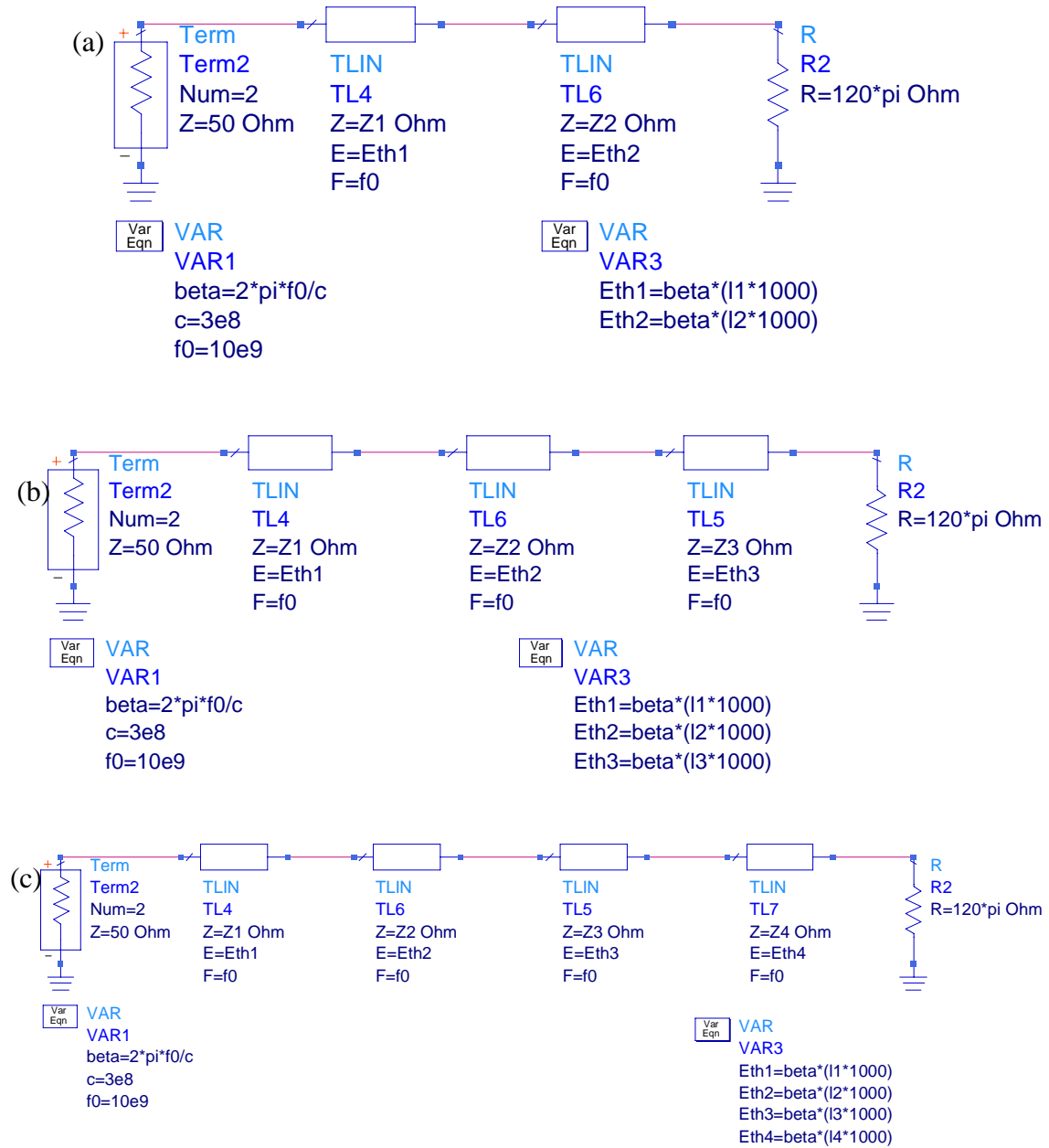


Figure 4.20 (a) Two-TLIN model of a TSA; (b) Three-TLIN model of a TSA;

(c) Four-TLIN model of a TSA

(a)Two-TLIN

Z1	186.57
Z2	504
l1	3.95124
l2	0.7488

Unit: mm

g1	3.7
g2	5.2
l1'	1.8944
l2'	0.5012

(b)Three-TLIN

Z1	50
Z2	135
Z3	430
l1	1.39376
l2	2.87257
l3	3.09084

g1	0.055
g2	0.8
g3	4.4
l1'	0.5695
l2'	1.2998
l3'	1.5676

(C)Four-TLIN

Z1	59.2197
Z2	96.6004
Z3	223.685
Z4	457.106
l1	1.51943
l2	1.89764
l3	2.63293
l4	1.85544

Unit: mm

g1	0.1
g2	0.41
g3	2.0
g4	4.8
l1'	0.6342
l2'	0.8386
l3'	1.2989
l4'	0.8507

Table 4.4 Dimensions of slot line model of a TSA

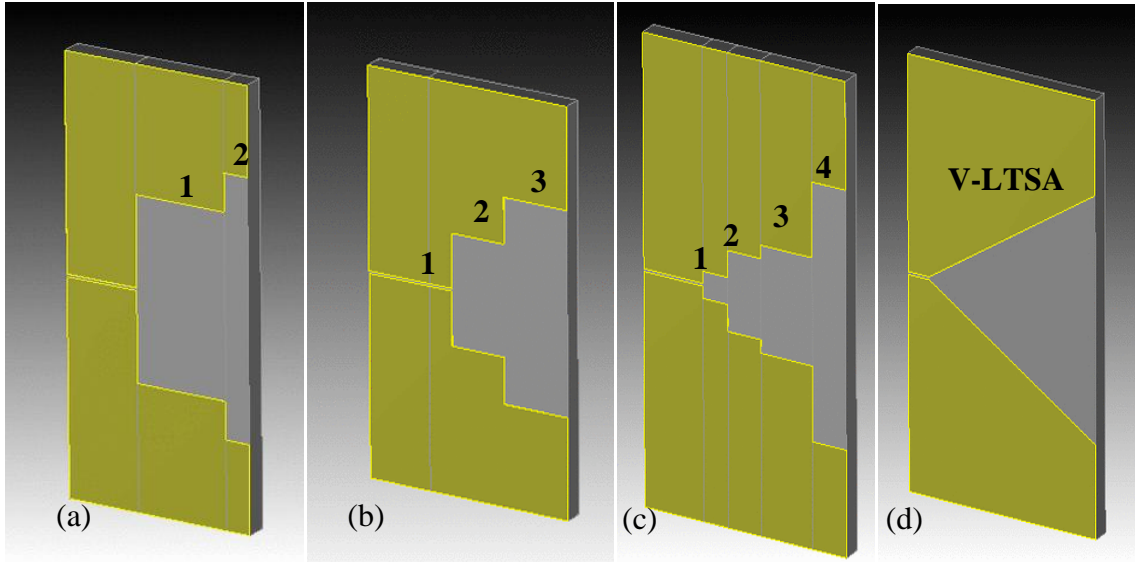


Figure 4.21 Schematic views of the TSA with increased transmission lines; (a) two section, (b) three section, (c) four section, (d) V-LTSA

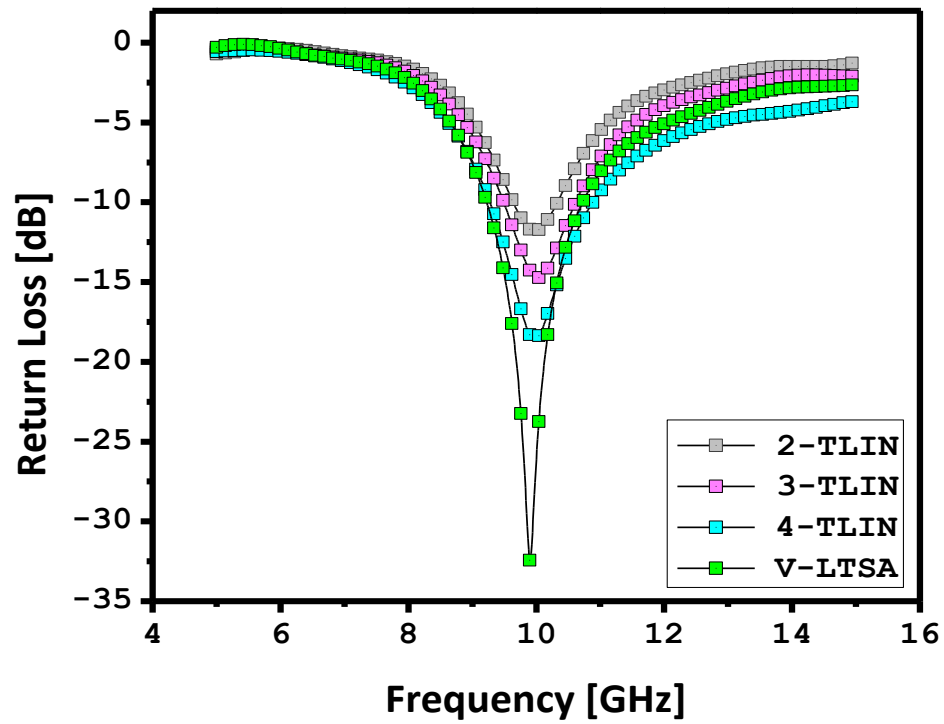


Figure 4.22 Return losses of the TLIN-modeled TSAs and the V-LTSA

4.5 Tapered Slot Antenna (TSA) with Biasing Lines

To incorporate with a QDMLL, the linearly tapered slot antenna (LTSA) is designed using the ideal TLIN-models. The shape and detailed dimensions are presented in Figure 4.23 and Table 4.5. The LTSA is fed by a coplanar slot line of the 0.1-mm wide air gap. The corresponding characteristic impedance of a slot line with a 0.1-mm air gap is 50Ω at 10 GHz. The design goal is to make an antenna operate at 10 GHz and the operation of an antenna should not be affected by the biasing lines for a QDMLL. The biasing lines for a QDMLL are also shown in Figure 4.23. The biasing network is composed of the forward DC current (I_f), reverse voltage (V_r) and GND lines. The simulated input impedance (Z_{in}) of the LTSA is presented in Figure 4.24. Based on the simulated result, the resonance frequency of an antenna is 10 GHz because of $\text{Imag}(Z_{in}) \cong 0$ and $\text{Real}(Z_{in}) \cong 50$ at 10 GHz.

The proposed LTSA is fabricated by the lithographic method. The measured return loss is compared to the simulated data. As shown in Figure 4.25, two results are well agreed at the desired frequency.

After integrating with a QDMLL, we measured the emitting power intensity out of the integrated module through an angle-rotation of the receiving antenna. As a receiving antenna, an X-band horn antenna is used. It rotates along $-90^\circ < \phi < 90^\circ$ at the fixed $\theta = 90^\circ$. Figure 4.26 shows both the simulated directivity and measured emitting power intensity. The mostly strong radiation is in the direction of $\phi = 0^\circ$, $\theta = 90^\circ$. This is because the TSA produces radiation in the end-fire direction at the wider end of the slot [6].

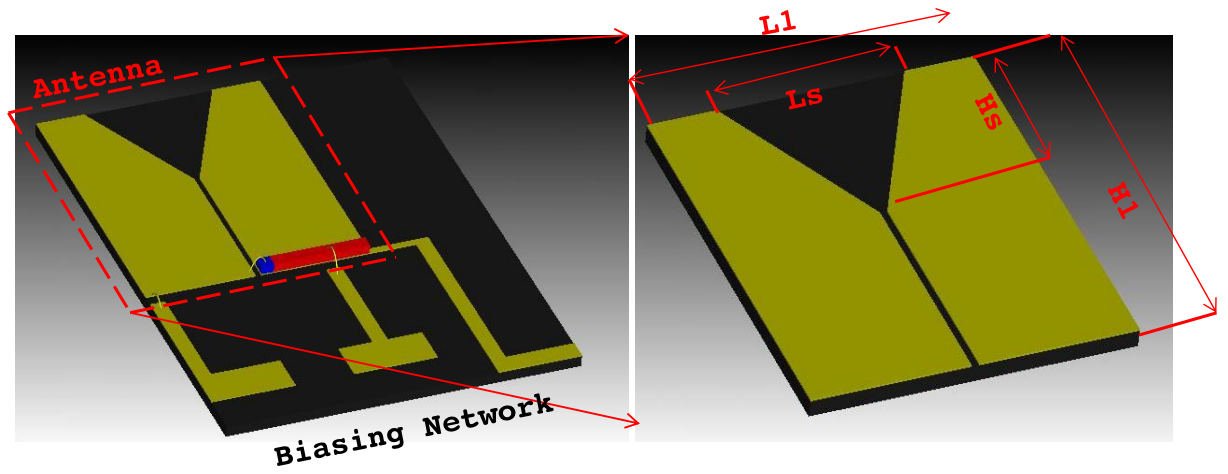


Figure 4.23 QDMLL-integrated-TSA module and the enlarged view of a TSA

Unit: mm

L1	8.8
Ls	4.9985
H1	10.5
Hs	4.667

Table 4.5 Detail dimensions of a TSA

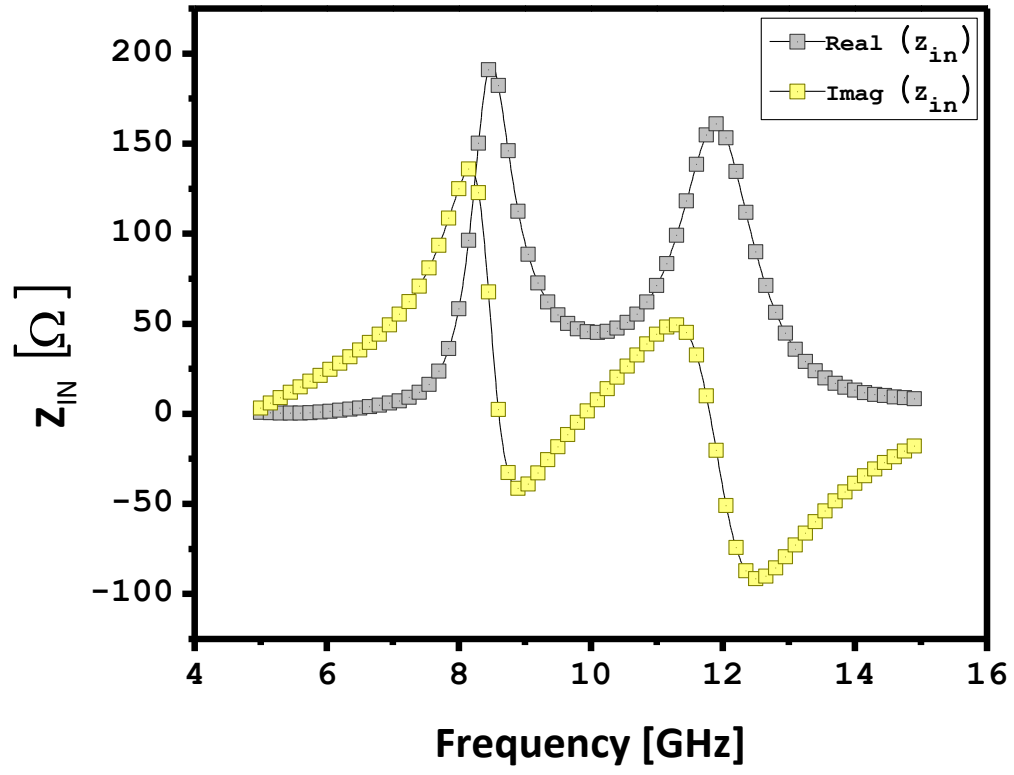


Figure 4.24 Input impedance (Z_{in}) of the TSA

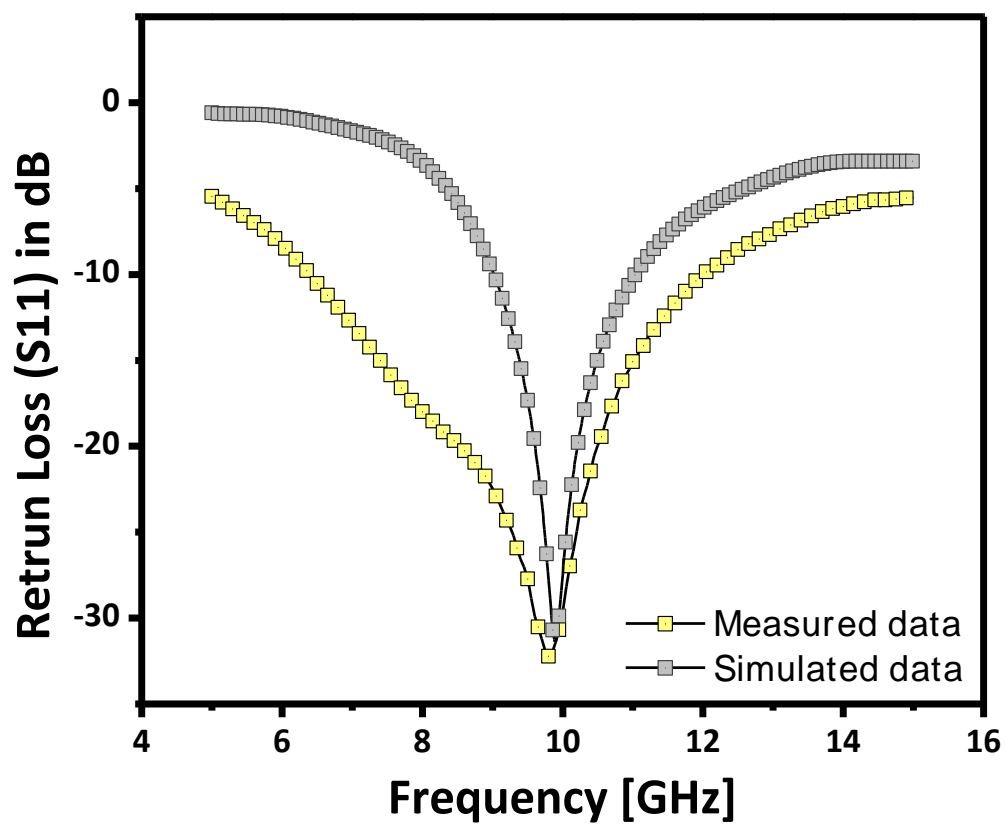


Figure 4.25 Measured and simulated return losses

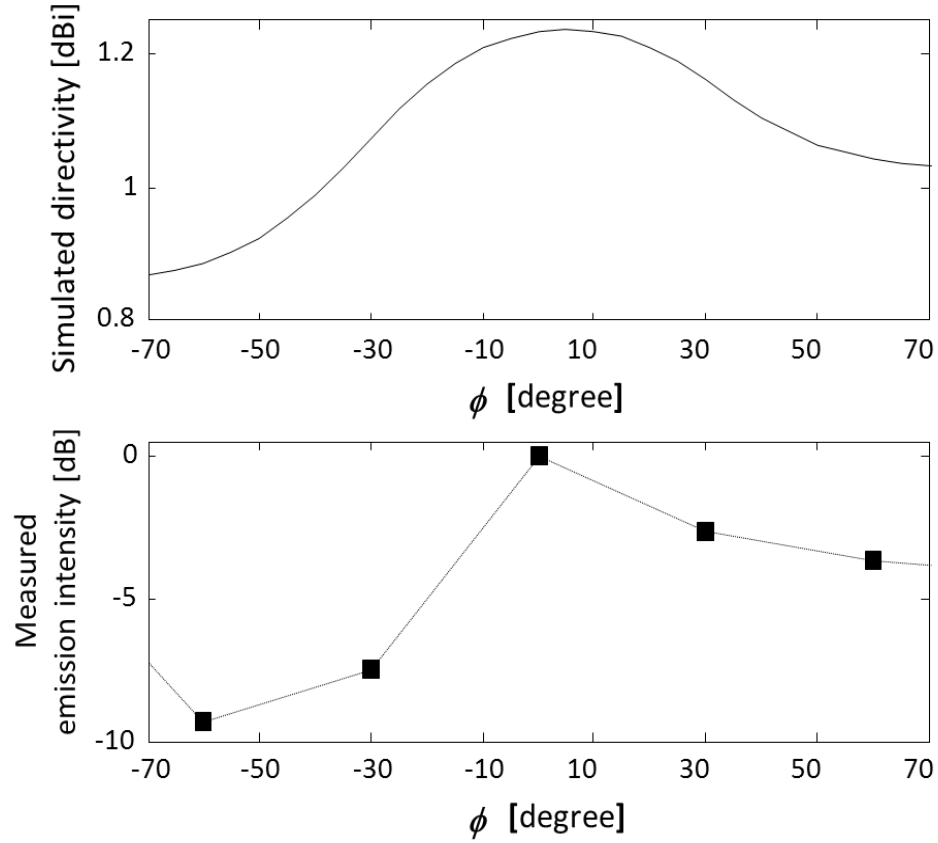


Figure 4.26 Simulated directivity and measured radiation intensity over $-90^\circ < \phi < 90^\circ$

4.6 2 Element TSA Array

Here, the design and operation of two element linearly tapered slot-line antenna array is described. The antenna array was designed to achieve beam steering by manipulating the bias conditions of a QDMLL. The common technique to achieve beam steering in array antennas is to differentiate the microwave signal out of the power sources by implementing phase shifters such as phase delay lines [7-9]. To this end, an external phase controller such as a phase delay line or phase shifter is required. The external phase controllers have been well developed and investigated. Yet, the power consumption and the enlarged size of an array are inevitable. Of particular interest are the

QDMLLs because they are capable of generating photocurrents of different phases by manipulating the reverse voltage bias on the absorber. The detail theory of phase variation of output photocurrent was previously explained in Chapter 2. A two element phased tapered slot antenna array was fabricated and integrated with two identical QDMLLs.

To design an array system, the interval distance (d) of two adjacent elements needs to be decided. The distance affects its radiation property. If the distance is chosen too small, its destructive mutual coupling between two elements can deteriorate the desirable radiation pattern [10-12]. In order to choose the proper distance (d), the S21s of various distances are simulated. The result in Figure 4.27 shows that the mutual coupling of two antennas gets smaller as the distance of separation gets larger. Although the lower S21 is preferable for better array performance, the array size is also a limitation. As a compromise, the smallest distance that satisfies $S_{21} < -15$ [dB] was chosen. The fabricated prototype of the QDMLL-integrated-TSA array is shown in Figure 4.28. The biasing microstrip lines consist of pumping currents, applied voltages and a common ground. Each line is designed to have an infinite impedance at 10 GHz so that the excited signal can only propagate into the array module. Two identical QDMLLs are directly mounted onto a co-planar ground side of a TSA and the absorber is wire-bonded to the other metal-side of the TSA.

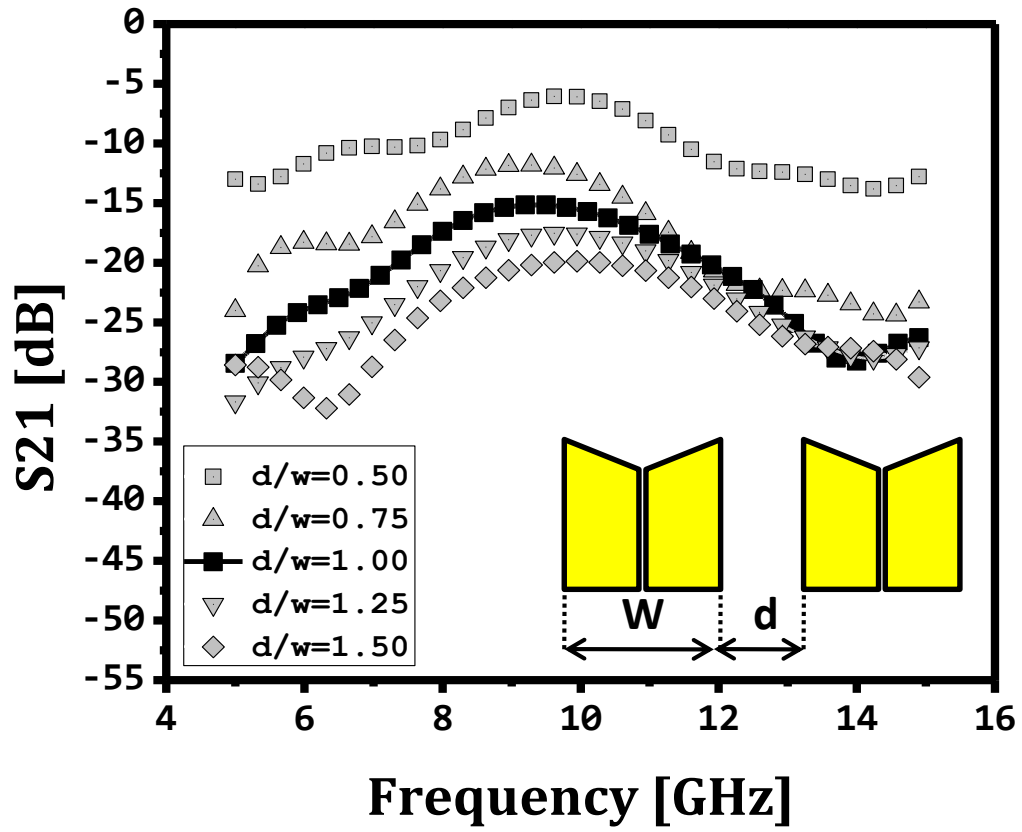


Figure 4.27 S_{21} -simulation of the 2 element TSA array as increasing the interval distance

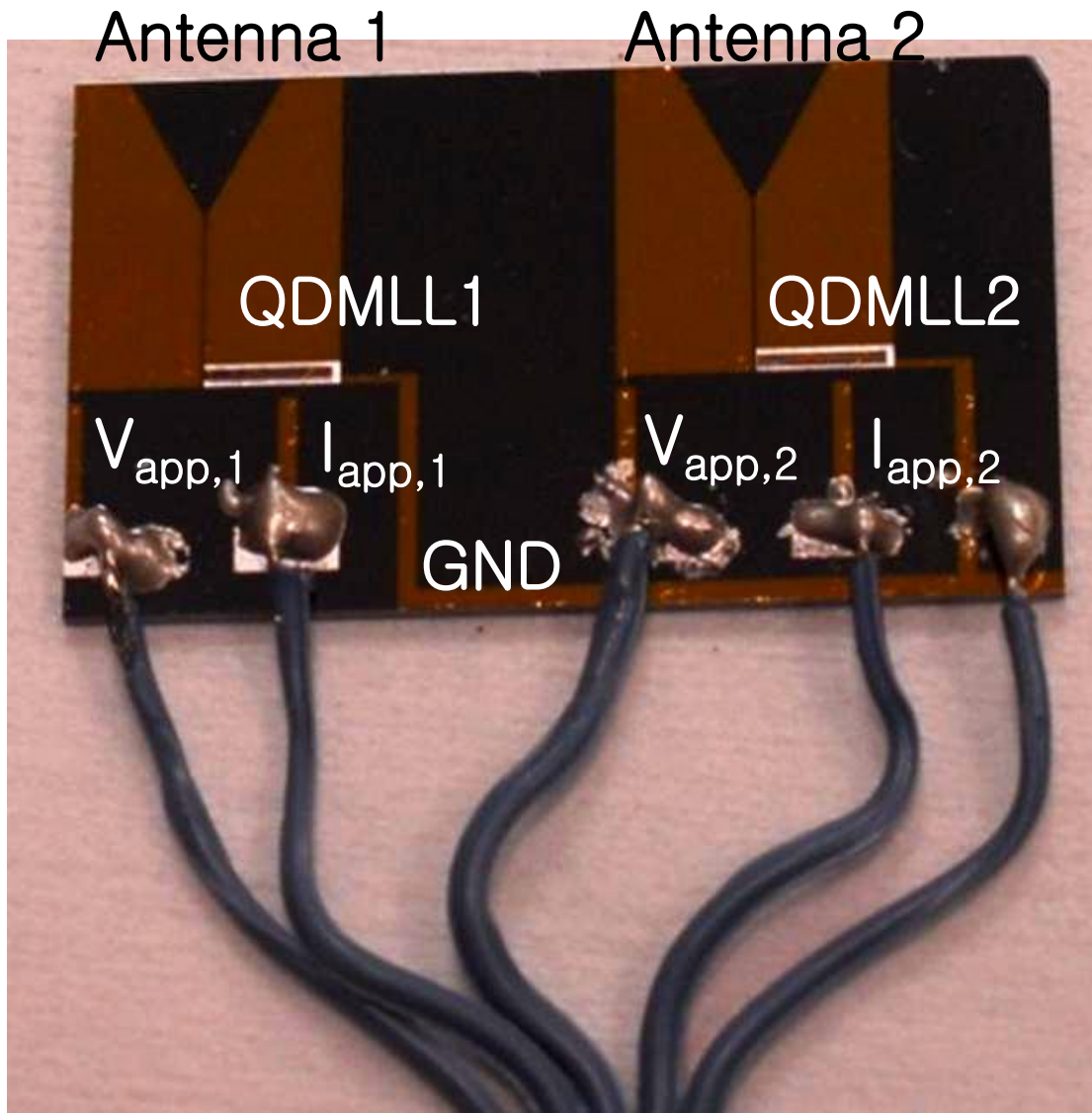


Figure 4.28 Photo-image of the fabricated QDMLL-integrated-LTSA array

4.7 Beam-steering Experiment

The radiation measurement setup is shown in Figure 4.29. In this setup, the array of TSAs, as the transmitter, is located in the center of the chamber. As the receiving antenna, an X-band horn antenna is mounted on the rotating post controlled by a stepper motor. The scanned RF spectrum of the emitted electrical field is monitored by an

electrical spectrum analyzer. All power supplies are placed outside of the chamber so that undesired scattering fields can be minimized. The phase and magnitude of the output photocurrents are controlled by means of manipulating the current and voltage bias on the QDMLL. The placement of the antenna in the anechoic chamber is shown in Figure 4.30. The distance between the transmitter and receiver is approximately 10 cm.

To achieve beam-steering, two different bias conditions are applied to the QDMLLs. The first bias condition is to apply 150-mADC currents and -2-Vvoltage to both QDMLLs. In the second bias case, 150-mADC currents and -2 V voltage is applied on the QDMLL 1 and 150-mA DC current and +0.5 V voltage is applied to the QDMLL2. In Figure 4.31, the output phase angle of a QDMLL is measured and presented. The resulting phases of -2V and +0.5V are respectively 21.7° and 12.6° . Thus, the phase angle difference of the two cases is 9.1° . In Figure 4.32, two maximum emitting power intensities are measured. For the first biasing case, the angle for the maximum power intensity is -10° . Next, the maximum value for the second biasing condition is measured at 0° .

In order to affirm the measured result, the directivity of the TSA array is simulated in Figure 4.33. The simulation shows that the angle of the maximum directivity increases by changing the same angle degree in input signals. Both measured emission power-intensity and simulated directivity demonstrates that radiation beam pattern is tilted by means of applying different voltages.

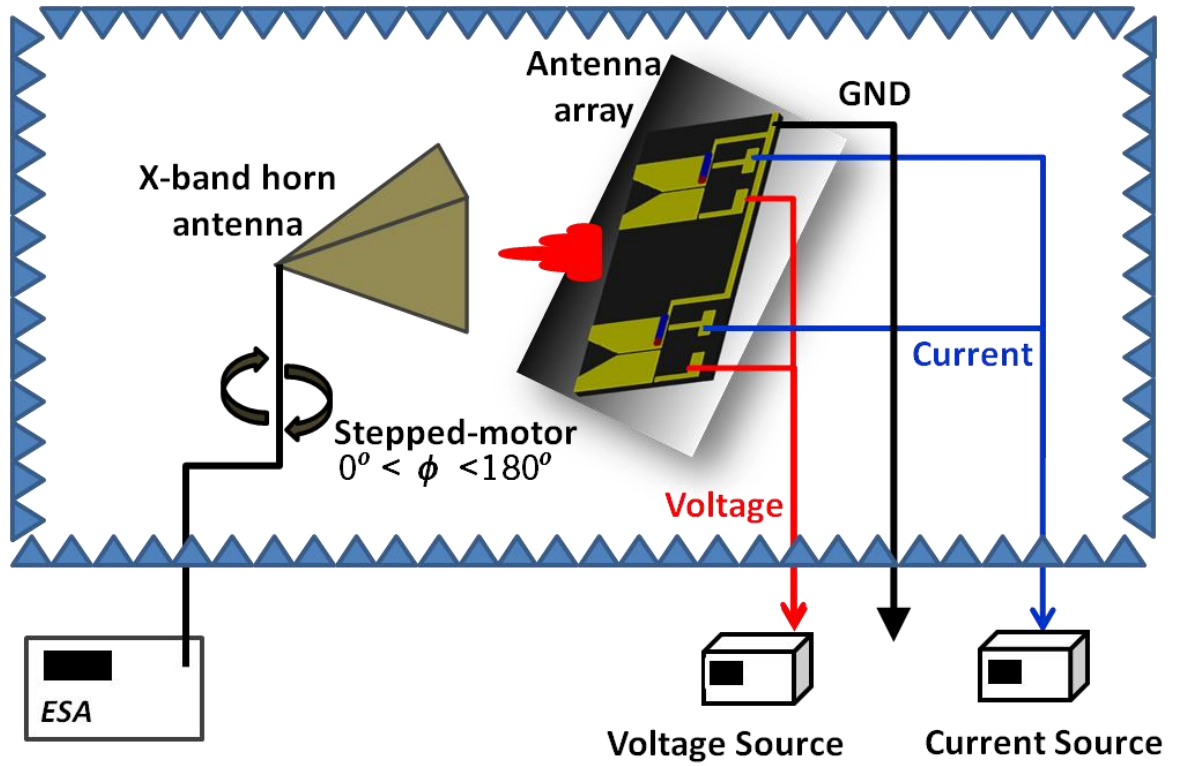


Figure 4.29 Experimental environment and schematics of a measurement setup for beam-steering

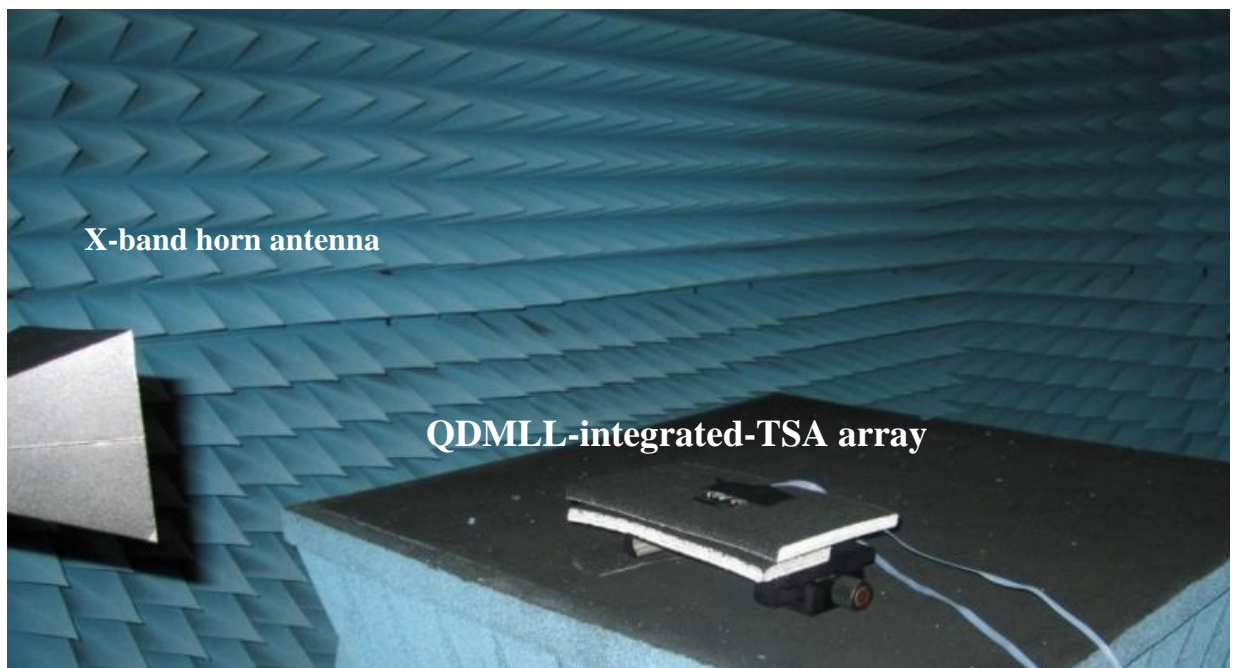


Figure 4.30 Photo-image of the measurement setup

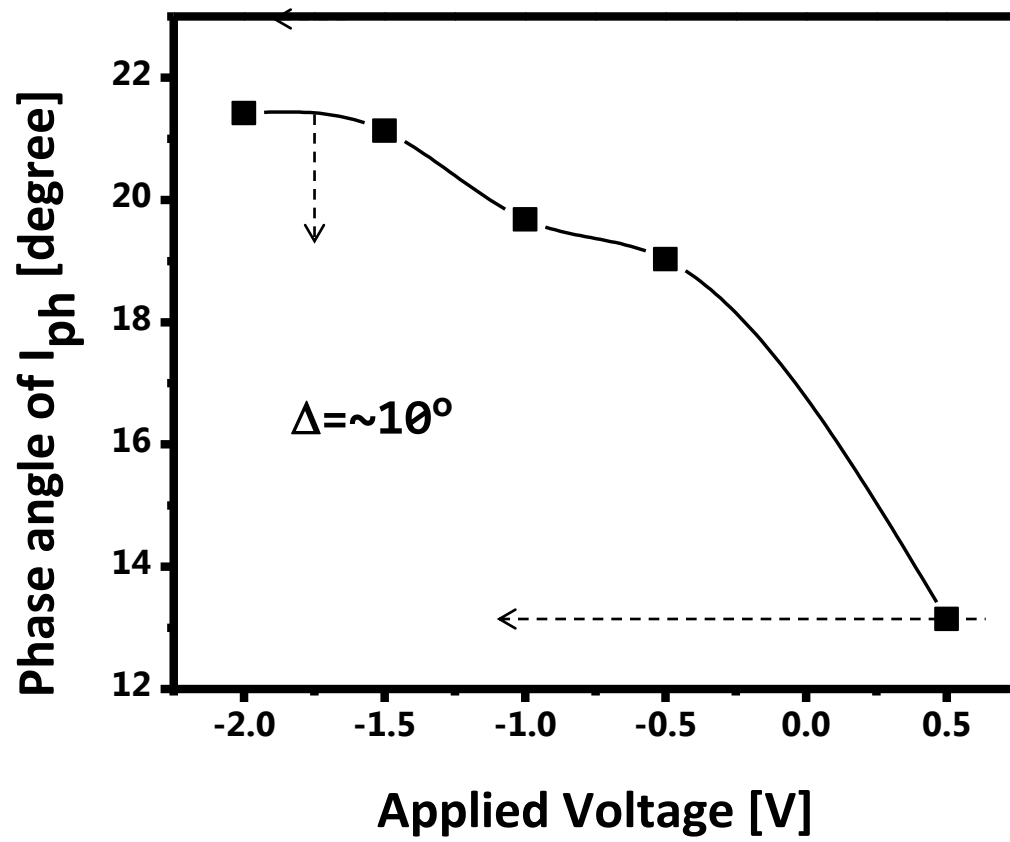


Figure 4.31 The measured output phase angle of a QDMLL as applied voltage

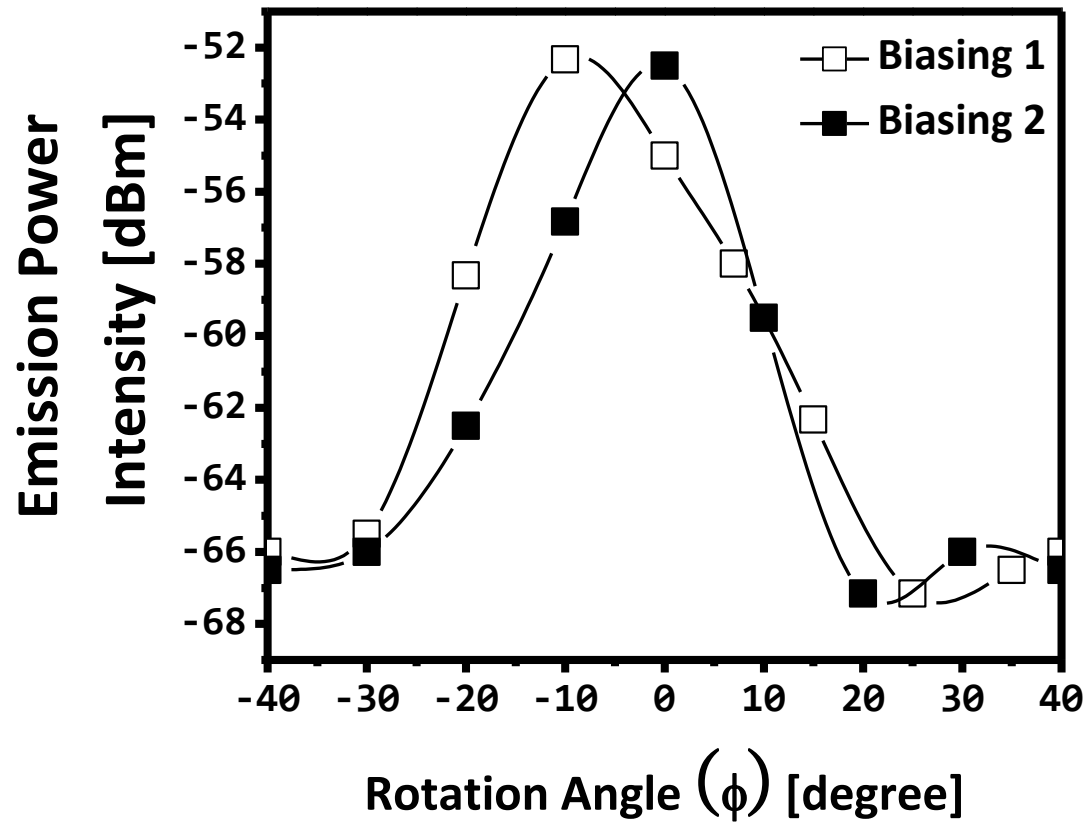


Figure 4.32 The measured emission power-intensity for different biasing conditions

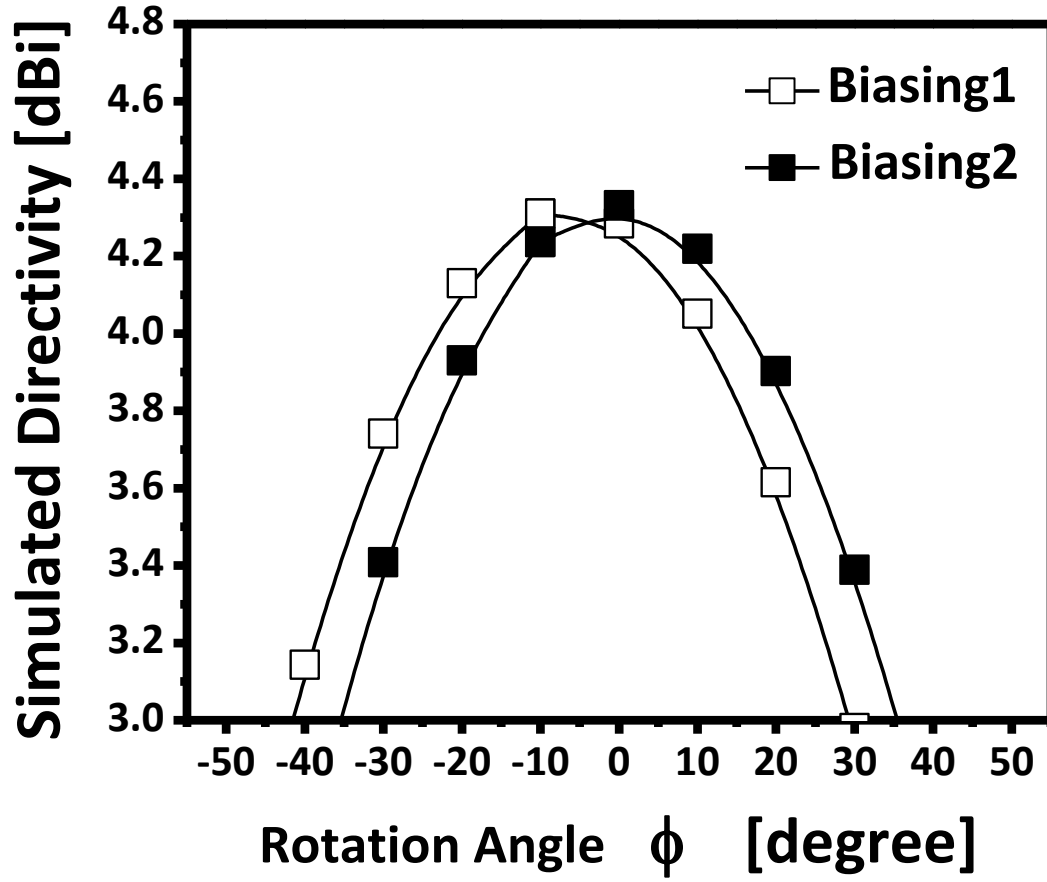


Figure 4.33 The simulated directivity of a TSA array

4.8 Conclusion

A dual band bow-tie slot antenna is first designed, fabricated and tested. Compared to the single resonance frequency antenna such as a bow-tie antenna or the microstrip antenna, the QDMLL can extend its operating range by using the slot antenna. An impedance matching circuit is introduced to increase the radiation efficiency at the first and second order harmonics of the QDMLL; 10 and 20 GHz. Based on the numerical

computation, the antenna is able to have around 5.17 dB-gain at 10 GHz and 3.63 dB-gain at 20 GHz with this impedance matching.

In 4.2, beam-steering capabilities were clearly demonstrated using an integrated 2 element QDMLL-LTSA phased array by manipulating the laser bias conditions. To improve the efficiency of the antenna design, the LTSA was designed using the equivalent ideal transmission line model. The far-field measurement experiment in an anechoic chamber showed good agreement between measured and simulation results. With this novel technology the QDMLL demonstrates potential to be an attractive candidate in realizing a compact phased array system without the use of complicated delay lines and phase shifters.

4.9 References

1. Advanced Design System (ADS), (www.home.agilent.com/agilent).
2. E. Michielssen, S. Ranjithan, R. Mittra, "Optimal multilayer filter design using real coded genetic algorithms," *Optoelectronics, IEE Proceeding*, Vol. 139, Issue no. 6, pp. 413 – 420, Dec., 1992
3. P. J. Gibson, "The Vivaldi aerial," in *Proc. 9th Eur. Microwave Conf.*, Brighton, U.K., Jun. 1979, pp. 101–105.
4. K. S. Yngvesson, "Endfire tapered slot antennas on dielectric substrates," *IEEE Trans. Antennas Propagat.*, vol. 33, no. 12, pp.1392–1400,1985.
5. H. Oraizi, S. Jam, "Optimum design of tapered slot antenna profile," *IEEE Trans. Antennas Propagat.*, vol. 51, no. 8, pp.1987–1995, Aug. 2003.
6. K.S. Yngvesson, T.L. Korzeniowski, Y.-S. Kim, E.L. Kollberg, J.F. Johansson, "The tapered slot antenna-a new integrated element for millimeter-wave applications," *IEEE Trans. Microw. Theory Tech.*, vol. 37, no.2, pp. 365 - 374, Aug. 2002.
7. E. Ojefors, Cheng. Shi, K. From, I. Skarin, P. Hallbjorner, A. Rydberg, "Electrically Steerable Single-Layer Microstrip Traveling Wave Antenna With Varactor Diode Based Phase Shifters," *IEEE Trans. Antennas Propagat.*, vol. 55, no. 9, pp. 2451 - 2460, 2007.
8. M.A.Y. Abdalla, K. Phang, G.V. Eleftheriades, "A Planar Electronically Steerable Patch Array Using Tunable PRI/NRI Phase Shifters," *IEEE Trans. Microw. Theory Tech.*, vol. 57, no.3, pp. 531–541, 2009.

9. M.Y.-W. Chia, T.-H. Lim, J.-K. Yin, P.-Y. Chee, S.-W. Leong, C.-K. Sim, "Electronic Beam-Steering Design for UWB Phased Array," *IEEE Trans. Microw. Theory Tech.*, vol. 54, no.6, pp. 2431 - 2438, Jun. 2006.
10. Hoi-Shun Lui, Hot Tat Hui, MookSeng Leong, "A Note on the Mutual-Coupling Problems in Transmitting and Receiving Antenna Array," *IEEE Mag. Antennas Propagat.*, vol. 51, no. 5, pp. 171 – 176, Oct. 2009.
11. Jing Zhao, Yueheng Li, Guishuang Sun, "The Effect of Mutual Coupling on Capacity of 4-Element Squared Antenna Array MIMO Systems," WiCom '09. 5th International Conference, pp. 1-4, Sept. 2009.
12. T. Mbarek, Gharsallah, "Mutual coupling in phased array for 3X4 Butler Matrices antenna network," *Int. Signals, Circuit and Systems*, 2008, pp. 1-5, Nov.2008.

Chapter 5

Conclusions and Future Work

5.1 Summary and Conclusions

In this work, the integration of a Quantum Dot Mode Locked Laser, that acts as a microwave and millimeter wave source, with a wideband antenna is presented. To this end, two aspects of research are discussed. The first aspect of this dissertation dealt with the MLLs based on the quantum dot (QD) materials. Due to the unique properties of the QDs, the QDMLL can expand the range of stable mode-locking operation. The details on the MLL structure and operation mechanism are also discussed by experimenting on a two-section QDMLL. In order to gather photocurrent from the absorption section, forward currents are applied on the gain and reverse voltage-bias to the absorber.

The second aspect of this dissertation is the realization of a compact transmitting antenna integrated to a QDMLL. For this purpose, several antenna prototypes are designed by using the two-port approach. The designed antennas are fabricated and integrated with laser chips using the lithographic method. The emitted power intensity and estimated pattern out of the fabricated prototypes are presented and discussed. Measurements on these integrated antennas showed a good agreement between simulation and experimental results. Moreover, the measured radiation generated by the QDMLL also confirms the proposed concept of the MLL as a possible compact microwave antenna source. To fully take an advantage of a QDMLL, a bow-tie slot antenna was used. The challenge of designing a slot antenna is that the fabricated antenna should resonate at multiple harmonics of the QDMLL repetition rate. Thus, available frequencies of MLLs are extended.

Another important development for the QDMLL-integrated-antenna is to match the antenna impedance to the absorber impedance, which is the key for enhancing the radiation efficiency. With the proposed dual band impedance matching stub lines, the power gain to the load is improved by 5-dB at 10 GHz and 3-dB at 20 GHz, respectively.

Finally, an example of achieving beam-steering using a two-element QDMLL-LTSA phased array by manipulating the laser bias condition is presented and discussed. To improve the efficiency of the antenna design, the LTSA was designed using an equivalent ideal transmission line model. Up to 10° , beam steering is observed by simply handling the applied voltage bias on each QDMLL and without the use of any external phase shifters. The far-field measurement performed in an anechoic chamber showed good agreement between measured and simulated results. With this technology, the proposed RF/Photonic antenna has the potential to be an attractive candidate in realizing a compact phased antenna array system by removing complicated delay lines and phase shifters.

5.2 Future Work and Recommendation

The results of this work show that the amount of generated power of the QDMLL is limited. The power of photocurrents is in general in the order of mW. Although an impedance matching circuit has been implemented, the radiating power intensity is still not sufficient. There are several possible approaches that can be used to increase the radiating power. At the MLL level, the generation of photocurrents can be increased by enhancing the optical-to-electrical conversion efficiency. A second approach is to use a power amplifier between the QDMLL and the antenna to amplify the signal from the

MLL. This approach will give enough power to make the proposed design useful for practical applications where more power out of the antenna is required.

Another challenge in our research is to produce the higher repetition rates. Based on the discussion in Chapter 2, the repetition rate of QDMLLs is inversely related to the total cavity length. The shorter the cavity, the higher repetition rate. However, the absorption of the signal out of the cavity is restricted by the size of the absorber. To resolve this limitation, the multisection QDMLL is suggested in 2.4. It is useful not only for the high frequency pulse generation but also for generating a reconfigurable microwave source by manipulating its bias positions. The ultimate reconfigurable system is feasible by combining the multisection QDMLL with reconfigurable antennas.

Another area of future research that merits further attention is using the double interval approach to generating multiple harmonics in the cavity and extracting several RF frequencies simultaneously. This will require a more sophisticated design with a single or multiple antennas attached to the same QDMLL. The use of power amplifier can be employed here as well.

If a single combination of QDMLL/antenna is to operate between 5 to 65 GHz and beyond, a more broadband matching network will be required. This is not an easy task considering the fact that the matching network will have to be a planar structure that is inherently narrowband.

Finally, although, it was demonstrated that beam steering and phase shifting can be achieved by manipulating the voltage bias condition of the attached QMLLs, the result was around 10 degrees. For practical application the beam steering angle has to go beyond the 10 degree point at much higher frequencies.